

# **Cold Li–Yb<sup>+</sup> mixtures in a hybrid trap setup**



# Cold Li–Yb<sup>+</sup> mixtures in a hybrid trap setup

ACADEMISCH PROEFSCHRIFT

ter verkrijging van de graad van doctor  
aan de Universiteit van Amsterdam  
op gezag van de Rector Magnificus  
prof. dr. ir. K.I.J. Maex

ten overstaan van een door het College voor Promoties ingestelde  
commissie, in het openbaar te verdedigen in de Agnietenkapel  
op dinsdag 18 september 2018, te 12:00 uur

door

Jannis Klaus Joger

geboren te Bonn, Bondsrepubliek Duitsland

**Promotiecommissie:**

Promotor:	Prof. dr. F.E. Schreck	Universiteit van Amsterdam
Copromotor:	Dr. R. Gerritsma	Universiteit van Amsterdam
Overige leden:	Prof. dr. T. Schaetz	Universität Freiburg
	Dr. A. Negretti	Universität Hamburg
	Prof. dr. J.S. Caux	Universiteit van Amsterdam
	Prof. dr. H.B. van Linden van den Heuvell	Universiteit van Amsterdam
	Dr. R.J.C. Spreuw	Universiteit van Amsterdam

Faculteit der Natuurwetenschappen, Wiskunde en Informatica

The work described in this thesis was carried out in the group "Quantum Gases and Quantum Information", at the Van der Waals-Zeeman Instituut of the University of Amsterdam, Science Park 904, 1098 XH Amsterdam, The Netherlands, where a limited number of copies of this thesis is available. A digital version of this thesis can be downloaded from <http://dare.uva.nl>.

The work described in this thesis has been partially supported by the European Research Council (ERC) and the Netherlands Organization for Scientific Research (NWO).

Copyright © 2018 by Jannis Klaus Joger

This work is licensed under the Creative Commons Attribution 3.0 NL licence.

Cover design by Jannis Klaus Joger© 2018

Typeset by L<sup>A</sup>T<sub>E</sub>X.

Printed and bound by .

ISBN:

*It is better to light a candle  
than to curse the darkness.*

W. L. Watkinson

*To Kerstin.*



# Contents

<b>Contents</b>	<b>v</b>
<b>1 Introduction</b>	<b>1</b>
<b>2 Theoretical foundations</b>	<b>7</b>
2.1 Introduction . . . . .	8
2.2 Atom-ion interaction . . . . .	8
2.2.1 Atom-ion interaction potential . . . . .	8
2.2.2 Atom-ion collisions . . . . .	11
2.3 The linear Paul trap . . . . .	12
2.3.1 Trapped ions in a Paul trap . . . . .	12
2.3.2 Trapped atom-ion systems in a Paul trap . . . . .	15
<b>3 Quantum dynamics of an atomic double-well system interacting with a trapped ion</b>	<b>17</b>
3.1 Introduction . . . . .	18
3.2 Atomic double-well in presence of an ion . . . . .	19
3.3 Static ion in one dimension . . . . .	21
3.4 Moving ion in one dimension . . . . .	24
3.5 Micromotion . . . . .	29
3.5.1 Radial micromotion . . . . .	30
3.5.2 Axial micromotion . . . . .	38
3.6 Summary and Conclusions . . . . .	39
<b>4 Experimental setup</b>	<b>43</b>
4.1 Introduction . . . . .	44

4.2	Design considerations . . . . .	44
4.3	Final experimental setup . . . . .	46
4.4	Ion trap design . . . . .	46
4.4.1	Blade electrodes . . . . .	49
4.4.2	End cap electrodes . . . . .	49
4.4.3	Yb oven . . . . .	49
4.4.4	Mount for ion trap and MOT mirror . . . . .	51
4.5	Ion trap simulation . . . . .	53
4.6	Helical resonator . . . . .	56
4.7	Vacuum system . . . . .	58
4.7.1	Background gas pressure . . . . .	58
4.7.2	Main vacuum chamber . . . . .	58
4.7.3	Viewports . . . . .	61
4.7.4	Lithium oven setup . . . . .	62
4.8	Magnetic field coils . . . . .	65
4.9	Laser setup . . . . .	70
4.9.1	Laser systems for Yb . . . . .	70
4.9.2	Laser systems for ${}^6\text{Li}$ . . . . .	76
4.9.3	Frequency stabilization . . . . .	80
4.10	Optical access . . . . .	84
4.11	Imaging setup . . . . .	84
<b>5</b>	<b>Trapped ions</b>	<b>89</b>
5.1	Introduction . . . . .	90
5.2	Ion trapping . . . . .	90
5.3	Ion trap characterization . . . . .	93
5.4	State preparation and state detection . . . . .	94
5.4.1	Electronic state preparation . . . . .	94
5.4.2	Spin preparation and spin detection in ${}^{171}\text{Yb}^+$ . . . . .	96
5.5	Coherence time of the spin qubit . . . . .	98
5.6	Micromotion compensation . . . . .	103
5.6.1	Axial micromotion compensation . . . . .	105
5.6.2	Radial micromotion compensation . . . . .	106
5.7	Conclusions and outlook . . . . .	108

<b>6 Trapped atoms</b>	<b>111</b>
6.1 Introduction . . . . .	112
6.2 Sequence . . . . .	112
6.3 Elevation height measurement . . . . .	116
6.4 Conclusions and outlook . . . . .	117
<b>7 Observation of collisions between cold Li atoms and Yb<sup>+</sup> ions</b>	<b>119</b>
7.1 Introduction . . . . .	120
7.2 Experimental setup . . . . .	120
7.3 Experimental sequence . . . . .	122
7.4 Results . . . . .	123
7.4.1 Density profile of the atomic cloud . . . . .	123
7.4.2 Loss rates . . . . .	124
7.4.3 Energy dependence of loss rates . . . . .	125
7.5 Theory . . . . .	126
7.6 Conclusions . . . . .	128
<b>8 Summary and outlook</b>	<b>129</b>
<b>9 Samenvatting en vooruitzichten</b>	<b>133</b>
<b>A Yb<sup>+</sup></b>	<b>139</b>
<b>B <sup>6</sup>Li</b>	<b>143</b>
<b>C Construction manual of the ion trap</b>	<b>145</b>
<b>D Construction manual of the Feshbach coils</b>	<b>147</b>
<b>E Optical reference cavity</b>	<b>149</b>
<b>F Correction of interaction time for the <sup>2</sup>F<sub>7/2</sub> state</b>	<b>151</b>
<b>Acknowledgments</b>	<b>153</b>
<b>List of publications</b>	<b>157</b>
<b>Acronyms</b>	<b>159</b>
<b>Bibliography</b>	<b>161</b>



# 1 — Introduction

## **Trapped ions and ultracold atoms**

With the possibility to trap and observe well-localized single particles, trapped ions find application in precision spectroscopy and are of fundamental importance, for instance, in metrology [1, 2], quantum information [3–6], quantum simulation [7], optical frequency standards [8] and cold chemistry [9]. Due to the strong, repulsive Coulomb interactions, trapped ions form stable crystalline structures (Coulomb crystals) where the single ions are spatially localized. Inter-ion distances on the order of several micrometers allow for individual laser-addressing and state-detection. Additionally, the ions are routinely cooled (close) to their motional ground state. As state-of-the-art laser manipulation provides full control over the motional and internal degrees of freedom, trapped ions represent a remarkable few-body quantum system (for reviews see, e.g., Ref. [10, 11]).

In contrast, the inter-atom, short-range van der Waals interaction allows to trap dense clouds of millions of bosonic or fermionic atoms in magneto optical traps, magnetic traps, optical dipole traps or in optical lattices [12]. Ensembles of trapped atoms are routinely cooled to quantum degeneracy [13, 14] and allow for tuning their interactions via Feshbach resonances [15, 16]. As atomic quantum gases can be prepared in a specific internal state and feature long coherence times they represent an outstanding many-body quantum system finding application, for instance, in metrology [17], quantum information [18], quantum simulation [19] and optical frequency standards [8] (for reviews see, e.g., Ref. [20, 21]).

## **Combining many-body with few-body quantum systems**

Recent experiments on mixtures of ultracold atoms and ions [22–30] point the way towards realizing novel platforms for studying quantum many-body

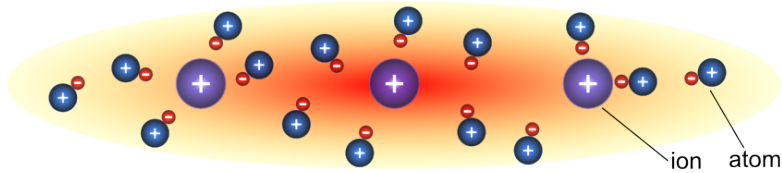


**Figure 1.1:** Sketch of an ion crystal immersed in a cloud of polarized atoms.

physics [31–33], ultracold collisions [22, 24, 30] and cold chemistry [25, 26, 34] and offer new applications (for reviews see Ref. [28, 35–40]). For example, by preparing and detecting the internal degrees of freedom of the ions and atoms we can characterize the atom-ion interactions allowing for initiating and thus for detecting fundamental chemical reactions on the single particle level. From this we can deduce the reaction products, reaction energies and branching ratios [25, 34].

In state-of-the-art experiments the temperature of a trapped atomic cloud is typically on the order of  $0.1\text{--}1\ \mu\text{K}$  while the ion temperature in a Paul trap is typically on the mK scale. Thus, an atomic cloud can be used to sympathetically cool an immersed ion crystal [23, 24, 30, 41].

Since the ions offer full control over their quantum state, we may use them to detect properties of the atomic system [42]. In particular, we could envision detecting the ion motion after it has interacted with the atoms.

Additionally, hybrid atom-ion systems could be used in quantum information applications. Examples include the possible implementation of quantum gates between atoms and ions which could serve as an interface between the two quantum systems [31, 43]. Furthermore, collisional cooling of the trapped ion quantum computer may allow for eliminating adverse heating that limits the fidelity of the quantum gates [44].

An ion crystal immersed in an ultracold cloud of fermionic atoms may be used as a quantum simulator of crystalline solids [45], in which the ions take the role of the crystal and the atoms resemble electrons. A very nice feature in such a system is that the ion crystal includes quantized sound waves (*phonons*) that may couple to the fermionic atoms via collisions. In this way, a key component of electronic matter – the fermion-phonon coupling – is naturally included in the quantum simulator [32]. Note that this feature is absent in the most commonly used atomic quantum simulator – atoms in optical lattices.

In a hybrid atom-ion experiment the trapping technologies for laser-cooled ions and ultracold atoms are merged in one experimental apparatus. The ions

are commonly trapped in a (linear) Paul trap [46, 47]. Here, spatial confinement of the particles is achieved with an oscillating radio frequency (rf) electric quadrupole field in two directions and a static electric field in the remaining direction. For most of the above ideas to work, it will be of fundamental importance to reach the so-called quantum or  $s$ -wave regime of atom-ion interactions [48]. However, a major roadblock towards reaching the quantum regime is formed by the time-dependent trapping field of the Paul trap, which limits attainable temperatures in hybrid atom-ion systems [23, 24, 30, 41, 49–53]. In particular, the micromotion of ions trapped in a rf trap may induce heating when short-range (Langevin) collisions with atoms occur. In reference [50], it was shown theoretically that the lowest temperatures may be reached for the largest ion-atom mass ratios  $m_i/m_a$ . The atom-ion combination with the highest mass ratio,  $m_i/m_a \approx 24$ –29, which allows for straightforward laser cooling is  $\text{Yb}^+/\text{Li}$ . This combination reaches the  $s$ -wave limit at a collision energy of  $k_B \cdot 8.6 \mu\text{K}$ , which should be in reach with current Paul traps and state-of-the-art excess micromotion compensation [54]. Up until now, nobody has investigated this combination in detail. Experimental studies have been limited to the combinations  $\text{Rb}/\text{Yb}^+$  [34],  $\text{Rb}/\text{Ba}^+$  and  $\text{Rb}/\text{Rb}^+$  [24],  $\text{Li}/\text{Ca}^+$  [55] and  $\text{Rb}/\text{Sr}^+$  [30] for atom clouds in the ultracold regime. Furthermore,  $\text{Yb}/\text{Yb}^+$  [22],  $\text{Rb}/\text{Ca}^+$  [25],  $\text{Ca}/\text{Yb}^+$  [26],  $\text{Ca}/\text{Ba}^+$  [56],  $\text{Na}/\text{Na}^+$  [57],  $\text{Na}/\text{Ca}^+$  [58],  $\text{Rb}/\text{K}^+$  and  $\text{Cs}/\text{Rb}^+$  [59] are studied with atoms cooled in magneto optical traps (mK regime).

### This thesis

In this PhD thesis, we describe the design and construction of an experimental apparatus capable of trapping, cooling and spatially overlapping neutral  ${}^6\text{Li}$  atoms and  $\text{Yb}^+$  ions. Our main goal is to reach the quantum regime in atom-ion mixtures and to investigate fundamental atom-ion scattering physics. In particular, we answer two important questions:

1. How does the atom-ion quantum simulator [32, 60] behave when we include micromotion in its theoretical description? To answer this question, we analyze in theory the quantum dynamics of an atom-ion quantum simulator *unit cell* in which a single atom interacts with a single trapped ion.
2. Is the combination  $\text{Yb}^+/\text{Li}$  suitable for the experimental applications intended? To find this out we experimentally establish if the chemical reaction rate in colliding  $\text{Li}$ – $\text{Yb}^+$  systems is low enough to allow for quantum applications and sympathetic cooling.

### Outline

In chapter 2 we provide the basic theory of atom-ion interactions and ion trapping in a Paul trap. With this knowledge we analyze the dynamics of an atom-ion system in a Paul trap following Ref. [50]. We see that the rf trapping field of the Paul trap adds energy to the system during a collision resulting in an increase of the total ion energy. This leads to an equilibrium ion energy setting a fundamental limit to the system depending only on the atom-ion mass ratio and the parameters of the trapping field.

Being a building block of the proposed atom-ion quantum simulator [32], we theoretically investigate the quantum dynamics of an ion-controlled atomic double-well system in chapter 3. Here, the coupling between the wells depends on the motional state of the ion which can be used to control and study the atom-ion interaction with high precision. We expand on previous calculations on this system [33, 61, 62] by including micromotion and analyze the effects of the so-called excess micromotion caused by trap imperfections. We find that the micromotion has a strong influence on the system and causes couplings to high-energy atom-ion scattering states. Those complicate accurate state preparation and may lead to heating. These effects can be mitigated by choosing an ion-atom combination with a large mass ratio and by choosing large interwell distances. Additionally, it is advisable to choose the double-well axis to be in the axial direction of the Paul trap as there is no micromotion (as we will make clear in chapter 2). In the case of excess micromotion we find that it has devastating effects on the system. Also here choosing a large ion-atom mass ratio helps but proper micromotion compensation is essential for the realization of such a system.

Trapping and cooling Li and  $\text{Yb}^+$  in the same physical location poses specific experimental challenges. In particular, trapping and cooling of  ${}^6\text{Li}$  requires high power laser fields and large (up to 800 G) magnetic fields at the location of the ions. Furthermore, the atoms are typically loaded from an atomic beam that may be harmful to the ion trap when aimed at it. Finally, to cool, trap and detect both, the atoms and ions, light fields of 8 different wavelengths in  $\sim 14$  beams have to be send into the experiment, requiring excellent optical access. In chapter 4 we give a detailed description on the experimental setup including the design of the hybrid trap setup and vacuum system as well as on the magnetic field coils, laser systems and imaging setup.

In order to characterize the setup, we present and analyze the sequences for trapping and initializing  $\text{Yb}^+$  ions and  ${}^6\text{Li}$  atoms in chapter 5 and chapter 6, respectively. This includes cooling, trapping and transport of the atoms as well as an analysis of the Paul trap in terms of trap frequencies and micromotion

compensation. We also show how the internal state of the ions can be prepared, manipulated and detected.

As  $\text{Li}/\text{Yb}^+$  is a favorable atom-ion combination for reaching the quantum regime, it is essential to understand the  $(\text{Li}-\text{Yb})^+$  molecular system. In chapter 7 we report on cold collisions in our system. We find that, when we prepare the  $\text{Yb}^+$  ion in its electronic ground state, less than one in a thousand Langevin collisions results in a chemical process such that sympathetic cooling and using the system for quantum applications should be realizable. We also study these collisions with the ions prepared in excited electronic states. Here, we observe charge transfer after a few collisions. The  $4f$  shell in the  $\text{Yb}^+$  ion prevents an exact theoretical prediction of such processes using standard methods of quantum chemistry. Thus, accurate measurements of chemical reactions between individual particles with full control over their energy and internal states provide an excellent test bed for *ab initio* molecular structure calculations [63, 64].

Finally, we summarize the results obtained in this thesis and discuss possible improvements on the setup in chapter 8.



## 2 — Theoretical foundations

In this chapter we provide the basic theory of atom-ion interactions and ion trapping in a Paul trap and discuss the dynamics of an atom-ion system in a Paul trap.

## 2.1 Introduction

In our experiment we investigate the dynamics of trapped atom-ion systems at cold and ultracold temperatures. Thus, the fundamental theory of atom-ion interactions and collisions in the classical and quantum regime is of key interest. This chapter gives a brief overview of the main topics. In section 2.2 we investigate atom-ion interactions. With  $R$  being the atom-ion separation we discuss the leading  $R^{-4}$  term of the interaction potential and atom-ion collisions. The dynamics of ions trapped in a linear Paul trap are investigated in section 2.3. Here, we not only describe trapped ions but also the effects of the Paul trap on trapped atom-ion systems.

## 2.2 Atom-ion interaction

In the last two decades the dynamics of atom-ion systems have been studied in numerous theoretical publications, see, e.g., Ref. [31, 35, 48, 63, 65–68].

### 2.2.1 Atom-ion interaction potential

Within the Born-Oppenheimer approximation the interaction between an atom and an atomic ion is defined by the energy difference between the total energy of the atom-ion complex ( $E_{\text{atom-ion}}$ ) and the total energy of the interacting atom ( $E_{\text{atom}}$ ) and ion ( $E_{\text{ion}}$ ) [69]:

$$V(R) = E_{\text{atom-ion}}(R) - (E_{\text{atom}} + E_{\text{ion}}) , \quad (2.1)$$

with the atom-ion separation  $R$ . By calculating  $V(R)$ , potential energy curves for the ground and excited states of the atom-ion complex (as in figure 7.4) can be obtained [68, 69]. An atom-ion interaction potential is schematically shown in figure 2.1 (a). Here, the long-range asymptotic of  $V(R)$  expressed in multipole expansion is given by [68]<sup>1</sup>

$$V(R) = -\frac{C_4^{\text{ind}}}{R^4} - \frac{C_6^{\text{ind}}}{R^6} - \frac{C_6^{\text{disp}}}{R^6} + \dots \quad (2.2)$$

The dominant two-body interaction between a neutral, nonpolar atom, as  ${}^6\text{Li}$ , and an atomic ion, as  $\text{Yb}^+$ , is due to ion-induced dipole forces. For an atom at

---

<sup>1</sup>The terms scaling with  $R^{-1}$  (Coulomb),  $R^{-2}$ (charge-dipole) and  $R^{-3}$ (charge-permanent electric quadrupole moment) vanish.

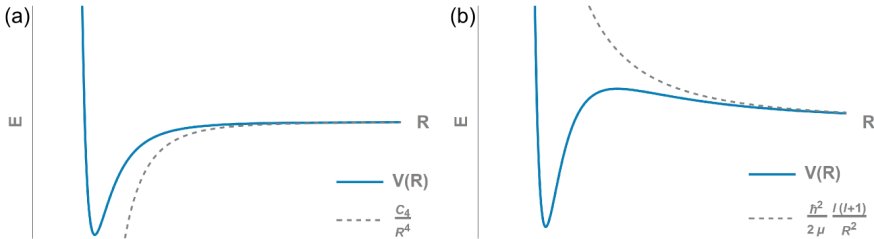


**Figure 2.1:** Atom-ion interaction potential  $V(R)$  (a) for  $s$ -wave scattering with  $l = 0$  and (b) for scattering with  $l \neq 0$ . At short distances higher order terms in equation (2.2) as exchange forces and dispersion start dominating and  $V(R)$  becomes strongly repulsive. For higher partial waves  $V(R)$  is superimposed with a centrifugal barrier effectively shielding  $V(R)$  from  $s$ -wave scattering with low-energy particles [15].

distance  $R$  from an ion, the electric field of the ion  $E(R) = Q/(4\pi\epsilon_0 R^2)$  induces an electric dipole moment  $p_{\text{ind}}$  in the atom, given by [70]

$$p_{\text{ind}} = \alpha \cdot E(R) = \frac{\alpha Q}{4\pi\epsilon_0 R^2}, \quad (2.3)$$

with  $\alpha$  the isotropic static electric dipole polarizability of the atom. This polarizability characterizes the displacement of the neutral atom's electron cloud relative to the positively charged atom nucleus and thus depends on the electronic state of the atom. Consequently, the attractive atom-ion polarization potential  $V^{\text{ind}}(R)$  is of the form [71]

$$V^{\text{ind}}(R) = -\frac{1}{2}\alpha E^2(R) = -\frac{\alpha Q^2}{2(4\pi\epsilon_0)^2 R^4} = -\frac{C_4}{R^4}, \quad (2.4)$$

with  $C_4 = \alpha Q^2/2(4\pi\epsilon_0)^2$  the long-range coefficient of the ion-induced charge-dipole interaction<sup>2</sup>. The second and third term in equation (2.2) scaling with  $R^{-6}$  are due to the interaction between the ion charge and the induced electric quadrupole moment in the atom ( $-C_6^{\text{ind}}R^{-6}$ ), and the dispersion interaction ( $-C_6^{\text{disp}}R^{-6}$ ).

In order to characterize the atom-ion dynamics, it is useful to define a characteristic length scale  $R^*$  and energy scale  $E^*$  of the interaction. By equating

<sup>2</sup>For ( ${}^6\text{Li}+\text{Yb}^+$ ):  $C_4 = 82.0935 E_h a_0^4 = 2.8066 \times 10^{-57} \text{ J}\cdot\text{m}^4$ , with  $E_h$  and  $a_0$  the Hartree energy and Bohr radius, respectively [63].

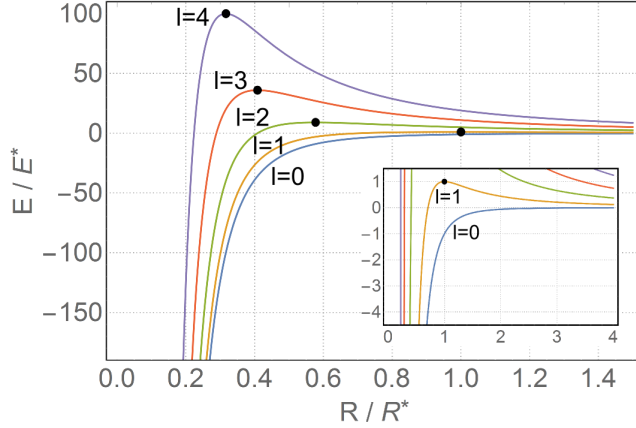


**Figure 2.2:** Long-range atom-ion potential  $V_{\text{eff}}(R)$  for partial waves  $l = 0, 1, 2, 3, 4$  in units of  $R^*$  and  $E^*$ . The black disks mark the centrifugal barrier for  $l \neq 0$  (adapted from [48]).

$E_{\text{kin}} = V^{\text{ind}}(R)$  we get [31]

$$R^* = \sqrt{\frac{2\mu C_4}{\hbar^2}} \quad \text{and} \quad E^* = \frac{\hbar^2}{2\mu(R^*)^2}, \quad (2.5)$$

with  $\mu = m_{\text{atom}}m_{\text{ion}}/(m_{\text{atom}} + m_{\text{ion}})$  the reduced mass. For  $l \neq 0$  scattering the potential features a centrifugal barrier as shown in figure 2.1 (b). The effective potential is then given by [31]

$$V_{\text{eff}}(R) = -\frac{C_4}{R^4} + \frac{\hbar^2 l(l+1)}{2\mu R^2}. \quad (2.6)$$

For the position and height of the centrifugal barrier we find

$$R_l^{\text{max}} = \sqrt{\frac{2}{l(l+1)}} R^* \quad \text{and} \quad E_l^{\text{max}} = \frac{l^2(l+1)^2}{4} E^*. \quad (2.7)$$

Consequently,  $R^*$  specifies the position of the centrifugal barrier of the potential for  $p$ -wave collisions ( $l = 1$ ) and thus sets the length scale of the interaction. For atom-ion collisions it is much larger than the length scale of the van der Waals interaction for neutral atom-atom collisions. The energy scale  $E^*$  defines the height of this barrier and is much smaller as for neutral atom-atom

collisions. The  $s$ -wave scattering regime is reached at relative kinetic energies of the atom-ion system smaller than  $E^*$ . The values for  $E^*$  of common atom-ion combinations range from 0.01–10  $\mu\text{K}$  which is hard to achieve even with state-of-the-art ion cooling techniques. For ( ${}^6\text{Li}+{}^{171}\text{Yb}^+$ )  $R^* = 69.75$  nm and  $E^* = k_B \times 8.58$   $\mu\text{K}$ , with  $k_B$  the Boltzmann constant<sup>3</sup>. The long-range part of the atom-ion potential in units of  $R^*$  and  $E^*$  for  $l = 0$  and also for higher partial waves  $l$  is shown in figure 2.2.

### 2.2.2 Atom-ion collisions

In the ultracold regime, at very low collision energies  $E_{\text{col}} < E^*$ , atom-ion dynamics are determined by the  $s$ -waves. Here, the short-range interactions have to be taken into account as described, e.g., in Ref. [48, 66]. The cold atom-ion collision experiments presented in chapter 7 are performed at slightly higher energies  $E_{\text{col}} > E^*$ . Here, the scattering dynamics are determined by the asymptotic part of the long-range potential and the centrifugal barrier and can be described (semi-)classically.

In the center-of-mass frame, the orbits of the colliding atom and ion depend on the collision energy  $E_{\text{col}}$  and on the impact parameter  $b$  which is the shortest distance between the unperturbed initial orbits (without atom-ion interaction). By defining the critical impact parameter  $b_c = (4C_4/E_{\text{col}})^{1/4}$ , we can distinguish between two types of collisions. For  $b > b_c$  the trajectories of the colliding particles do not cross the centrifugal barrier. Those so-called *glancing collisions* typically only lead to weak deflection of the collision partners and thus to small momentum transfer. For  $b < b_c$  the particles overcome the centrifugal barrier and enter into an inward-spiraling orbit resulting in so-called *Langevin collisions*. Here, a significant amount of energy can be transferred between the atom and ion. While glancing collisions are purely elastic, Langevin collisions may result in elastic, inelastic or reactive scattering processes. From the Langevin cross section  $\sigma_L = \pi b_c^2$  we determine the collision energy-independent rate for Langevin collisions to be  $\gamma_L = 2\pi\rho_a\sqrt{C_4/\mu}$ , with  $\rho_a$  the density of atoms at the ion position [72, 73].

---

<sup>3</sup>  $R^*$  and  $E^*$  values for various combinations of atom-ion species can be found, e.g., in Ref. [40, 62].

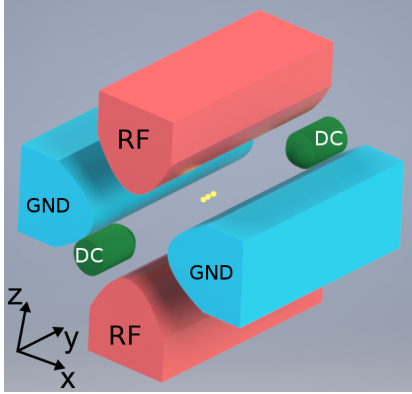


**Figure 2.3:** Schematic electrode configuration of a linear Paul trap. The quadrupole potential between the rf blade electrodes (RF) and grounded blade electrodes (GND) provides radial confinement of the ions in  $x$ - and  $z$ -direction while a static direct current (dc) potential generated by additional end cap electrodes (DC) provides axial confinement in  $y$ -direction.

## 2.3 The linear Paul trap

As an ion trap we use a linear Paul trap [47] as shown in figure 2.3. Here, we spatially overlap trapped  $\text{Yb}^+$  ions with a cloud of trapped  ${}^6\text{Li}$  atoms.

### 2.3.1 Trapped ions in a Paul trap

An ion trap is a device that allows for spatial confinement of charged particles over a long period of time isolated from environmental influences. The underlying principle is, that a charged particle in an inhomogeneous, oscillating rf field experiences a *ponderomotive force* accelerating the particle towards the weak field direction [46, 74].

In a linear Paul trap the rf trapping field confines the ion in radial direction while a static electric field traps the ion in axial direction. Linear Paul traps offer the possibility to trap crystals of multiple ions in linear, planar or three-dimensional structures [75]. Additionally, for atom-ion experiments the controlled overlapping of atoms and ions is simplified since separate tuning of the end cap voltages provides axial alignment of the ion position.

In a linear Paul trap the trapping electric field near the trap axis generated by the rf periodic quadrupole field in radial directions  $x$  and  $z$  and the static electric field in axial direction  $y$  is [76]

$$\mathbf{E}(\mathbf{r}, t) = \mathbf{E}_{\text{dc}}(\mathbf{r}) + \mathbf{E}_{\text{rf}}(\mathbf{r}, t) \quad (2.8)$$

with

$$\mathbf{E}_{\text{dc}}(\mathbf{r}) = \frac{U_{\text{dc}}}{y_0^2} \begin{pmatrix} \kappa_x x \\ -2\kappa_y y \\ \kappa_z z \end{pmatrix}, \quad (2.9)$$

$$\mathbf{E}_{\text{rf}}(\mathbf{r}, t) = \frac{U_{\text{rf}}}{r_0^2} \begin{pmatrix} -\kappa'_x x \\ 0 \\ \kappa'_z z \end{pmatrix} \cos(\Omega t). \quad (2.10)$$

Here, the geometrical factors  $\kappa_r < 1$  and  $\kappa'_r < 1$  ( $r = x, y, z$ ) depend on the trap electrode geometry and  $\Omega$  is the rf trap drive frequency. A single ion of charge  $Q$  and mass  $m_i$  in the electric field (2.8) experiences the Lorentz force  $\mathbf{F}_L(\mathbf{r}, t) = Q\mathbf{E}(\mathbf{r}, t)$  and thus the classical equations of motion can be derived:

$$\ddot{x} - \frac{Q}{m_i} \left( \frac{\kappa_x U_{\text{dc}}}{y_0^2} - \frac{\kappa'_x U_{\text{rf}}}{r_0^2} \cos(\Omega t) \right) x = 0 \quad (2.11)$$

$$\ddot{y} + \frac{2Q\kappa_y U_{\text{dc}}}{m_i y_0^2} y = 0 \quad (2.12)$$

$$\ddot{z} - \frac{Q}{m_i} \left( \frac{\kappa_z U_{\text{dc}}}{y_0^2} + \frac{\kappa'_z U_{\text{rf}}}{r_0^2} \cos(\Omega t) \right) z = 0 \quad (2.13)$$

We note that the motion along the  $x$ ,  $y$  and  $z$  axes are decoupled. These differential equations can be transformed into the canonical form of *Mathieu's differential equation*

$$\frac{\partial^2 \mathbf{r}_r}{\partial \tau^2} + [a_r - 2q_r \cos(2\tau)] \mathbf{r}_r = 0 \quad (r = x, y, z), \quad (2.14)$$

by substituting  $\tau = \frac{\Omega}{2}t$  and

$$a_x = a_z = -\frac{1}{2}a_y = -\frac{4QU_{\text{dc}}\kappa_r}{m_i\Omega^2 y_0^2}, \quad (2.15)$$

$$q_x = -q_z = \frac{2QU_{\text{rf}}\kappa'_r}{m_i\Omega^2 r_0^2}, \quad q_y = 0, \quad (2.16)$$

with typically  $|q| \ll 1$  and  $|a| \ll q^2$  [49]. As the parameters  $a$  and  $q$  have fixed values those Mathieu equations are periodical in time and thus can be solved by employing Floquet theory. The lowest-order approximation to the solutions are then given by [10]:

$$\mathbf{r}_r(t) \approx 2A \cos\left(\beta_r \frac{\Omega}{2}t + \phi_r\right) \left[1 - \frac{q_r}{2} \cos(\Omega t)\right] \quad (2.17)$$

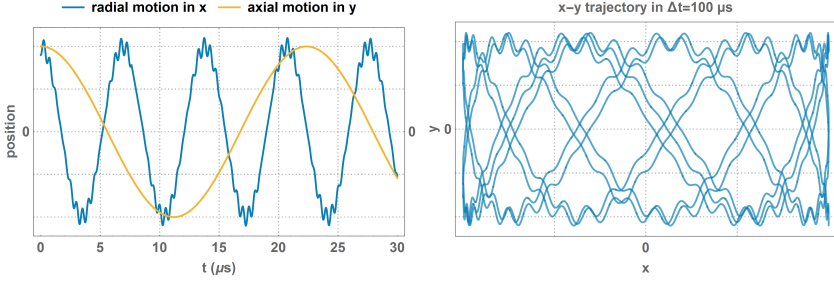


**Figure 2.4:** Radial and axial trajectory of a  $^{174}\text{Yb}^+$  ion in a Paul trap with  $A = 1$ ,  $\Omega = 2\pi \times 2 \text{ MHz}$ ,  $a_x = 0.001$  and  $q_x = 0.2$  yielding trap frequencies of  $\omega_x = 2\pi \times 145 \text{ kHz}$  and  $\omega_y = 2\pi \times 45 \text{ kHz}$ .

with

$$\beta_r \approx \sqrt{a_r + \frac{q_r^2}{2}}. \quad (2.18)$$

Here,  $A$  is an arbitrary constant and may be used to satisfy boundary conditions or for normalization of a particular solution. Figure 2.4 shows the solution in radial  $x$  and axial  $y$  direction for a  $^{174}\text{Yb}^+$  ion with  $A = 1$ ,  $\Omega = 2\pi \times 2 \text{ MHz}$ ,  $a_x = 0.001$  and  $q_x = 0.2$ . The motion of the charged particle in the Paul trap is composed of a *secular motion* at trap frequency

$$\omega_{i,r} = \beta_r \frac{\Omega}{2} \approx \frac{\Omega}{2} \sqrt{a_r + \frac{q_r^2}{2}} \quad (2.19)$$

and with phase  $\phi_r$  which, in radial direction, is superimposed with a driven motion at trap drive frequency  $\Omega \gg \omega_{i,r}$ , the so-called *micromotion* (*MM*). When treating the motion in the harmonic approximation, equation (2.17) is averaged over the short time period  $2\pi/\Omega$  such that the *MM* term vanishes and the residual motion of the particle is the harmonic secular motion with frequency  $\omega_{i,r}$ . This treatment is useful for the description of pure ion dynamics but is insufficient when solving the atom-ion problem.

In the quantum-mechanical picture as applied in chapter 3, the motion of a charged particle in the electric field of a Paul trap is governed by the Schrödinger equation

$$i\hbar \frac{\partial}{\partial t} \Psi(\mathbf{r}_r, t) = H_r(t) \Psi(\mathbf{r}_r, t). \quad (2.20)$$

In analogy to the classical picture the problem for each axis is decoupled such that we can separate the three-dimensional problem in three one-dimensional

problems with the Hamiltonian [10]

$$H_r(t) = \frac{\mathbf{p}_{i,r}^2}{2m_i} + \frac{1}{8}m_i\Omega^2\mathbf{r}_r^2 [a_r + 2q_r \cos(\Omega t)] , \quad (2.21)$$

with  $\mathbf{p}_{i,r}$  the momentum of the ion.

### 2.3.2 Trapped atom-ion systems in a Paul trap

The dynamics of trapped ions in a Paul trap spatially overlapped with a cloud of trapped atoms have proven to be very complex and have been investigated theoretically and experimentally in numerous publications in the classical and quantum regime [30, 49–51, 67, 77–81].

In a first approach, the simplified model of one-dimensional, purely elastic hard core collisions between an ion and a stationary atom were considered classically [77]. As explained in the previous section, the motion of a trapped ion in a Paul trap in radial direction is composed of a slow secular motion superimposed with a driven MM at the rf trap drive frequency. A trapped ion immersed in an atomic cloud frequently collides with the surrounding atoms. Those sudden interruptions of the ion motion lead to an energy exchange between the rf field and the secular motion of the ion. It is found that at a critical ion-atom mass ratio  $m_i/m_a = \xi_c$  the system experiences a transition from heating to cooling dynamics. For very small mass ratios  $m_i/m_a \ll \xi_c$  collisions lead to rf heating of the ions resulting in ion loss, while for large mass ratios  $m_i/m_a \gg \xi_c$  collisions lead to a decrease of the ion's mean kinetic energy which is essential for sympathetic cooling [51, 67, 78, 79]. This dependency on the rf MM suggests that the temperature of an ion, perfectly trapped at the center of the rf node and thus only experiencing negligible MM is determined by the thermal distribution of the atoms. For an experiment it is therefore advisable to restrict the collisions to the center of the ion trap [67] or to use higher order pole ion traps which have a flat potential at the center and thus only small MM amplitudes [79].

In Ref. [50] the long-range  $R^{-4}$  atom-ion potential (see section 2.2) is included into the theoretical description of the classical problem. They find that for atom-ion collisions even with the atoms at zero temperature and the ion perfectly trapped at the rf node the efficiency of sympathetic cooling is fundamentally limited. A result of their calculations is that two processes alter the mean kinetic energy of the ion: Firstly, the attractive atom-ion interaction potential  $V(R)$  given in equation (2.2) pulls the ion out of the rf node which at the final hard-core collision leads to energy exchange as stated above. Secondly, as

the ion is pulled from the rf node towards the atom directly before and after the collision the ion motion is non-adiabatic relative to the rf trapping potential of the Paul trap. During this period the rf field can be seen as a time-dependent perturbation to the effective atom-ion potential which does work on the ion leading to an increase of its mean kinetic energy. Here, the characteristic scale for the work done on the ion is given by [50]

$$W_0 = 2 \left( \frac{m_a}{m_i + m_a} \right)^{5/3} \left( \frac{m_i^2 \omega_i^4 C_4}{q^2} \right)^{1/3}, \quad (2.22)$$

with  $m_a$  ( $m_i$ ) the mass of the atom (ion),  $\omega_i$  the secular trap frequency of the ion given in equation (2.19) and the trap parameter  $q$  given in equation (2.16). It turns out that the change of the ion's mean energy due to the work done during the non-adiabatic motion dominates over the energy exchange due to the collision itself. This has also been experimentally shown in Ref. [30] for Rb/Sr<sup>+</sup>. From equation (2.22) it can be seen that this heating effect should be mitigated by choosing a large ion-atom mass ratio  $m_i/m_a$ .

### 3 — Quantum dynamics of an atomic double-well system interacting with a trapped ion

We analyze theoretically the quantum dynamics of an atomic double-well system interacting with a single trapped ion<sup>1</sup>. We find that the atomic tunneling rate between the wells depends on both, the spin of the ion via the short-range spin-dependent atom-ion scattering length and its motional state with tunneling rates reaching hundreds of Hertz. This phonon-atom coupling is of interest for creating atom-ion entangled states and may form a building block in constructing a hybrid atom-ion quantum simulator. We analyze the role of micromotion (MM) when the ion is trapped in a Paul trap. We find that the MM causes couplings to high-energy atom-ion scattering states, preventing accurate state preparation and complicating the double-well dynamics. We conclude that the adverse effects of MM can be mitigated by choosing ion-atom combinations with a large mass ratio and by limiting the system to large interwell distances. In either case, accurate MM compensation would be required.

---

<sup>1</sup>Parts of this chapter were published as *Quantum dynamics of an atomic double-well system interacting with a trapped ion* by J. Joger, A. Negretti and R. Gerritsma, Phys. Rev. A **89**, 063621 (2014) [82].

### 3.1 Introduction

The excellent coherent controllability of the trapped ions' quantum states together with the near-perfect state preparation and state readout may allow for experiments in which ions *control* the dynamics of ultracold atoms. For instance, in Ref. [31] a hybrid quantum information processor is proposed in which quantum gate operations are performed by means of a controlled collision between a single trapped atom and ion. Here, the spin-dependence of the atom-ion scattering length can be used to obtain a state-dependent collisional phase shift, leading to the desired quantum logic [83,84]. Recently, our group expanded on this idea and calculated that a similar controllability of the interaction should arise when the ion is tightly trapped in the center of an atomic Josephson junction [61]. In such a setup the atomic tunneling rate between the wells of the double-well potential depends both, on the spin of the ion via the short-range spin-dependent atom-ion scattering length and on its motional state. Since the ion could in this way control many-body dynamics, mesoscopic entanglement between the atomic matter wave and the spin of the ion may be created. The interplay between the spin-dependent tunneling and the interatomic interactions could also result in superpositions of quantum self-trapping [85] and Josephson tunneling. Single, neutral impurities have also been proposed as a means to control and measure the dynamics in Josephson junctions, but these typically lack the superb controllability offered by the trapped ion system [86,87].

Including a single trapped ion expands on the rich dynamics of the Josephson junction as described in numerous experimental and theoretical works [85, 88–96]. Furthermore, the system may be seen as a ‘unit cell’ for a larger scale hybrid atom-ion quantum simulator [32]. Constructing such a device by concatenating ion-controlled double-wells could be a natural way to combine quantum simulators in which atoms can tunnel between sites in an optical lattice [19] with simulators employing the pseudo-spin and collective motional states of ion crystals [7]. In such a system, atomic Bloch waves would interact with phononic excitations in the ion crystal, leading to solid state phenomena such as Peierls instabilities [32,97] and phonon-mediated interactions.

Ref. [61] solved the atomic dynamics in the ion-controlled double-well system by assuming that the ion is pinned to the center of its trap. This simplification is based on the experimentally realistic case that the ion is trapped much more tightly than the atom in the double-well potential. In Ref. [62] we investigated as a second step how the simple secular dynamics of the ion in a harmonic trapping potential change the picture obtained in Ref. [61]. Here, we find that

the tunneling dynamics depend also on the motional state of the ion.

In this thesis, I expand on the results obtained in my Diploma thesis [62] by considering the effects of the ion’s intrinsic micromotion (MM) in a Paul trap. It has been shown that MM significantly changes the dynamics of the proposed atom-ion quantum gate [31], as described in Ref. [49], leading to slower gates or requiring additional control pulses. MM has also been shown to limit attainable temperatures for ions that are sympathetically cooled by atoms [41, 50]. Here, I show that in the case of the ion-controlled atomic double-well system the MM causes difficulties in state-preparation and complicates the atomic tunneling for large tunneling rates, i.e. small interwell separations. We find that using an atom-ion combination with a large mass ratio, with the ion being the heavier particle, allows to overcome such difficulties. This conclusion is in line with a recent classical analysis studying attainable temperatures in atom-ion sympathetic cooling [50].

This chapter is based on our publication [82] and additionally investigates the effects of so-called axial MM caused by imperfections often observed in real Paul traps. In section 3.2 the setup is introduced in which an atom is trapped in a double-well potential with a single ion trapped in its center as shown in Fig. 3.1. For the sake of completeness, in section 3.3 we briefly revisit the simplified case where the ion is pinned to the center of the trap described in Ref. [62] before the effects of a moving ion in a harmonic trapping potential are investigated in section 3.4. In section 3.5 the solutions to the atomic double-well in the presence of a time-dependent trapping potential for the ion and the effect of MM are discussed. Here, we will expand on the previous considerations by investigating the impact of axial micromotion on the ion-controlled double-well system, which was not included in [82].

### 3.2 Atomic double-well in presence of an ion

We consider a system with a single ion trapped in the tight potential of a Paul trap and a single atom trapped in a double-well potential as shown in figure 3.1. The Hamiltonian of such a system is given by

$$H = H_i + H_a + H_{ia} . \tag{3.1}$$

The first term in equation (3.1) is the effective Hamiltonian of an ion in the harmonic potential of a Paul trap (see chapter 2.3.1). The second term is the

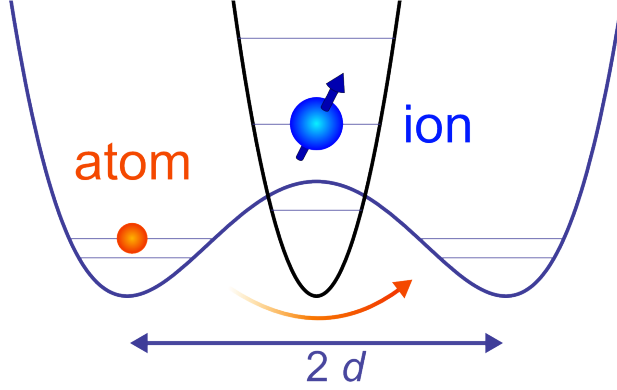


**Figure 3.1:** Atomic double-well system interacting with a single trapped ion. The tunneling rate of the atom between the potential wells depends on the internal spin state of the ion and on the interwell distance  $2d$ .

Hamiltonian for an atom in the double-well potential  $V_{\text{DW}}$  and is given by

$$H_a = \frac{p_a^2}{2m_a} + V_{\text{DW}}(z_a). \quad (3.2)$$

Here,  $p_a$ ,  $m_a$  and  $z_a$  denote the momentum, mass and position of the atom, respectively. We use the double-well potential [98]

$$V_{\text{DW}}(z_a) = \frac{b}{d^4}(z_a^2 - d^2)^2, \quad (3.3)$$

with the interwell barrier  $b$ , minima at  $z_a = \pm d$  and the atom's local trapping frequencies of  $\omega_a = \sqrt{8b/m_a d^2}$ . We fix  $\omega_a$  for each interwell distance  $2d$  by setting

$$b = \frac{1}{8}\omega_a^2 m_a d^2. \quad (3.4)$$

Without loss of generality this simplification enables us to change the interwell distance without changing the local trapping frequency. The third term in equation (3.1) is the atom-ion interaction term which we derived in chapter 2.2.

### 3.3 Static ion in one dimension

In Ref. [61] and [62] a simplified case for the system is considered first, assuming that the ion is ground state cooled and that it is trapped much more tightly than the atom, with  $\omega_i \gg \omega_a$ . Furthermore, the Paul trap's intrinsic MM is neglected. Under these assumptions the ion can be treated as if it would be pinned to the center of the ion trap potential at  $z_i = 0$  and the term  $H_i$  in equation (3.1) can be neglected.

For the sake of completeness, we first redo the calculations for this simplified case in a similar manner. It will allow us to explain the basic ingredients of our setup and the ideas behind our numerical approach.

We write the Hamiltonian as  $H_a = H_a^{(0)} + H_a^{(1)}$  with

$$H_a^{(0)} = \frac{\hbar^2}{2m_a} \frac{\partial^2}{\partial z_a^2} + \frac{1}{2} m_a \omega_a^2 z_a^2 - \frac{C_4}{z_a^4}, \quad (3.5)$$

$$H_a^{(1)} = \frac{1}{8} m_a \omega_a^2 \left( \frac{z_a^4}{d^2} - 2z_a^2 + d^2 \right) - \frac{1}{2} m_a \omega_a^2 z_a^2. \quad (3.6)$$

In order to solve the Schrödinger equation for  $H_a$  we expand the solutions onto the eigenstates of  $H_a^{(0)}$ . The harmonic potential term  $m_a \omega_a^2 z_a^2 / 2$  was added in  $H_a^{(0)}$  and subtracted again in  $H_a^{(1)}$ . In this way,  $H_a^{(0)}$  has a discrete set of eigenstates and eigenenergies. This simplifies the calculation and is advantageous as the solution of  $H_a$  forms a discrete set as well [61].

We solve the Schrödinger equation for the Hamiltonian  $H_a^{(0)}$  by means of quantum defect theory (QDT) [48]. In this way, we can deal with the short-range behavior of the interaction potential which starts deviating from  $C_4/z_a^4$  and becomes strongly repulsive. An appropriate parametrization of the short-range dynamics can be employed by introducing a set of energy-independent terms, the short-range phases, as has been shown in Ref. [65]. Accordingly, for  $z_a \rightarrow 0$  the energy is dominated by the term  $-C_4/z_a^4$  and at short distances the behavior of the relative wave functions is governed by the even and odd solutions

$$\tilde{\psi}_e(z_a) \propto |z_a| \sin \left( \sqrt{\frac{m_a}{\mu}} \frac{R^*}{|z_a|} + \phi_e \right), \quad (3.7)$$

$$\tilde{\psi}_o(z_a) \propto z_a \sin \left( \sqrt{\frac{m_a}{\mu}} \frac{R^*}{|z_a|} + \phi_o \right), \quad (3.8)$$

where  $\phi_e$  and  $\phi_o$  are the even and odd short-range phases, respectively. Those are related to the singlet and triplet scattering length and therefore depend on the relative spin orientation of the atom and ion. They are neither known experimentally nor can they be reliably obtained from *ab initio* calculations. Therefore, we choose a number of realistic values, corresponding to scattering lengths in the range  $-R^*$  to  $R^*$ . We note that in an experiment we can tune these values by external confinement or with magnetic fields, e.g. in a quasi 1D-setup: by changing the confinement in the two remaining dimensions [31,65,66].

The Schrödinger equation

$$H_a^{(0)}\Phi_k^{(0)}(z_a) = \mathcal{E}_k^{(0)}\Phi_k^{(0)}(z_a) \quad (3.9)$$

is solved numerically by making use of the renormalized Numerov method [99]. Here, we determine the solutions  $\Phi_k^{(0)}(z_a)$  with energies  $\mathcal{E}_k^{(0)}$  and quantum number  $k$  by using the equations (3.7) and (3.8) as boundary conditions at minimal distance  $r_{\min}$ , so that  $C_4/z_{a,\min}^4 \gg E_{\max}$ , where  $E_{\max}$  is the largest energy considered in the problem [31]. In order to diagonalize the full Hamiltonian  $H_a$ , the Schrödinger equation

$$\left(H_a^{(0)} + H_a^{(1)}\right)\Phi_k^{(d)}(z_a) = \mathcal{E}_k^{(d)}\Phi_k^{(d)}(z_a) \quad (3.10)$$

has to be solved. For this we follow the argumentation in Ref. [31] by choosing the orthonormal basis

$$\Phi_k^{(d)}(z_a) = \sum_k c_k \Phi_k^{(0)}(z_a). \quad (3.11)$$

By substituting equation (3.11) into (3.10) and with (3.9) we obtain

$$\sum_k c_k \mathcal{E}_k^{(0)} \Phi_k^{(0)}(z_a) + \sum_k c_k H_a^{(1)} \Phi_k^{(0)}(z_a) = \sum_k c_k \mathcal{E}_k^{(d)} \Phi_k^{(0)}(z_a). \quad (3.12)$$

Now we insert  $H_a^{(1)}$ , multiply with  $\left(\Phi_{k'}^{(0)}(z_a)\right)^*$  from the left and integrate over  $z_a$ :

$$\begin{aligned} & \delta_{kk'} c_{k'} \left( \mathcal{E}_k^{(0)} + \frac{1}{8} m_a \omega_a^2 d^2 \right) + \frac{m_a \omega_a^2}{4} \sum_k c_k \int dz_a \left( \Phi_{k'}^{(0)}(z_a) \right)^* \left( \frac{z_a^4}{2d^2} - 3z_a^2 \right) \Phi_k^{(0)}(z_a) \\ & = \mathcal{E}_k^{(d)} c_{k'}. \end{aligned} \quad (3.13)$$

With the matrix elements

$$\mathcal{M}_{kk'}^{(j)} = \int dz_a \left( \Phi_{k'}^{(0)}(z_a) \right)^* z_a^j \Phi_k^{(0)}(z_a) \quad (3.14)$$

equation (3.13) can be written in the form of a matrix equation

$$\sum_k H_{kk'} c_k = \mathcal{E}_k^{(d)} c_{k'} , \quad (3.15)$$

with

$$H_{kk'} = \delta_{kk'} \left( \mathcal{E}_k^{(0)} + \frac{1}{8} m_a \omega_a^2 d^2 \right) + \frac{m_a \omega_a^2}{4} \left( \frac{\mathcal{M}_{kk'}^{(4)}}{2d^2} - 3\mathcal{M}_{kk'}^{(2)} \right) . \quad (3.16)$$

As in Ref. [61] and [62], we diagonalize the Hamiltonian (3.16) for an example system consisting of a  $^{87}\text{Rb}$  atom and a  $^{171}\text{Yb}^+$  ion. For this atom-ion combination we obtain  $R^* = 306 \text{ nm}$  and  $E^*/h = 935 \text{ Hz}$  [100]. The corresponding correlation diagram, describing the dynamics in the system, is shown in figure 3.2 a) with  $\omega_a = 2\pi \times 1.8 \text{ kHz}$  and by taking 106 basis states into account. Here, the energy spectrum of the system is plotted against the interwell separation  $d$ . It characterizes the relation of the asymptotic vibrational states for large  $d$  to the molecular and vibrational states when  $d \rightarrow 0$ .

At large interwell separations there is no coupling between the wells. Here, the asymptotic vibrational states resemble those of a harmonic oscillator with equidistant,  $d$ -independent eigenenergies. As  $d$  is reduced, the coupling between the wells gets stronger, which results in a splitting of the energy levels in two. This is due to an energy difference between states with symmetric (ground) and antisymmetric (excited) combinations of the wave packets in the two wells, given by:  $\Phi_{g,e}(d) = \frac{1}{\sqrt{2}} (\Phi_L(d) \pm \Phi_R(d))$ . Here, we denote the left (right) wave packet with  $\Phi_{L(R)}$  and the corresponding energies with  $E_{e(g)}$  for ground (excited) superpositions, respectively.

In the two mode picture, this energy difference corresponds to the tunneling rate  $J/h = (E_e - E_g)/h$  of a single atom which depends on the coupling between the local modes [70, 98].

In figure 3.2 b) the dependency of the tunneling rate to the interwell separation  $d$  is plotted. At  $d = 900 \text{ nm}$  the ground-state degeneracy is lifted corresponding to a tunneling rate of  $J/h = 56 \text{ Hz}$ , when  $\phi_{e/o} = \mp\pi/4$  (black lines) and  $J/h = 202 \text{ Hz}$ , when  $\phi_{e/o} = \mp\pi/3$  (dashed blue lines). This is in analogy to the spin-dependent rates obtained in Ref. [61] and [62].

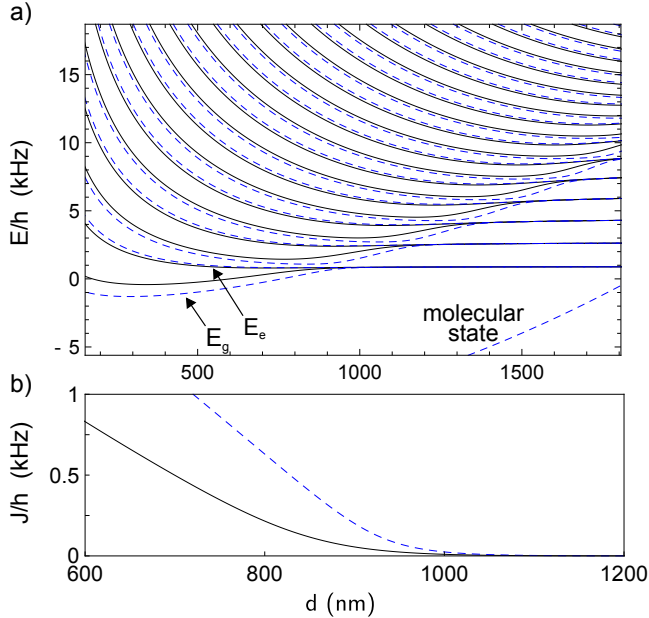


**Figure 3.2:** Results for a double-well system with a  $^{87}\text{Rb}$  atom and a spatially static  $^{171}\text{Yb}^+$  ion. (a) Correlation diagram: Energy spectrum as a function of the interwell separation  $d$  assuming  $\phi_{e/o} = \mp\pi/4$  (black lines) and  $\phi_{e/o} = \mp\pi/3$  (dashed blue lines). (b) Corresponding tunneling rate between the two potential wells in dependence to  $d$  owing to the energy difference of even and odd solutions.

We conclude, since the short-range phases depend on the relative spin orientations of the atom and ion, that we can control the tunneling dynamics of the atom with the spin of the ion [31, 65].

In figure 3.2 there is also a molecular state. As we will see, the energy curves exhibit avoided crossings as soon as resonances between molecular and vibrational states appear [65].

### 3.4 Moving ion in one dimension

The goal of the present chapter is to see how the MM of the trapped ion system may change the dynamics described above. For this purpose, it is convenient to

first briefly consider the case in which the atom is allowed to move in a static trap. We will use the solutions of this problem to construct the solutions for the MM case in section 3.5. Here, we follow Ref. [62] and additionally solve the dynamics for a system consisting of a  ${}^6\text{Li}$  atom and a  ${}^{171}\text{Yb}^+$  ion.

With a non-static ion the Hamiltonian of the system is given by

$$H = \underbrace{\frac{p_i^2}{2m_i} + \frac{1}{2}m_i\omega_i^2 z_i^2}_{H_i} + \underbrace{\frac{p_a^2}{2m_a} + V_{\text{DW}}(z_a)}_{H_a} - \underbrace{\frac{C_4}{(z_i - z_a)^4}}_{H_{ia}}. \quad (3.17)$$

Here,  $p_i$ ,  $m_i$  and  $z_i$  denote the momentum, mass and position of the ion, respectively and  $\omega_i$  is the trap frequency of the ion. The first term in equation (3.17) is the effective Hamiltonian of an ion in the harmonic potential of a Paul trap (see chapter 2.3.1) without MM, so that we can neglect the third term of equation (2.21). The second term is equal to equation (3.2) which we already know from section 3.2. The third term in equation (3.17) is again the atom-ion interaction term from chapter 2.2, now depending on the relative coordinate  $r = (z_i - z_a)$ .

Hence, we may rewrite the Hamiltonian in relative and center of mass (COM) coordinates, using:

$$M = m_i + m_a \quad (\text{total mass}) \quad (3.18)$$

$$\mu = (m_i m_a)/M \quad (\text{reduced mass}) \quad (3.19)$$

$$R = (m_i z_i + m_a z_a)/M \quad (\text{COM coordinate}) \quad (3.20)$$

$$r = z_i - z_a \quad (\text{relative coordinate}) \quad (3.21)$$

$$\omega_R^2 = (m_i\omega_i^2 + m_a\omega_a^2)/M \quad (3.22)$$

$$\omega_r^2 = (m_i\omega_i^2 + m_a\omega_a^2)/M \quad (3.23)$$

The Hamiltonian in terms of these coordinates is

$$H^{(d)} = H_R^{(0)} + H_r^{(0)} + H^{(1)}, \quad (3.24)$$

with

$$H_R^{(0)} = -\frac{\hbar^2}{2M} \frac{\partial^2}{\partial R^2} + \frac{1}{2} M \omega_R^2 R^2, \quad (3.25)$$

$$H_r^{(0)} = -\frac{\hbar^2}{2\mu} \frac{\partial^2}{\partial r^2} + \frac{1}{2} \mu \omega_r^2 r^2 - \frac{C_4}{r^4}, \quad (3.26)$$

$$H^{(1)} = \mu(\omega_i^2 - \omega_a^2) Rr + V_{\text{DW}}(R, r) - \frac{\mu\omega_a^2}{2} \left( \frac{m_a}{\mu} R^2 + \frac{\mu}{m_a} r^2 - 2Rr \right). \quad (3.27)$$

Equation (3.25) denotes the Hamiltonian of a harmonic oscillator with mass  $M$  and trap frequency  $\omega_R$ . Therefore, it has the eigenstates  $f_n(R)$ , which are Fock states with corresponding energies  $E_n^{(0)} = \hbar\omega_R(n + 1/2)$ , with  $n = a^\dagger a$  the particle number.

The dynamics of the system are described by  $H_r^{(0)}$ , the Hamiltonian of the relative motion, which is similar to the Hamiltonian  $H_A^{(0)}$  in equation (3.5). As in the static ion case we can solve the Schrödinger equation of such a Hamiltonian with QDT and find the eigenfunctions  $\Phi_k^{(0)}(r)$  and eigenenergies  $\mathcal{E}_k^{(0)}$ . The first term in equation (3.27) describes the effect of a mismatch between the ion's and atom's trap frequencies and the second term is the potential of the double-well in COM and relative coordinates. In order to find a set of discrete basis states, we used the same trick as for the static case, by adding and subtracting the term  $m_a\omega_a^2 z_a^2/2$  to equation (3.17). The third term in equation (3.27) is the subtracted part in COM and relative coordinates.

In order to transform the Schrödinger equation for the full Hamiltonian (3.24) into a matrix equation, we write the Hamiltonians (3.25)–(3.27) in terms of  $E^*$

and  $R^*$ :

$$H_R^{(0)} = -\frac{\mu}{M} \frac{\partial^2}{\partial R^2} + \frac{M}{\mu} B^2 \alpha R^2, \quad (3.28)$$

$$H_r^{(0)} = -\frac{\partial^2}{\partial r^2} + \alpha r^2 - \frac{1}{r^4}, \quad (3.29)$$

$$\begin{aligned} H^{(1)} = & \frac{\alpha}{\beta^2} \left( 2\gamma^2 R \otimes M^{(1)} - \frac{m_a}{\mu} R^2 - \frac{\mu}{m_a} M^{(2)} \right) \\ & + \frac{\alpha m_a}{\mu \beta^2} \left( \frac{d^2}{4} - \frac{1}{2} R^2 + \frac{1}{4d^2} R^4 \right. \\ & \quad + \frac{m_i}{M} R \otimes M^{(1)} - \frac{m_i}{Md^2} R^3 \otimes M^{(1)} \\ & \quad - \frac{m_i^2}{2M^2} M^{(2)} + \frac{3m_i^2}{2M^2 d^2} R^2 \otimes M^{(2)} \\ & \quad \left. - \frac{m_i^3}{M^3 d^2} R \otimes M^{(3)} + \frac{m_i^4}{4M^4 d^2} M^{(4)} \right), \quad (3.30) \end{aligned}$$

with

$$\begin{aligned} \gamma &= \frac{\omega_i}{\omega_a}, \quad \beta^2 = (m_i + \gamma^2 m_a)/M, \\ \alpha &= \left( \frac{\mu \omega_r}{\hbar} \right)^2, \quad B^2 = \omega_R^2 / \omega_r^2 = (m_a + \gamma^2 m_i) / (m_i + \gamma^2 m_a) \end{aligned}$$

and with matrix elements

$$M_{kk'}^{(j)} = \int (\Phi_{k'}^{(0)})^*(r) r^j \Phi_k^{(0)}(r) dr. \quad (3.31)$$

Here, the first term in equation (3.30) results from the first and last term in equation (3.27), while the double-well potential  $V_{\text{DW}}$  in the new coordinates and parameters is given by the second term in equation (3.30).

The full Hamiltonian can be diagonalized in the expanded basis  $|f_n(R), \Phi_k^{(0)}(r)\rangle$ , where  $f_n(R)$  denotes the Fock state with quantum number  $n$  of the COM motion, and  $\Phi_k^{(0)}(r)$  denotes the scattering wave function in the relative motion with quantum number  $k$ . As comparison with the static ion case we diagonalize for the same example system of one  $^{87}\text{Rb}$  atom and one  $^{171}\text{Yb}^+$  ion, assuming  $\phi_{e/o} = \mp\pi/4$ ,  $\omega_a = 2\pi \times 1.8\text{kHz}$  and  $\omega_i = 2\pi \times 9.9\text{kHz}$ . The corresponding correlation diagram is shown in figure 3.3 a). It was obtained

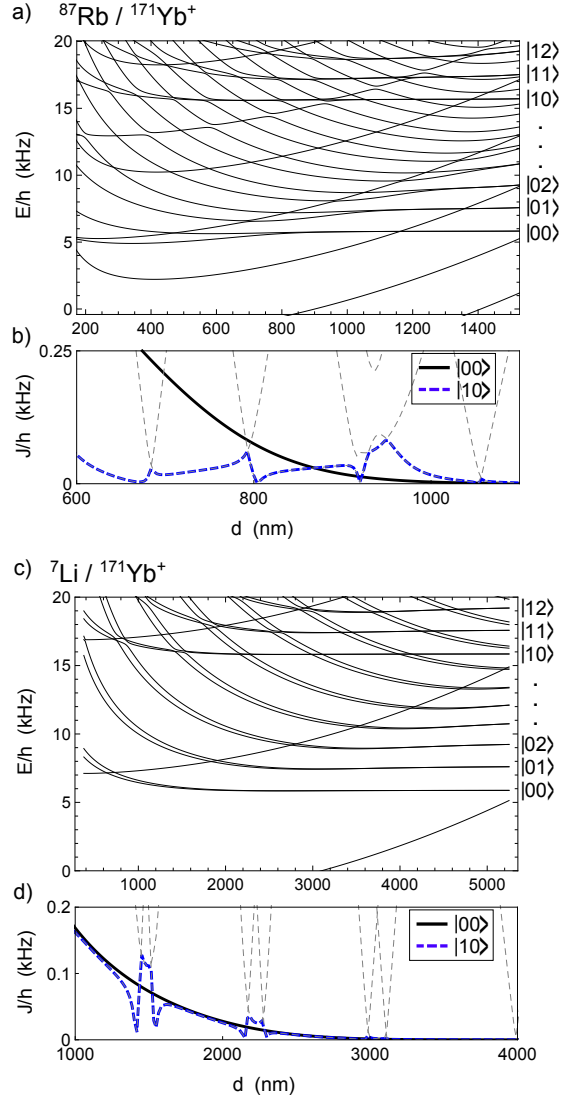


**Figure 3.3:** Correlation diagrams and corresponding tunneling rates as a function of the interwell separation  $d$  for a double-well system with a moving ion for a  $^{87}\text{Rb}$  atom and  $^{171}\text{Yb}^+$  ion (a)–(b) and for a  $^7\text{Li}$  atom and  $^{171}\text{Yb}^+$  ion (c)–(d) (see text).

by expanding the solutions onto 6417 basis states (69 in the COM and 93 in the relative coordinate). The particular ion-atom Fock states are marked with  $|n_i, n_a\rangle$ . Compared to the static ion correlation diagram in figure 3.2 a), we see that, due to the additional ion dynamics, the level density for both, vibrational and molecular states, is increased. Crossings between such states manifest themselves as resonances and cause avoided crossings in the adiabatic spectrum.

In figure 3.3 b) the corresponding tunneling rate  $J/h$  is plotted against interwell separation  $d$ . Here, we compare it for the ion and atom in their harmonic oscillator ground states  $|0, 0\rangle$  with the rate obtained for  $|1, 0\rangle$ . Now the tunneling depends on both, the spin state of the ion as well as its motional state. The tunneling rates for  $|0, 0\rangle$  and  $|1, 0\rangle$  differ for most values of  $d$ . For instance, the tunneling rate for  $|0, 0\rangle$  at  $d = 775$  nm is  $J/h = 101$  Hz and  $J/h = 37$  Hz for  $|1, 0\rangle$ . We conclude, that the atomic tunneling rate can be tuned via the motional state of the ion. Further details and explanations on these results and the influence of avoided crossings on those can be found in [62, 82].

Additionally and expanding on [62], we compare these results to those with a  ${}^7\text{Li}$  atom and a  ${}^{171}\text{Yb}^+$  ion which is the atom-ion combination of choice for the experiment presented in this thesis. For a direct comparison with Rb–Yb $^+$  we assume the same parameters:  $\phi_{e/o} = \mp\pi/4$ ,  $\omega_a = 2\pi \times 1.8$  kHz and  $\omega_i = 2\pi \times 9.9$  kHz. The corresponding correlation diagram and tunneling rates are presented in figure 3.3 c) and d), respectively. Here, 2700 states were taken into account and we note the different length scales for  $d$ .

We see that for Li–Yb $^+$  there are less molecular states and therefore less avoided crossings as for Rb–Yb $^+$ . Also the splitting of the degenerate symmetric and antisymmetric states happens at larger interwell separations  $d$ , since the wave packet size, which is proportional to  $m_a^{-1/2}$ , is larger for lower masses. Due to the larger ion-atom mass ratio, the dynamics of the Li atom and the Yb $^+$  ion are more independent than for Rb–Yb $^+$  in a similar fashion as in the Born-Oppenheimer approximation. This leads to a weaker coupling of the motional and molecular states resulting in smaller avoided crossings in the adiabatic spectrum. Therefore, the tunneling rate for Li–Yb $^+$ , shows less dependence on the motional state of the ion as long as there are no avoided crossings nearby.

### 3.5 Micromotion

By including the intrinsic micromotion (MM) of a Paul trap (see chapter 2.3.1), we turn our attention to a more realistic case, which was not considered in [62].

### 3.5.1 Radial micromotion

The time-dependent Hamiltonian of an ion trapped in a Paul trap in one dimension is given by (see chapter 2.3.1)

$$H_i(t) = \frac{p_i^2}{2m_i} + \frac{1}{8}m_i\Omega^2 z_i^2 [a + 2q \cos(\Omega t)]. \quad (3.32)$$

Here, the ion's motion consists of a harmonic oscillation at secular frequency  $\omega_i$  and the MM, driven by the radial, rf trap drive frequency  $\Omega$ . The relation between  $\omega_i$  and  $\Omega$  is given by

$$\omega_i \approx \frac{\Omega}{2} \sqrt{a + \frac{q^2}{2}}. \quad (3.33)$$

Here, we will investigate, how including the MM contributes to the dynamics of the ion-controlled double-well system. In order to do so, we exchange the time-independent  $H_i$ -term in equation (3.17) by the time-dependent version of equation (2.21) so that the full Hamiltonian of the system reads

$$H(t) = \frac{p_i^2}{2m_i} + \frac{1}{8}m_i\Omega^2 z_i^2 [a + 2q \cos(\Omega t)] + \frac{p_a^2}{2m_a} + V_{\text{DW}}(z_a) - \frac{C_4}{(z_i - z_a)^4}. \quad (3.34)$$

Following Ref. [49], where the MM in an atom-ion system with the atom trapped in a harmonic potential was analysed, we will derive the effective Hamiltonian  $H_{\text{eff}}(t)$  composed of a time-dependent and a time-independent term.

We start with deriving the solution of the Schrödinger equation for the Hamiltonian (2.21), while ignoring its time-independent terms [101]. In this case the Schrödinger equation takes the form

$$i\hbar \frac{\partial}{\partial t} \Psi(z_i, t) = \left( \frac{1}{4}m_i q \Omega^2 z_i^2 \cos(\Omega t) \right) \Psi(z_i, t), \quad (3.35)$$

with the solutions

$$\Psi(z_i, t) = \Psi(z_i, 0) \exp \left( -\frac{i}{4\hbar} m_i q \Omega z_i^2 \sin(\Omega t) \right). \quad (3.36)$$

The effect of the time-dependent potential term can be seen as an additional oscillating phase, the Cook-Shankland phase [101], to the time-independent wave

function  $\Psi(z_i, 0)$ . Therefore, it is convenient to write the wave function in the Schrödinger equation of the Hamiltonian (2.21)

$$i\hbar \frac{\partial}{\partial t} \Psi(z_i, t) = H_i(t) \Psi(z_i, t) \quad (3.37)$$

as

$$\Psi(z_i, t) = \exp\left(-\frac{i}{4\hbar} m_i q \Omega z_i^2 \sin(\Omega t)\right) \phi(z_i, t), \quad (3.38)$$

with the assumption, that the time-dependent part of  $\phi(z_i, t)$  is a slowly varying function and does not contribute to the Cook-Shankland phase [101].

The substitution of the solution (3.38) into the time-dependent Schrödinger equation (3.37) gives:

$$i\hbar \frac{\partial}{\partial t} \phi(z_i, t) = \left[ -\frac{\hbar^2}{2m_i} \frac{\partial^2}{\partial z_i^2} + \frac{1}{8} a m_i \Omega^2 z_i^2 + \frac{1}{8} m_i q^2 \Omega^2 z_i^2 \sin^2(\Omega t) + \frac{i}{4} q \Omega \hbar \left(1 + 2z_i \frac{\partial}{\partial z_i}\right) \sin(\Omega t) \right] \phi(z_i, t) \quad (3.39)$$

With equation (2.19) and  $g = (2 + 4a/q^2)^{-1/2}$  we can extract the effective Hamiltonian for the ion associated with the wave function  $\phi(z_i, t)$ , which reads

$$H_{i,\text{eff}}(t) = \frac{p_i^2}{2m_i} + \frac{1}{2} m_i \omega_i^2 z_i^2 + H_{\text{MM}}(t), \quad (3.40)$$

with

$$H_{\text{MM}}(t) = -m_i g^2 \omega_i^2 z_i^2 \cos(2\Omega t) - g \omega_i \{z_i, p_i\} \sin(\Omega t), \quad (3.41)$$

where  $\{z_i, p_i\}$  is the anticommutator of the ion's position and momentum operators. We denote  $H_{\text{MM}}(t)$  the time-dependent term of equation (3.40) as it describes the additional MM, while the time-independent terms account for the secular motion of the ion in a harmonic potential.

Accordingly, the total Hamiltonian of the system (3.1) can be written in the form

$$H(t) = H^{(d)} + H_{\text{MM}}(t), \quad (3.42)$$

while  $H^{(d)}$  is the Hamiltonian for the double well system without MM which was defined in equations (3.24 – 3.27).

As  $H^{(d)}$  is given in COM and relative coordinates, we also rewrite the MM term  $H_{\text{MM}}(t)$  in terms of these coordinates:

$$H_{\text{MM}}(t) = -m_i g^2 \omega_i^2 \left( \frac{\mu^2}{m_i^2} r^2 + 2 \frac{\mu}{m_i} r R + R^2 \right) \cos(2\Omega t) - g\omega_i \left( \{R, p\} + \frac{\mu}{m_i} \{r, p\} + \frac{\mu}{m_a} \{R, P\} + \frac{\mu}{M} \{r, P\} \right) \sin(\Omega t) \quad (3.43)$$

Here, the COM and relative momenta are denoted by  $P$  and  $p$ , respectively.

Following the argument in Ref. [49], we will not treat the MM as a perturbation of the system, since it is an intrinsic property of a Paul trap which cannot be switched off nor be compensated [76]. Instead, we note that  $H_{\text{MM}}(t)$  satisfies the periodicity condition  $H_{\text{MM}}(T+t) = H_{\text{MM}}(t)$ , with  $T = 2\pi/\Omega$ , and we can transform this periodic system into a linear system by employing Floquet theory.

In general, the special class of Floquet solutions  $\Psi(t)$  in the Schrödinger equation

$$i\hbar \frac{\partial}{\partial t} \Psi(t) = H(t) \Psi(t), \quad (3.44)$$

can be expressed as

$$\Psi(t) = e^{-\frac{i}{\hbar} \epsilon t} u(t), \quad (3.45)$$

with quasienergy  $\epsilon$  and the Floquet wave function  $u(t)$ , which is periodic in time. By substituting (3.45) into (3.44) we find, that we have to diagonalize the Floquet Hamiltonian

$$H_{\text{F}} = H^{(d)} + H_{\text{MM}}(t) - i\hbar \frac{\partial}{\partial t}. \quad (3.46)$$

To obtain the Floquet states and quasienergy for our system, we use the eigenenergies  $E_l$  and eigenstates  $|\Psi_l^{(d)}(R, r)\rangle$  of  $H^{(d)}$ , the double-well Hamiltonian without MM. For the corresponding Floquet Hamiltonian  $H_{\text{F}} - H_{\text{MM}}(t)$  those yield the Floquet eigenstates  $|u_{jl}\rangle = e^{ij\Omega t} |\Psi_l^{(d)}(R, r)\rangle$  with Floquet energies  $\epsilon_{jl} = E_l + j\hbar\Omega$ . Here, the integer  $j$  denotes the class of Floquet states and  $l$  denotes the quantum number of the solution without MM.

For the full Floquet Hamiltonian we introduce the generalized matrix elements of the extended Hilbert space

$$\langle\langle u_{j'l'}^* | H_{\text{F}} | u_{jl} \rangle\rangle = (E_l + j\hbar\Omega) \delta_{jj'} \delta_{ll'} + \frac{1}{T} \int_0^T dt \langle u_{j'l'}^* | H_{\text{MM}}(t) | u_{jl} \rangle. \quad (3.47)$$

By inserting  $H_{\text{MM}}(t)$  and the Floquet eigenstates  $|u_{jl}\rangle$  into the matrixelement of the second term we get:

$$\begin{aligned} \langle u_{j'l'}^* | H_{\text{MM}}(t) | u_{jl} \rangle &= \langle \Psi_{l'}^{(d)}(R, r) | e^{-ij'\Omega t} H_{\text{MM}}(t) e^{ij\Omega t} | \Psi_l^{(d)}(R, r) \rangle \\ &= \langle \Psi_{l'}^{(d)}(R, r) | [V_1 \cos(2\Omega t) + V_2 \sin(\Omega t)] e^{i(j-j')\Omega t} | \Psi_l^{(d)}(R, r) \rangle \end{aligned} \quad (3.48)$$

Following again Ref. [49], it can be shown that

$$\langle \Psi_{l'}^{(d)}(R, r) | V_2 | \Psi_l^{(d)}(R, r) \rangle = \frac{E_l - E_{l'}}{ig\hbar\omega_i} \langle \Psi_{l'}^{(d)}(R, r) | V_1 | \Psi_l^{(d)}(R, r) \rangle, \quad (3.49)$$

so that we have to evaluate the matrix elements for  $V_1$  and  $V_2$ , with

$$V_1 = -m_i g^2 \omega_i^2 \left( \frac{\mu^2}{m_i^2} r^2 + 2 \frac{\mu}{m_i} r R + R^2 \right), \quad (3.50)$$

and

$$V_2 = \frac{im_i g \omega_i}{\hbar} (E_l - E_{l'}) \left( \frac{\mu^2}{m_i^2} r^2 + 2 \frac{\mu}{m_i} r R + R^2 \right). \quad (3.51)$$

In a similar manner as in the static ion case, we expect the atom-ion interaction to be weak at large distances. Therefore, the corresponding matrix elements are small. As a consequence, the secular approximation for the trapped ion holds quite well, such that we can expect the particular states to resemble those of a harmonic oscillator. Here, resonances between motional and molecular states cause avoided crossings with very small gaps.

As the distance is reduced the atom-ion interaction gets stronger, resulting in increasing matrix elements. The larger these matrix elements are, the less we expect the secular approximation to hold. Consequently, the shape of the correlation diagram changes completely and exhibits avoided crossings with large gaps.

Regarding the selection rules for possible resonances, we see that the coupling between two states of different Floquet classes may become resonant, when  $\epsilon_{j'l'} = \epsilon_{jl}$ . With the selection rules  $|j - j'| = 2$  for  $V_1$  and  $|j - j'| = 1$  for  $V_2$ . Without further calculations we can already conclude from the relation in equation (3.49) that for sufficiently high  $E_l$  the coupling strength for  $V_2$  is much larger than for  $V_1$ . Thus the main effects of the MM on the system should originate from  $V_2$  [49, 82].

We will expand the solutions of the problem onto the set of eigenstates of the time-independent problem over a number of Floquet classes. But since we

cannot treat the MM as a perturbation, we have to take into account a large number of those classes.

To illustrate MM-induced coupling for our states of interest  $|\Phi_{g,e}^{(d)}\rangle$ , we have to calculate the corresponding matrix elements. Here, we will only evaluate the coupling to the ground state  $|\Phi_g^{(d)}\rangle$ , since it can be shown that for the coupling to excited states  $|\Phi_e^{(d)}\rangle$  we can expect similar results.

As mentioned above the pre-factor  $(E_l - E_{l'})$  in equation (3.49) makes  $V_2$  the main MM term and for a qualitative understanding of the new dynamics it is sufficient to just focus on it. To this effect we introduce the following notation for the absolute value of the matrix elements

$$V_{rr} = \frac{m_i g \omega_i}{\hbar} (E_g - E_l) \frac{\mu^2}{m_i^2} \left| \langle \Phi_g^{(d)} | r^2 | \Psi_l^{(d)} \rangle \right|, \quad (3.52)$$

$$V_{rR} = \frac{m_i g \omega_i}{\hbar} (E_g - E_l) \frac{\mu}{m_i} \left| \langle \Phi_g^{(d)} | r R | \Psi_l^{(d)} \rangle \right|, \quad (3.53)$$

$$V_{RR} = \frac{m_i g \omega_i}{\hbar} (E_g - E_l) \left| \langle \Phi_g^{(d)} | R^2 | \Psi_l^{(d)} \rangle \right|. \quad (3.54)$$

The resulting matrix elements are shown for  $^{87}\text{Rb}-^{171}\text{Yb}^+$  in figures 3.4 a)–3.4 c) and for  $^7\text{Li}-^{171}\text{Yb}^+$  in figures 3.4 d)–3.4 f). As for the case without MM we assume for both systems  $\phi_{e/o} = \mp\pi/4$ ,  $\omega_a = 2\pi \times 1.8\text{ kHz}$  and  $\omega_i = 2\pi \times 9.9\text{ kHz}$ . Here, the matrix elements are plotted against the detuning of the coupling state  $E_g - E_l$  for two different double-well separations  $d$ , respectively. In analogy to Ref. [49], we see that the couplings are strongest to states that are nearby in energy.

We first take a closer look at the different matrix elements of the  $^{87}\text{Rb}-^{171}\text{Yb}^+$  system. For increasing energy separations  $E_g - E_l$ , the couplings to  $V_{RR}$  quickly fall to zero. However, for  $V_{rR}$  and  $V_{rr}$  we see significant couplings with states that are far separated in energy. This behavior can be explained via the non-linear interaction between the atom and ion.

As we know already from the case without MM in chapter 3.4, the terms of the Hamiltonian in COM coordinate  $R$  describe a harmonic oscillator. Therefore, its eigenstates are Fock states and the corresponding matrix elements have well-defined selection rules:

$$\begin{aligned} \langle f_{n'} | R | f_n \rangle &\neq 0 & \text{for} & \quad |n - n'| = 1 \\ \langle f_{n'} | R^2 | f_n \rangle &\neq 0 & \text{for} & \quad |n - n'| = \{0, 2\} \end{aligned}$$

In figure 3.3 we saw that the ion's and atom's ground states experience only slight perturbations due to the atom-ion interaction. We conclude, that only

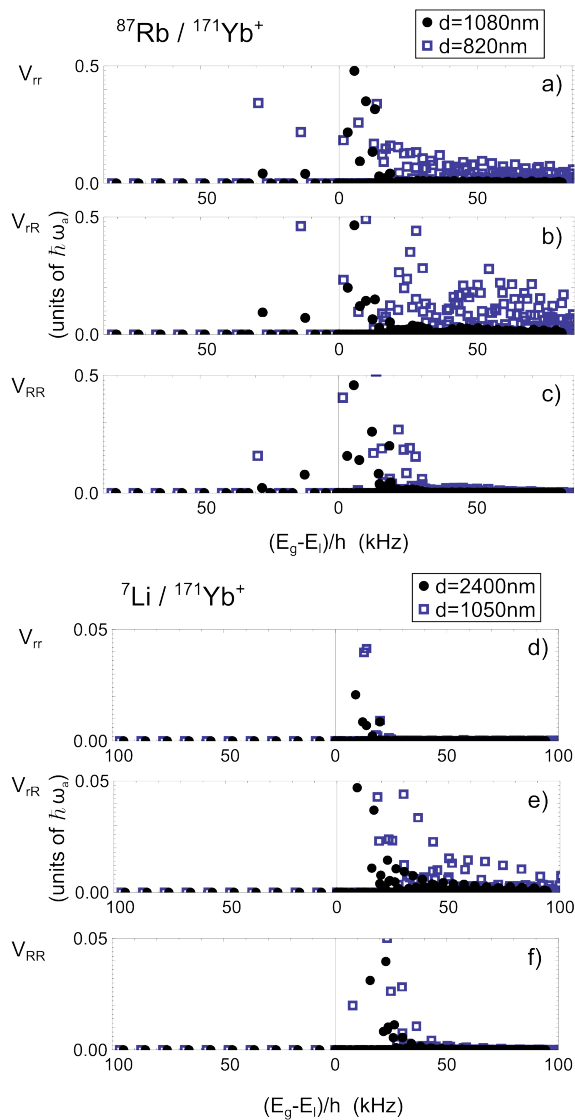


**Figure 3.4:** Matrix elements  $V_{rr}$ ,  $V_{rR}$  and  $V_{RR}$  in units of  $\hbar\omega_a$  with  $\phi_{e/o} = \mp\pi/4$ ,  $\omega_a = 2\pi \times 1.8\text{kHz}$  and  $\omega_i = 2\pi \times 9.9\text{kHz}$  (see text). (a)–(c) For  $^{87}\text{Rb}$ – $^{171}\text{Yb}^+$  with  $d = 1080$  and  $820\text{nm}$ . (d)–(f) For  $^7\text{Li}$ – $^{171}\text{Yb}^+$  with  $d = 2400$  and  $1050\text{nm}$ .

a few Fock states are involved in the interaction and due to the selection rules only coupling to nearby states occurs. Since there are also selection rules on  $j$ , the coupling states need to be of a different Floquet class. These states are unlikely to become resonant, as  $\Omega \gg \omega_R$ .

This picture changes completely when we examine the atom-ion scattering states in the relative coordinate  $r$ . Here, owing to the non-linearity of the atom-ion interaction there are no selection rules. Thus, the ground state couples to highly excited states belonging to different Floquet classes.

MM-induced coupling occurs when the energy gap to an excited state is in the same range as the rf trap drive frequency. In a correlation diagram these couplings appear as level crossings between the eigenenergies of the Fock states  $E_n^{(0)}$  and  $E_n^{(0)} - \Omega$  or  $E_n^{(0)} - 2\Omega$  as illustrated in Ref. [49]. In our example system we have  $\Omega = 2\pi \times 70.5$  kHz. For the case plotted here with an interwell separation of 820 nm, the couplings to states that are  $\approx 70$  kHz separated in energy reach up to 10% of the atomic trapping frequency. Additionally, such large couplings cause significant deviations from the secular solution if resonances occur. Therefore, we expect a lot of energy level crossings and thus resonances causing avoided crossings with increasing strength as  $d$  is reduced. In an experiment, this poses a big problem, since it significantly impedes the adiabatic transfer without exciting the atom.

Now we compare these results to the results of the  ${}^7\text{Li}-{}^{171}\text{Yb}^+$  system (see figures 3.4 d) – 3.4 f)). We directly see that for  $V_r$  and  $V_{rR}$  the coupling to higher excited states is much weaker and the MM induced couplings are on a percent level of the atomic trapping frequency of  $\approx 20$  Hz. Mathematically, the weaker coupling results from the pre-factors of the matrix elements, which are  $\mu^2/m_i^2 = m_a^2/M^2$  and  $\mu/m_i = m_a/M$ , respectively. From this we conclude, that adverse MM effects may be reduced by choosing  $m_i \gg m_a$ . This observation is in line with the findings in Ref. [50] which are discussed in chapter 2.3.2.

Finally, we numerically solve the full double-well problem including MM. The required total Hilbert space dimensions scale as  $N_{\text{COM}} \times N_{\text{rel}} \times N_{\text{echos}}$ , that is the number of COM states to be taken into account times the number of relative states times the number of Floquet classes. Here, we only take the Floquet classes  $j = -2, \dots, 2$  into account. Still, evaluating the corresponding correlation diagram for  ${}^{87}\text{Rb}-{}^{171}\text{Yb}^+$  as in figure 3.3 a) but with the additional MM, requires a Hilbert space of dimension  $32\,000 \times 32\,000$  which is beyond our computing power.

For diagonalizing the Hamiltonian for  ${}^7\text{Li}-{}^{171}\text{Yb}^+$ , as in figure 3.3 c), 13 500 states are used to form a sufficient basis, which reduces the computation time

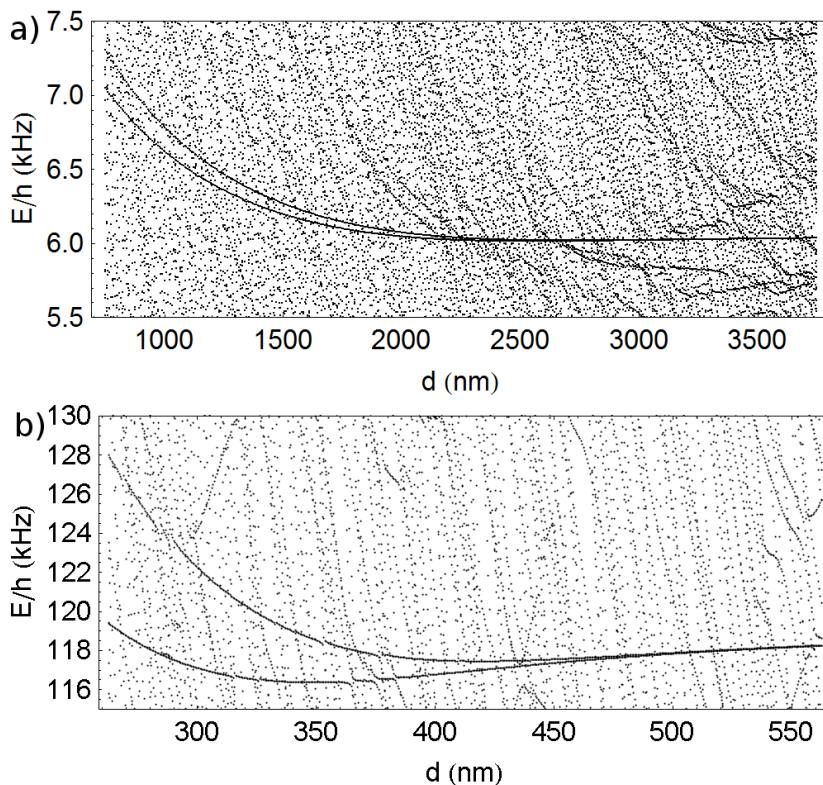


**Figure 3.5:** Correlation diagrams of quasi-eigenenergies for one  ${}^7\text{Li}$  atom and one  ${}^{171}\text{Yb}^+$  ion with radial MM. (a) Spectrum around the states  $|\Phi_{e,g}^{(d)}\rangle$  with  $\omega_a = 2\pi \times 1.8\text{ kHz}$ ,  $\Omega = 2\pi \times 70.5\text{ kHz}$  for  $q = 0.4$  and  $a = 0$  so that  $\omega_i \approx 2\pi \times 10\text{ kHz}$ . For the calculation we took  $j = -2, \dots, 2$ ,  $\phi_e = -\pi/4$ , and  $\phi_o = \pi/4$ . To construct the basis 13 500 states were used. The Hamiltonian was diagonalized for 500 different values of  $d$ . Here, many energy crossings appear but the avoided crossings remain very small. (b) Spectrum with  $\omega_a = 2\pi \times 98\text{ kHz}$ ,  $\Omega = 2\pi \times 967\text{ kHz}$  for  $q = 0.4$  and  $a = 0$  so that  $\omega_i \approx 2\pi \times 137\text{ kHz}$ . For the calculation we took  $j = -2, \dots, 2$ ,  $\phi_e = \pi/3$ , and  $\phi_o = -\pi/3$ . To construct the basis 8640 states were used. The Hamiltonian was diagonalized for 600 different values of  $d$ . It can be seen that many energy crossings appear and that the avoided crossings become bigger as  $d$  decreases.

significantly. The resulting correlation diagram is shown in figure 3.5 a). We can see that, even though many more energy levels are present in the spectrum, the coupling to the states  $|\Psi_{e,g}^{(d)}\rangle$  is very small, so that the MM should not pose a problem for the parameters considered here.

Additionally, we calculated the spectrum for  ${}^7\text{Li}-{}^{171}\text{Yb}^+$  around ground states for a higher trap drive frequency. To reduce the numerical complexity we put all energy scales to similar values, i.e.,  $\omega_a = 2\pi \times 98$  kHz and  $\Omega = 2\pi \times 967$  kHz for  $q = 0.4$  and  $a = 0$ , so that  $\omega_i \approx 2\pi \times 137$  kHz. Also here we find that at least for large inter-well separations  $d$  the MM induced couplings are weak resulting in relatively small avoided crossings. This enables us to apply the secular approximation for the double-well system and we expect, that taking more Floquet classes into account will not alter the results for the values of  $d$  plotted.

However, for smaller inter-well separations the ground state presents many avoided crossings and therefore more Floquet classes are required to reach convergence.

### 3.5.2 Axial micromotion

Besides the intrinsic radial MM of the ion, there might be imperfections in the setup causing MM along the axial direction of the Paul trap. Some of these, namely asymmetric trapping potentials or electric stray fields, will be discussed in chapter 5.6 and we call the motion, induced by those, excess MM. Additionally, a fraction of the intrinsic MM is projected onto the axial component of the ion in a Paul trap. This might be due to insufficient low-pass filtering of the end caps or when the ion is not axially positioned equidistant to both end caps.

In the axial direction, the trapping potential of a Paul trap, generated by the end caps, is a harmonic potential. Hence, the ion's time-dependent Hamiltonian with axial MM in one dimension is given by

$$H_i(t) = \frac{p_i^2}{2m_i} + \frac{1}{2}m_i\omega_i^2 z_i^2 - eE_{\text{MM,ax}}z_i \sin(\Omega t) , \quad (3.55)$$

where the first two terms describe the ion in a harmonic potential. The last term specifies the additional axial MM, with  $E_{\text{MM,ax}}$  the electric field amplitude of the oscillating axial field.

In order to study the effect of the oscillating term in equation 3.55 we first express it in relative and COM coordinates:

$$H_{\text{MM,ax}}(t) = eE_{\text{MM,ax}} \sin(\Omega t) \left( \frac{\mu}{m_i} \hat{r} + \hat{R} \right) \quad (3.56)$$

To examine the impact of axial MM, we compute the coupling strength of the ground state  $g$  to higher  $l$  states caused by the axial MM related operator  $\hat{V}_3$ . Here, we focus on the relative coordinate as this will cause the largest effect, as explained above. In particular we compute

$$V_r = \left| \frac{1}{2} \langle \Phi_g^{(d)} | \hat{V}_3 | \Psi_l^{(d)} \rangle \right| \quad \text{with} \quad (3.57)$$

$$\hat{V}_3 = eE_{\text{MM,ax}} \sin(\Omega t) \frac{\mu}{m_i} \hat{r} \quad . \quad (3.58)$$

In figure 3.6 the computed absolute matrix elements  $V_r$  are plotted against the detuning of the coupling state  $E_g - E_l$  for an oscillating electric field of  $E_{\text{MM,ax}} = 0.1 \text{ V/m}$ . As for the radial MM in figure 3.4, we assume for both systems  $\phi_{e/o} = \mp\pi/4$ ,  $\omega_a = 2\pi \times 1.8 \text{ kHz}$  and  $\omega_i = 2\pi \times 9.9 \text{ kHz}$ . For  ${}^7\text{Li}-{}^{171}\text{Yb}^+$  we note the two different scales for  $V_r$  and especially the much larger scales of these matrix elements compared to the ones plotted in figure 3.4.

For both atom-ion combinations the axial MM can cause major modifications to the double-well system because the coupling is of order  $\sim \hbar\omega_a$ . We conclude, that axial MM has to be compensated much better than  $E_{\text{MM,ax}} = 0.1 \text{ V/m}$ , which may be possible with state-of-the-art MM compensation [102].

## 3.6 Summary and Conclusions

In this chapter, the one dimensional dynamics of an ion-controlled atomic double-well system have been studied theoretically for the case, that the ion is trapped in a Paul trap. The main focus was on the analysis of the effect of MM on the system. We used the Floquet theorem to obtain the quasienergies and find that the MM causes many avoided crossings in the correlation spectrum when a resonance occurs between different quasienergy classes. The exact strength of these crossings depends on the trap parameters, but we conclude that it is a good idea to choose an ion-atom combination with a large mass ratio. In an experiment, we would tune  $d$  dynamically. Here, the avoided crossings will complicate state preparation as if  $d$  is reduced slowly, the trapped state is transformed from the vibrational to a highly excited state by passing the avoided crossing adiabatically. To conserve the initial state, the wells have to be brought together

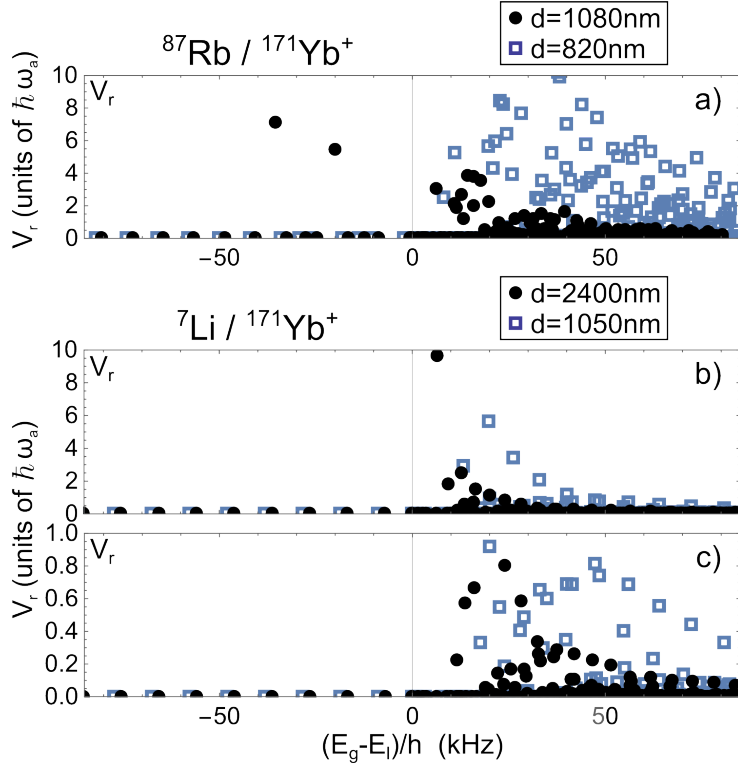


**Figure 3.6:** Matrix element  $V_r$  in units of  $\hbar\omega_a$  with  $E_{\text{MM},\text{ax}} = 0.1\text{ V/m}$ ,  $\phi_{e/o} = \mp\pi/4$ ,  $\omega_a = 2\pi \times 1.8\text{ kHz}$  and  $\omega_l = 2\pi \times 9.9\text{ kHz}$  (see text). (a) For  $^{87}\text{Rb}-^{171}\text{Yb}^+$  with  $d = 1080$  and  $820\text{ nm}$ . (b)–(c) For  $^7\text{Li}-^{171}\text{Yb}^+$  with  $d = 2400$  and  $1050\text{ nm}$ . Note the different scales for  $V_r$ .

adiabatically with respect to the crossings, but without exciting the atoms to higher trap states. Additionally, the two-mode approximation may break down in a many-body scenario when including the MM, complicating its theoretical description.

In linear Paul traps the rf field confines the ions only in the two radial directions. To improve the situation it may be advisable to have the double-well separation in the third, axial direction where the ion is confined by static fields. However, due to the spherical symmetry of the atom-ion interaction potential, there will be some minimum distance where the secular approximation will fail [49]. Additionally, there may be excess MM in the axial direction caused by imperfections in the experimental setup [76]. We have analyzed the effect of axial MM on the double-well system and found that possible couplings can be of order  $\sim \hbar\omega_a$  causing significant deviations from the secular approximation. For the parameters considered in this chapter, the oscillating electric fields in axial direction need to be reduced to  $\leq 0.1 \text{ V m}^{-1}$ , for instance, by employing state-of-the-art MM compensation [102], in order to avoid complications due to MM.



## 4 — Experimental setup

In this chapter the experimental setup for trapping, cooling and overlapping of neutral  ${}^6\text{Li}$  atoms and  $\text{Yb}^+$  ions is presented in detail. This includes the trap design, vacuum system, magnetic field coils, laser setup and imaging system.

## 4.1 Introduction

The main objective of my PhD research was to design, build and characterize an apparatus which is capable of realizing an atom-ion system as described in chapter 1. Such a hybrid trap, which combines state-of-the-art ion- and atom-trapping technologies in order to spatially overlap  $\text{Yb}^+$  ions with a gas of  $^6\text{Li}$  atoms, allows to investigate collision dynamics and to perform quantum simulation experiments. This chapter is structured as follows:

First, the requirements which the hybrid trap has to fulfill are stated in section 4.2. In section 4.3 we present the final experimental setup. In section 4.4 the ion trap, which is at the heart of the experiment is presented in detail. During the development process simulations have been carried out in order to numerically analyze the trap design which are presented in section 4.5. A helical resonator provides the ion trap with an amplified rf signal as described in section 4.6.

In section 4.7 we present the vacuum setup. Our single chamber solution results in a compact *two-story* design, which provides optimal optical access. Additionally, ultra-high vacuum (UHV) at the main chamber is maintained by separating the atom oven from it using differential pumping.

The coil setup used to dynamically generate magnetic fields is explained and characterized in section 4.8. Here, the focus is on two home-made coils in Helmholtz configuration which can generate fields of up to 1000 G while they can also be switched off or to anti-Helmholtz configuration within milliseconds.

For cooling, state-preparation, state-manipulation and state-detection of both species as well as for trapping  $^6\text{Li}$  numerous laser-beams at different frequency, intensity and polarization are employed. The level schemes of  $^6\text{Li}$  and  $^{171}\text{Yb}^+$  and a complete description of the laser setup including laser stabilization are given in section 4.9. In section 4.10 we discuss the optical access of the design before the setup for absorption imaging of the magneto optical trap (MOT) and the setup for fluorescence imaging of the ions is presented in section 4.11.

## 4.2 Design considerations

The experimental setup was designed with the following criteria in mind:

**trap lifetime:** The trap lifetime for both, atoms and ions, needs to be sufficiently long for the initialization-, interaction- and detection-process.

**initialization:** In order to study the quantum dynamics of interacting mixtures of  ${}^6\text{Li}$  atoms and  $\text{Yb}^+$  ions they need to be prepared in well-defined quantum states. Therefore, both need to be cooled to temperatures below the Doppler-limit and prepared in the internal state of choice with high accuracy before brought into interaction.

**controllability:** In order to ensure adequate and reproducible measurements the operations done on the atoms and ions need to be controlled precisely with accurate timing.

**detection:** At the beginning and at the end of each experimental cycle a read-out of the system is performed. With the setup it should be possible to measure the internal and external state as well as the number of atoms and ions, respectively.

The system of choice is a combination of two trapping technologies, namely a Paul trap for  $\text{Yb}^+$  ions merged with a crossed optical dipole trap for  ${}^6\text{Li}$  atoms. Both systems offer the best prerequisites for a hybrid system in terms of the criteria above. Paul traps allow for individual addressing and imaging of the ions as well as for the precise preparation of their internal and motional state. In optical dipole traps dense clouds of millions of atoms can be trapped and prepared in the same quantum state.

During the formation phase of the setup the following points were given consideration in order to keep the system as simple and as compact as possible while optimizing the experimental conditions.

A well-established trapping method for  ${}^6\text{Li}$  is to pre-cool the atoms in a Zeeman slower before trapping them in a MOT<sup>1</sup>. Subsequently, the atom cloud is to be transferred into a crossed optical dipole trap (ODT)<sup>2</sup>. This facilitates the excitation of Feshbach resonances to realize evaporative cooling of  ${}^6\text{Li}$  [105].

In our design, the MOT is generated outside the ion trap. This prevents the contamination of the ion trap electrodes with highly reactive  ${}^6\text{Li}$  and allows to trap large atom numbers. Instead of a standard MOT, a mirror MOT is utilized underneath the ion trap. A mirror MOT allows to realize a MOT close to surfaces which minimizes the distance from the MOT to the ions. Here, the Zeeman slower is positioned diagonally behind the mirror. This mitigates the contamination of the mirror with  ${}^6\text{Li}$ . The next step of the sequence is the

---

<sup>1</sup>Using a Zeeman slower is recommended, since for  ${}^6\text{Li}$  it is hard to obtain enough atoms from a temporarily raised background pressure [103].

<sup>2</sup>The experiments described in this thesis are performed on atoms in a magnetic trap. The ODT was implemented in later experiments and will be characterized in Ref. [104].

transfer of the atom cloud from the mirror MOT into the crossed ODT. As the latter is located at the ion position the atoms are trapped in a magnetic trap as an intermediate step. The position of the atoms in the magnetic trap, being the minimum of a magnetic quadrupole field, is transferred to the position of the ODT by dynamically tuning the current of the magnetic field coils. The crossed ODT is coupled in through apertures in the end caps of the Paul trap. Thus, the axes of the ODT and of the ion trap have the same orientation. The use of a massive Paul trap with a large thermal mass prevents possible damage by accidental absorption of the high power fiber laser beam. All components of the trap setup as well as the vacuum parts in the proximity of the trapping region are made from non-magnetic materials or from materials with a very low magnetic permeability ( $\mu_r \leq 1.1$ ). Thus, the apparatus is less sensitive to the influence of large magnetic fields as generated in the experiment. Re-entrant viewports, as well as a custom-made main vacuum chamber allow for optical access in multiple axes for laser beams as well as for imaging at the position of the MOT and at the position of the ions.

### 4.3 Final experimental setup

The design of the vacuum chamber is shown in figure 4.1. It is built up of three parts. At the heart of the experimental setup is an ion trap, where  ${}^6\text{Li}$  atoms and  $\text{Yb}^+$  ions are spatially overlapped and the experiments are conducted. Several coils provide the magnetic fields necessary.

On the left side, vacuum pumps and a gauge provide and measure UHV which is necessary to ensure sufficiently long lifetimes of the atoms and ions.

The oven-chamber on the right side is the source of  ${}^6\text{Li}$  atoms. In order to protect the main vacuum chamber from the elevated pressures in the atomic oven, it is separated by a differential pumping stage which is part of the Zeeman slower for pre-cooling the atoms.

### 4.4 Ion trap design

The design of the ion trap is presented in figure 4.2. This linear Paul trap is composed of four hyperbolically shaped blade electrodes for radial confinement and two end cap electrodes for axial confinement (see chapter 2.3.1). The blades have a distance to the trap center of  $r_0 = 1.5$  mm and a length of 9.0 mm, while the end caps are separated by  $2z_0 = 10.0$  mm.

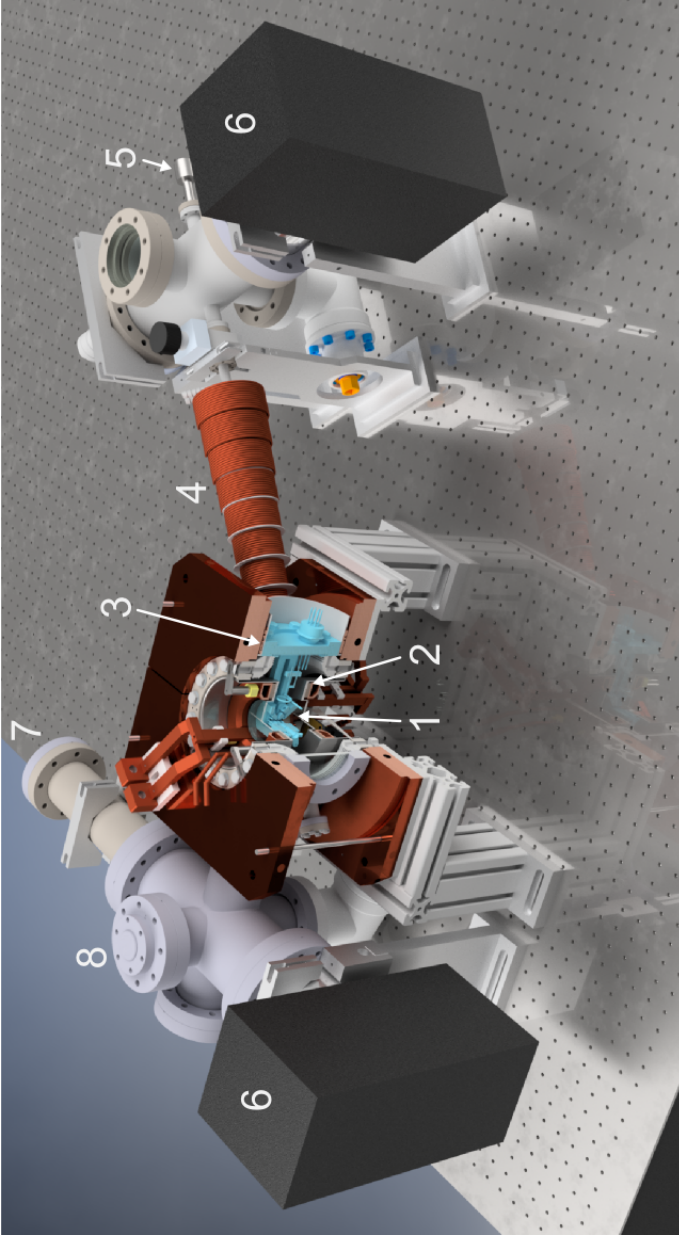


**Figure 4.1:** Sectional drawing of the experimental setup. An ion trap (1) is embedded into the main vacuum chamber at the center. Two pairs of field coils – (2) Feshbach coils and (3) MOT coils – provide homogeneous as well as gradient magnetic fields. In a Zeeman slower (4)  ${}^6\text{Li}$  atoms, emerging from the Li-oven (5), are pre-cooled. UHV is sustained and measured with ion pumps (6), a titanium sublimation pump (TSP) and an ion gauge (8). For more information see the corresponding sections.

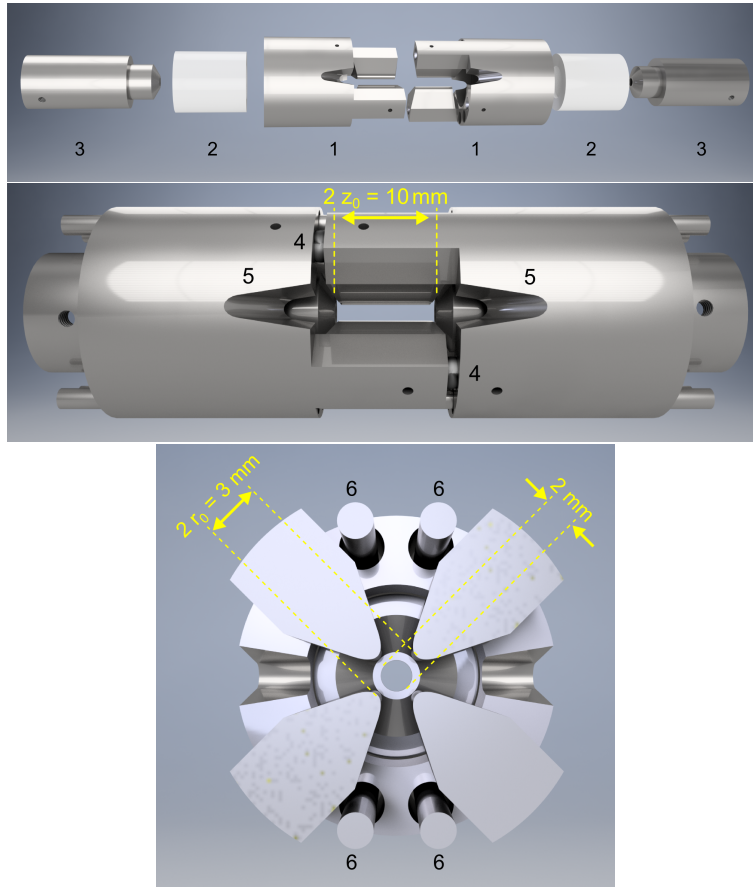


**Figure 4.2:** CAD drawings of ion trap: (top) Exploded assembly drawing. The end caps (3) are inserted into electrically insulating ceramic tubes (2) with a wall thickness of 1 mm which in turn fit exactly into an axial bore hole in the solid metal cylinders featuring the blade pairs (1); (middle) Side view of assembled trap. Spherical spacers (4) separate the metal cylinders by 1 mm, while a barrier at the inner end of the ceramic tubes provides a fixed horizontal distance between the end caps and blades of 0.5 mm. Notches (5) on the flanks of the metal cylinders allow for horizontal optical access under an incident angle of 45 deg. (bottom) Vertical cut through the center of the trap. The end caps feature an aperture with a diameter of 2 mm for laser access. To compensate the radial position of the ions four additional rod electrodes (6) with a diameter of 2 mm are implemented.

The whole trap-setup including the mount is designed to be built out of a single piece of stainless steel<sup>3</sup> to ensure highest precision in shaping of the surfaces and fitting (when assembled)<sup>4</sup>.

#### 4.4.1 Blade electrodes

Figure 4.3 shows one pair of blade electrodes. One of the main characteristics is, that each pair of electrodes has been carved out of one metal cylinder. This solid and firm design ensures optimal radial and axial alignment of the blades to each other. Additionally, since only one connection is needed to supply rf voltage to one blade pair, the risk of possible phase differences between the rf potentials is minimized (see chapter 5.6). Spherical, insulating spacers<sup>5</sup> sitting in small cavities separate the blades from the opposite blade-component by 1 mm and provide precise alignment in all three dimensions. The massive construction of the blades allows them to withstand short-time illuminations with high-power laser light as well as mechanical stress due to temperature fluctuations and during vacuum bake-out. Additionally, their hyperbolic shape provides an accurate quadrupole potential at the ion position.

#### 4.4.2 End cap electrodes

The end caps, as shown in figure 4.4, are rotationally symmetric w.r.t. the trap axis and at the axis of symmetry their tips possess an aperture with a diameter of 2 mm. As can be seen in the CAD drawing, the end caps are optimized for maximal optical access. They also provide laser access for the ions and are designed for realizing the crossed optical dipole trap which will be sent through the apertures as explained in chapter 4.10.

#### 4.4.3 Yb oven

The design of the Yb oven is shown in figure 4.5. It was adapted from Ref. [106]. A stainless steel rod is electrically connected to a stainless steel tube filled with chunks of crystalline ytterbium<sup>6</sup> via a metal sheet made of tantalum<sup>7</sup>. By applying current ( $I_{\text{Yb-oven}} \leq 3.5 \text{ A}$ ) Joule heating occurs at the thin tube walls

---

<sup>3</sup>EN steel number 1.4429,  $\mu_r < 1.1$

<sup>4</sup>The construction plan can be found in appendix C.

<sup>5</sup>Silicon nitride ( $\text{Si}_3\text{N}_4$ ),  $\varnothing = 3 \text{ mm}$ , grade 10

<sup>6</sup>Sigma-Aldrich, Ytterbium chunks, 99.9% Metals Basis, 548804-5G

<sup>7</sup>Ta, electrical resistivity: 131 n $\Omega$ m

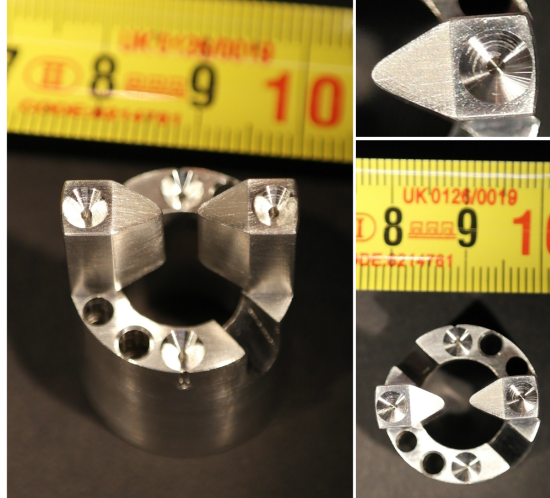


**Figure 4.3:** Pictures of ion trap component featuring one pair of blade electrodes. The zoom-in shows the hyperbolic shape of the blades and one of the four cavities for spherical spacers (see text).

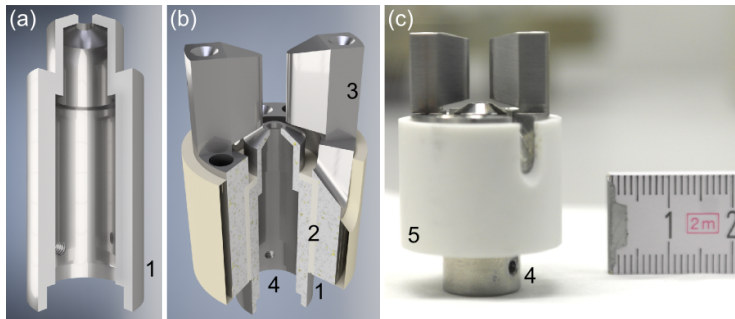


**Figure 4.4:** (a) Sectional drawing of an end cap (1). The diameter near the top of the electrode is reduced to accurately fit it into its carrier while on the inside the wider diameter at the bottom increases the optical aperture. (b) CAD drawing of an end cap stuck inside the cylinder featuring a blade pair (3) isolated from each other by a ceramic tube (2). The tip of the end cap sticks out just underneath the blades. At the tapped hole at the bottom (4) the voltage source is connected. (c) Picture of the assembly shown in (b). On the outside there is an additional ceramic tube (5) with a thickness of 1.5 mm which insulates the blade electrodes from the mount.

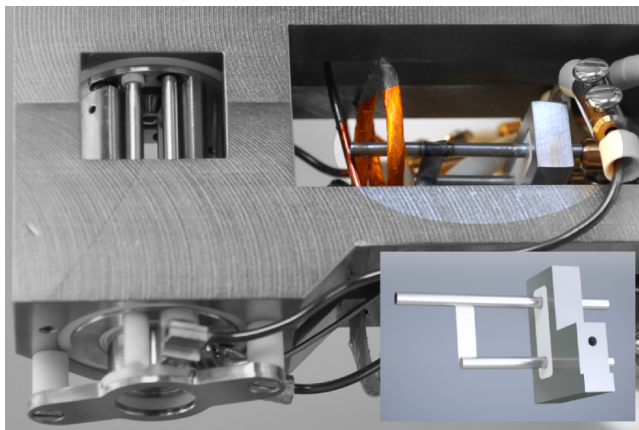


**Figure 4.5:** Ion trap assembly with Yb oven highlighted. The inset shows a CAD drawing of the Yb oven. While the lower rod is massive, the upper rod is a tube filled with chunks of crystalline Yb (diameter  $\approx 1 - 1.5$  mm). A flat metal sheet made of tantalum serves as electrical connection between both rods.

which leads to diffusion of gaseous Yb. The oven is run continuously since the background pressure is not notably affected by it<sup>8</sup>.

#### 4.4.4 Mount for ion trap and MOT mirror

Figure 4.6 shows the fully assembled hybrid trap setup, mounted on a custom-made CF63 feedthrough flange<sup>9</sup>. The mount<sup>10</sup> is designed to be as stable and as compact as possible to preserve a vibration-free environment and to ensure that the assembled trap fits through the flange of the vacuum chamber. The mirror<sup>11</sup> for the mirror MOT is attached at the bottom of the mount, right underneath

<sup>8</sup>Previous long-time observations showed that the heating rate and trapping behavior remain unaffected by a continuously running oven [107].

<sup>9</sup>Vacom, special feedthrough flange CF63, material: 1.4404, electrical feedthroughs: 1x W-HV2-10-CE-AM16 (10 Alumel® pins,  $U_{\max} = 2$  kV,  $I_{\max} = 4.8$  A), 1x W-HV6-4-CE-CU13 (4 copper pins,  $U_{\max} = 6$  kV,  $I_{\max} = 27$  A), specials: 4xM4x0.7 tapped blind holes

<sup>10</sup>Made from the same piece of stainless steel as the ion trap components.

<sup>11</sup>Altechna, HR laser line mirror, material: BK7, thickness: 0.9 mm, custom shape, coating: HR>99.6 % @ 671 nm, AOI=45°

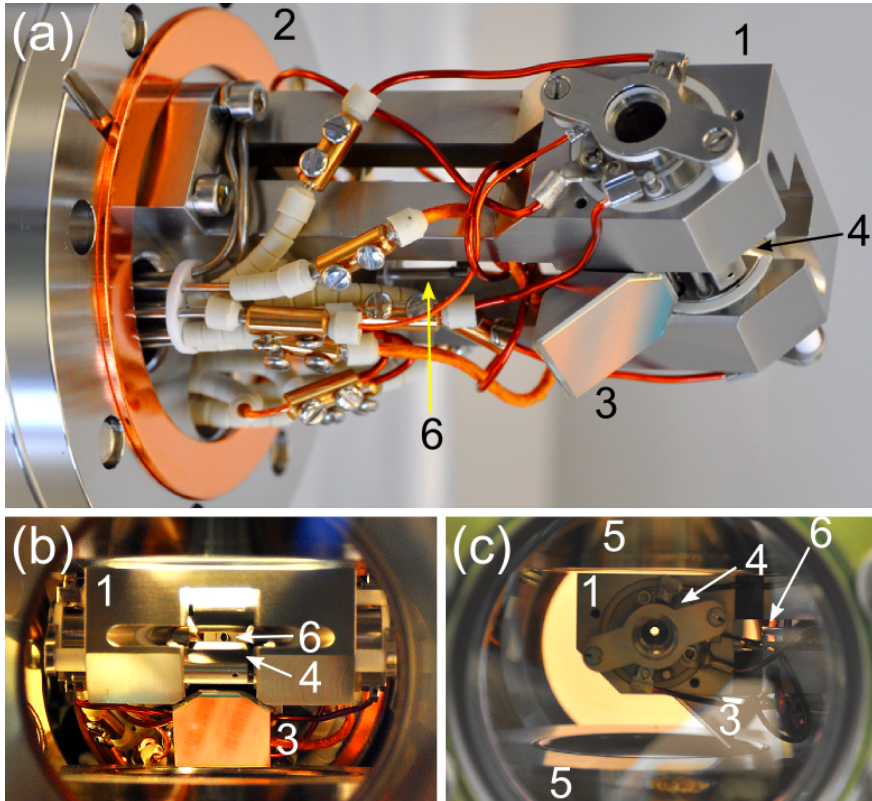


**Figure 4.6:** Fully assembled hybrid trap with mounted MOT mirror. (a) The mount of the hybrid trap setup (1) is attached to a custom-made feedthrough flange (2) which also provides all necessary electrical connections (see text). An in-vacuum mirror for the MOT (3) is attached at the bottom of the mount at an angle of  $45^\circ$ . The ion trap (4) fits exactly in a through bore hole in the mount; (b) and (c) Front and side view of the hybrid trap setup built-in the vacuum chamber. Above and underneath the hybrid trap inverted viewports (5) protrude into the vacuum chamber. The Yb-oven (6) is located behind the ion trap and points exactly to the center of the ion trap.

the ion trap. For wiring UHV compatible kapton wires<sup>1213</sup>, connectors<sup>14</sup> and isolators<sup>1516</sup> were used.

## 4.5 Ion trap simulation

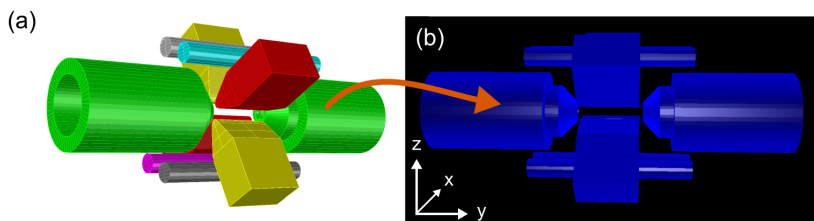


**Figure 4.7:** (a) AutoCAD drawing of trap electrodes. (b) Visualization of imported structures for simulation.

In order to properly design an ion trap, the electric potential  $\Phi$  inside the trap volume generated by the electrodes needs to be calculated accurately. With this knowledge, the trapping characteristics of the particular design can be simulated. A software package<sup>17</sup>, providing powerful numerical tools, allows to reproduce extensive electrode geometries and to calculate the resulting trapping potentials. In particular, the trajectories of ions can be simulated. The software is constructed such that an AutoCAD<sup>18</sup> drawing of the ion trap, as shown in figure 4.7, can be read into the program as a 3D surface model. To obtain the electric potential  $\Phi$ , the Laplace equation  $\Delta\Phi(x, y, z) = 0$  is solved with Dirichlet boundary conditions  $\Phi(x, y, z) = U_i$  on the surface of electrode  $i$ . Here, employing Boundary Element Method (BEM), where only the electrode surfaces need to be discretized instead of the whole field volume, significantly reduces

<sup>12</sup>Allectura, 311-KAPM-200, Multi Strand High Flexible Kapton Wire for UHV,  $I_{\max} = 20$  A,  $\varnothing 2.2$  mm

<sup>13</sup>Allectura, 311-KAP-130, Kapton insulated Cu-wire,  $\varnothing 1.3$  mm,  $U_{\max} = 10$  kV

<sup>14</sup>Allectura, diverse cable rings (360-RING-1.0-M2, 360-RING-1.7-M2), power push on connectors (360-PPO-1.5) and power inline connectors (360-PIC-1.5, 360-PIC-1.8)

<sup>15</sup>Allectura, 316-CBEAD-1.5, Ceramic beads, AD = 4 mm, ID = 1.5 mm

<sup>16</sup>Allectura, 316-CBEAD-2.5, Ceramic beads, AD = 5 mm, ID = 2.5 mm

<sup>17</sup>Download for both Linux and Windows operating systems freely available at kilian-singer.de/ent.

<sup>18</sup>www.autodesk.de

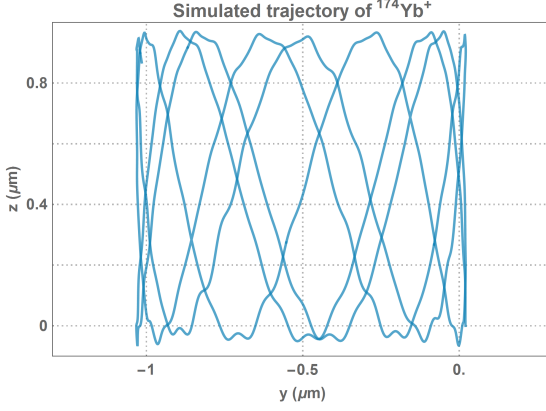


**Figure 4.8:** Simulated ion trajectory for  $^{174}\text{Yb}^+$  with  $\Delta t = 0.05$  ms,  $U_{\text{rf}} = 100$  V,  $U_{\text{dc}} = 20$  V and  $\Omega = 2\pi \times 2$  MHz

computing time [108]. A detailed mathematical description can be found in [6].

Figure 4.8 shows the simulated trajectory of an  $^{174}\text{Yb}^+$  ion for our ion trap design with the parameters given in the caption. From such simulations the trap frequencies of the ion in all axes can be extracted. The axial and radial trap frequencies  $\omega_{\text{ax/rad}}$  obtained for varying trap parameters  $U_{\text{rf}}$  and  $U_{\text{dc}}$  are shown in figure 4.9. Using equation 2.19 they are given by

$$\omega_{\text{ax}} = \sqrt{\frac{2QU_{\text{dc}}\kappa_{\text{ax}}}{m_{\text{ion}}y_0^2}} \quad \text{and} \quad (4.1)$$

$$\omega_{\text{rad}} = \frac{\Omega}{2m_{\text{ion}}} \sqrt{2Q \left( \frac{(\kappa'_{\text{rad}})^2 QU_{\text{rf}}^2}{(r_0^2 \Omega)^2} - \frac{2m_{\text{ion}} U_{\text{dc}} \kappa_{\text{rad}}}{y_0^2} \right)}, \quad (4.2)$$

with  $Q$  the electric charge of the ion with mass  $m_{\text{ion}}$ ,  $U_{\text{dc}}$  the applied voltage at the end caps,  $U_{\text{rf}}$  the amplitude of the rf voltage signal, the trap parameters  $r_0 = 1.5$  mm and  $y_0 = 5$  mm and geometrical factors  $\kappa_{\text{ax}} = \kappa_y$  and  $\kappa'_{\text{rad}} = \kappa'_x = \kappa'_z$  (see chapter 2.3.1). From the fits in figure 4.9 the geometrical factors can be identified with  $\kappa_{\text{ax}} \approx 0.115$ , thus  $\kappa_{\text{rad}} = 2\kappa_{\text{ax}} \approx 0.230$  and  $\kappa'_{\text{rad}} \approx 0.974$ .

The stability parameters  $a$  and  $q$  from equations 2.15 and 2.16 obtained from the simulation are plotted in figure 4.10.

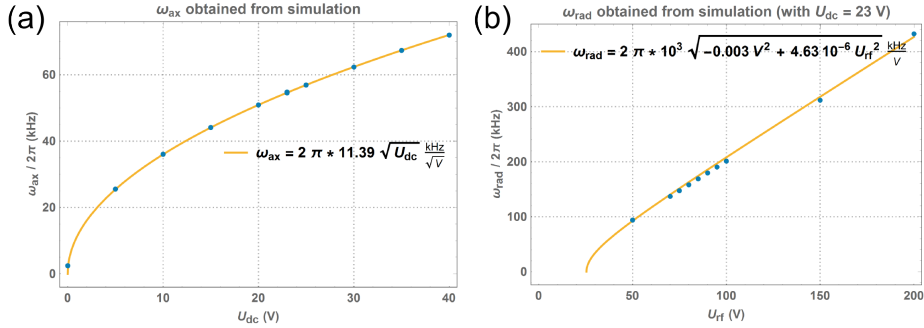


**Figure 4.9:** (a) Axial and (b) radial trap frequencies obtained from simulated trapping potentials for  $^{174}\text{Yb}^+$  with  $\Omega = 2$  MHz.

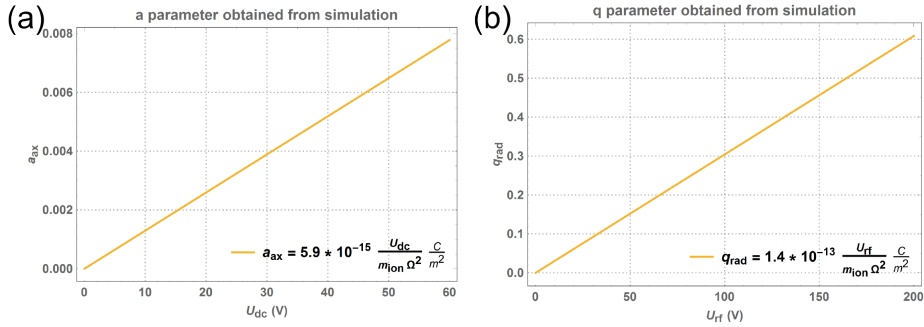


**Figure 4.10:** (a)  $a$  parameter and (b)  $q$  parameter for the final ion trap design obtained from simulation.

## 4.6 Helical resonator

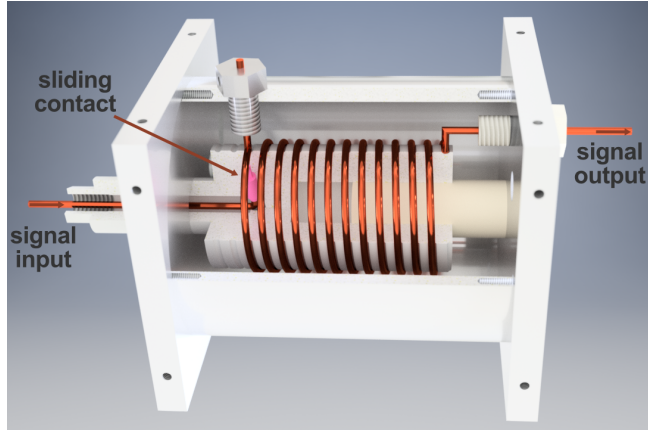


**Figure 4.11:** Sectional drawing of helical resonator. The sliding contact (highlighted in pink) is inserted in a Teflon cylinder which also serves to support a copper coil via helical grooves on the surface. By rotating the Teflon cylinder the position of the tap point is adjusted to perform impedance matching (see text).

One of the ion trap blade pairs is driven with an rf signal generated in a signal generator<sup>19</sup> and a 2 W amplifier<sup>20</sup>. For tight traps with deep trapping potentials the amplitude of the signal is up to several hundred Volts. Typically, the impedance of the rf source, with an output impedance of  $50\ \Omega$ , differs from the load impedance of the ion trap including the wiring and interconnections. Here, employing a helical resonator allows for impedance matching between the rf source and the ion trap to prevent reflections of the rf signal to the amplifier and to provide higher amplitudes. A helical resonator combined with an ion trap represent a series LCR circuit with resonance frequency  $\omega_0 = \frac{1}{\sqrt{LC}}$  and  $Q$  factor  $Q = \frac{1}{R} \sqrt{\frac{L}{C}} = \frac{\omega_0}{\Delta\omega}$ . By suppressing non-resonant signals, helical resonators with high  $Q$  factor (narrow bandwidth  $\Delta\omega$ ) also act as noise filters, reducing motional heating of the ions [109, 110].

Two helical resonators have been built for drive frequencies of  $\Omega_{\text{rf}}/2\pi \approx$

<sup>19</sup>Rohde & Schwarz, Signal Generator - SMS2, frequency range: 0.1 – 1040 MHz, frequency resolution: 100 Hz, Level: +13 dBm to -137 dBm

<sup>20</sup>Mini Circuits, ZHL-1-2W

2.0 MHz and 7.7 MHz. The design, which is similar for both resonators, is shown in figure 4.11. A list of the particular resonator parameters is shown in table 4.1. A copper coil is wound helically on a cylindrical PTFE core and placed inside

	No. 1	No. 2
coil $\phi$ [mm]	70	45
wire $\phi$ [mm]	1.5	2.5
coil pitch [mm]	2.5	5.5
coil windings	46	12
tube length [mm]	186	108
tube $\phi$ [mm]	140	80.5
$f_0$ [MHz]	2.0	7.7
$U$ [V <sub>pp</sub> ]	165	495

**Table 4.1:** Parameter list of the two helical resonators built for the experiment.

a silver-coated aluminum cylinder tube. One end of the conductor is grounded at the tube while the other end is connected to the ion trap. Helical grooves on the surface, supporting the coil, guide the core when being rotated. The amplified rf input signal is coupled to the coil via a sliding contact at the inside of the coil sticking out of the Teflon core. By rotating the core the tap point is adjusted and thus impedance matching is performed. A capacitive divider at the output allows for monitoring of the signal with reduced amplitude. In addition, a trimmer capacitor<sup>21</sup> in parallel to the output signal allows for fine adjustment of the resonance frequency.

The amplifier and helical resonator are located as close as possible to the ion trap to mitigate unwanted effects as Joule heating and rf crosstalk. Additionally, a voltage variable attenuator<sup>22</sup> attached in between the rf source and amplifier allows to dynamically vary the strength of the trapping potential during the experiment.

---

<sup>21</sup>Voltronics, U.S.A. Trimmer Capacitor, Capacitance Range: 1.5 pF to 40 pF, Voltage Rating: 1 kV

<sup>22</sup>Mini Circuits, ZX73-2500-S

## 4.7 Vacuum system

The vacuum system of the experimental setup meets several requirements.

- UHV at the location of atom-ion interaction to not be limited by background gas collisions during the experiment.
- Use of non-magnetic materials to not perturb the magnetic fields needed in the experiments during operation.
- Antireflective (AR) coated viewports allow for optimal optical access. Additionally, inverted viewports minimize the distance to external magnetic field coils and maximize the numerical aperture (NA) of the imaging system.
- A special vacuum chamber meets the requirements and characteristics of the trap's two-story design and ensures optimal access for magnetic field coils in all axes.

### 4.7.1 Background gas pressure

In atom-ion experiments the time for one experimental cycle is on the order of  $t_{\text{cycle}} = 5\text{--}10\text{ s}$ , where by far most of this time is used to prepare the ultra-cold atomic sample. Thus, to ensure sufficiently long lifetimes of the  ${}^6\text{Li}$  atoms and  $\text{Yb}^+$  ions the experiments are performed in an UHV environment.

In the main chamber two vacuum pumps, an ion getter pump<sup>23</sup> and a regularly fired filament type TSP<sup>24</sup>, provide stable vacuum with a background gas pressure of  $p \leq 10^{-10}$  mbar.

Separated by a differential pumping stage there is the Li oven chamber with an additional ion getter pump of the same type.

### 4.7.2 Main vacuum chamber

One of the hybrid trap's main characteristic is the two-story design as illustrated in section 4.10. The custom-made vacuum chamber<sup>25</sup>, specially designed for this setup, is shown in figure 4.12. To ensure no disturbance of the magnetic fields it is made from low-magnetic 316L stainless steel<sup>26</sup>.

<sup>23</sup>Agilent, VACION PLUS 75 STARCELL, (50 l/s N<sub>2</sub>, 30 l/s Ar)<sub>@p = 10 × 10<sup>-10</sup> mbar</sub>

<sup>24</sup>Agilent, TSP FILAMENT CARTRIDGE

<sup>25</sup>Kimball Physics, Custom MCF 600 Vacuum Chamber

<sup>26</sup>EN steel number 1.4404,  $\mu_r < 1.1$

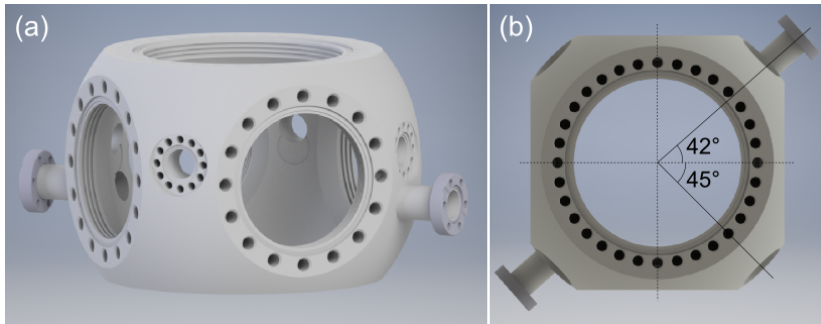
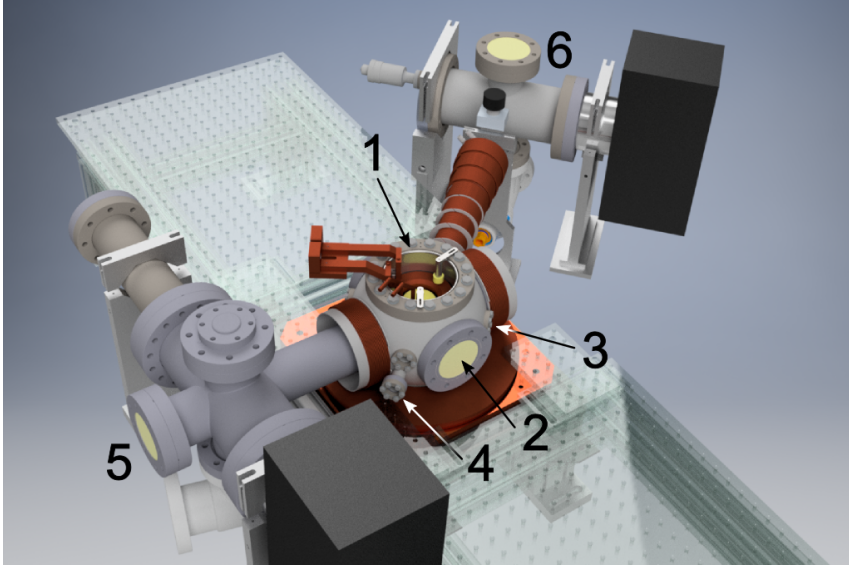


**Figure 4.12:** CAD drawing of customized main vacuum chamber. (a) side view: DN100 CF ports at the top and bottom as well as DN63 CF ports at the flanks offer optimal optical access. Prominent is the custom two-story design with four horizontally aligned DN16 CF ports 10.7 mm above the center plane of the chamber and two horizontally aligned DN16 CF half nipples 16.0 mm below the center plane. (b) For optimal laser access, the four ports above the center plane are under an angle of  $45^\circ$  to the ion trap's axis, while the two half nipples are under an angle of  $42^\circ$  for optimal MOT loading rates without the risk of hitting the MOT mirror with  ${}^6\text{Li}$  atoms.

The chamber has a spherical square shape with two standard DN100 CF ports located at the top and at the bottom as well as four standard DN63 CF ports at the flanks. The four DN16 CF sealing surface ports, by default located at the four corners in-between the DN63 CF ports have been moved 10.7 mm above the center plane of the chamber. This is exactly 4 mm higher than the center of the ion trap<sup>27</sup>. These ports are used for laser access under an angle of  $45^\circ$  to the ion trap axis as can be seen in figure 4.34 (b). The connection line of two additional opposing DN16 CF half nipples 16 mm below the center plane of the chamber crosses the ion trap axis under an angle of  $42^\circ$ . One of these is rotatable and used to connect the Zeeman slower while the other one is used to send in the Zeeman slower laser beam. The angle is optimal for the atom beam to bypass the MOT mirror without the risk of hitting while at the same time ensuring high MOT loading rates.



viewport	quantity	flange size	AR coating for wavelength (nm)	materials (flange / weld ring / glass)
1 <sup>i</sup>	2	DN100	370, 670, 935	316LN, 316L / 316L / Fused Silica
2 <sup>ii</sup>	2	DN63	671, 935, 1068	316LN / Ta / Fused Silica
3 <sup>iii</sup>	4	DN16	370, 935, 1068	316L / Ta / Fused Silica
4 <sup>iv</sup>	1	DN16	671	316LN / Ta / Fused Silica
5 <sup>v</sup>	1	DN63	671	316LN / Ta / Kodial
6 <sup>vi</sup>	1	DN63	–	304L / Kovar / Fused Silica

<sup>i</sup> Kurt J. Lesker, custom re-entrant viewport • <sup>ii</sup> Viewport: Hositrad, HOVPZ64Q-NM, Coating: Tafelmaier • <sup>iii</sup> Vacom, VPCF16UVQ-L-VAR370/935/1068-316L • <sup>iv</sup> Hositrad, HOVPZ16QVAR-NM • <sup>v</sup> Viewport: Hositrad, HOBVPZ64-NM, Coating: Tafelmaier • <sup>vi</sup> Hositrad, HOVPZ64Q

**Figure 4.13 & Table 4.2:** The figure shows the experimental setup without the upper MOT coil assembly and imaging system to reveal the view on hidden viewports. The table gives additional information on all viewports marked in the figure.

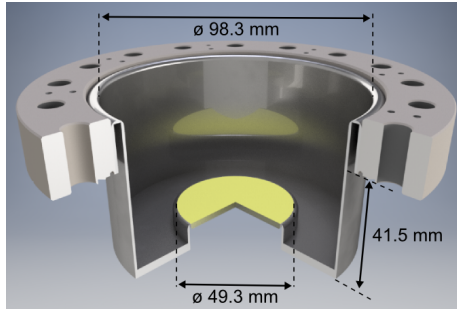


**Figure 4.14:** Sectional drawing of re-entrant viewport.

### 4.7.3 Viewports

Due to the requirements upon the system, most of the viewports had to be custom-made. A list of all viewports with informations on coatings and materials can be found in table 4.2.

The flanges of the viewports in the vicinity of magnetic field coils are made from stainless steel (316L or 316LN) with weld rings made from tantalum<sup>28</sup> as those materials are almost insensitive to magnetic fields.

#### re-entrant viewports

The first item in table 4.2 are two custom-made re-entrant viewports. The design is shown in figure 4.14. The flange is made from stainless steel 316LN, while all other metal parts are made from 316L. The fused silica window is AR coated for 370 nm, 670 nm and 935 nm. The advantages of this design are the following:

1. The upper re-entrant viewport is used for imaging where a high NA is essential. As can be seen in figure 4.6 (b) and (c), the re-entrant viewports are designed to be as close as possible to the hybrid trap, providing a maximum numerical aperture of  $NA_{\max} = 0.15$ <sup>29</sup>.

<sup>27</sup>This height-shift is a compromise due to the finite size of the flanges.

<sup>28</sup>Ta, Z=73, magnetic susceptibility  $\chi_m = 154.0 \times 10^{-6} \text{ cm}^3/\text{mol}$

<sup>29</sup>The NA is primarily limited by the compensation electrodes as can be inferred from figure 4.2. Here, a reduction of the rod diameter from 2 mm to 1.5 mm would increase the maximum numerical aperture to  $NA_{\max} = 0.17$ .

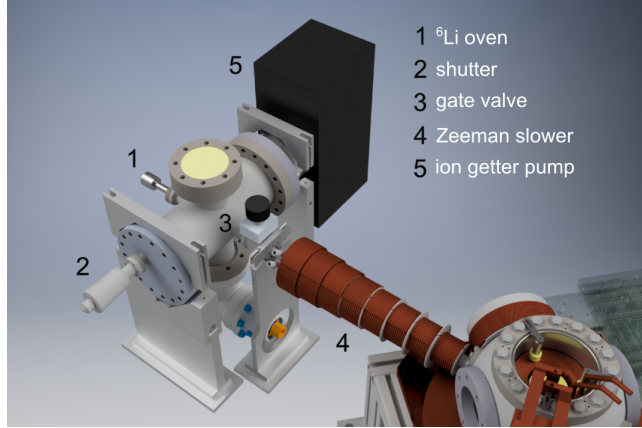


**Figure 4.15:** CAD drawing of oven setup.

2. The bearing surface surrounding the window itself is designated for supporting special high-current magnetic field coils (see chapter 4.8). Here the minimum distance to the atoms and ions ensures maximum yield in terms of magnetic field.

#### 4.7.4 Lithium oven setup

The design and all simulations of the lithium oven setup including the Zeeman slower were done by Henning Fürst [104] and the design was adapted from the group of Prof. Selim Jochim at the University of Heidelberg<sup>30</sup> [111, 112].

The Li oven setup is shown in figure 4.15. It is separated from the main chamber by a differential pumping stage, which is part of a Zeeman slower, and a UHV-gate valve<sup>31</sup>. The valve offers the possibility to refill the oven while the main chamber maintains under vacuum. A motorized mechanical shutter provides deterministic loading of atoms into the MOT and increases its lifetime when closed.

In order to ensure a high atom flux, the temperature of the oven is  $T_{\text{oven}} \approx 400^\circ\text{C}$  which limits the minimum pressure reachable in the oven chamber to  $p \approx 10^{-9}$  mbar. The differential pumping stage allows to connect the oven chamber to the main chamber, while maintaining stable UHV in the main chamber.

<sup>30</sup>[www.lithium6.de](http://www.lithium6.de)

<sup>31</sup>Vacom, 5GVM-16CF-MV-S

### Zeeman slower

The velocity of the  ${}^6\text{Li}$  atoms<sup>32</sup> emerging from the oven follows a thermal velocity distribution. The mean velocity is on the order of several 100 m/s. In order to increase the MOT loading efficiency their mean velocity is decreased in a Zeeman slower to a narrow velocity distribution peaked around  $v_{\text{mean}} \approx 50$  m/s. A higher MOT loading efficiency also means shorter experimental cycles. Thus, less time is needed to acquire statistics in measurements. Additionally, the atomic beam leaving the Zeeman slower is reasonably collimated. Therefore, the contamination with  ${}^6\text{Li}$  of vacuum components in the main chamber, e.g. the hybrid trap, is mitigated.

The Zeeman slower is composed of a linear polarized laser beam, red detuned to the  $D2$  transition of  ${}^6\text{Li}$ , slightly focused onto the atom-source and a magnetic field which decreases while the atoms approach the MOT. A CAD drawing of the Zeeman slower, the calculated horizontal magnetic fields and the evolution of different velocity classes in phase-space is shown in figure 4.16.

The working principle of a Zeeman slower is as follows: As the atoms approach the Zeeman slower region the atomic transitions are Doppler shifted according to their velocity. The magnetic field induces a Zeeman shift to the atomic resonance frequency which almost cancels the Doppler shift. This leads to efficient Doppler cooling of the atoms. A decreasing Zeeman shift during the transit, due to shrinking magnetic fields, compensates the decreasing Doppler shift of the cooling transition during the slow-down, ensuring continuous and efficient cooling until the atoms enter the MOT. In addition, the slight focus of the cooling beam provides additional collimation of the atomic beam.

A detailed description of the Lithium oven setup including the Zeeman slower is given in Ref. [104].

---

<sup>32</sup>Sigma-Aldrich, Lithium-6, Chunks, 95 Atom %  ${}^6\text{Li}$ , 340421-10G

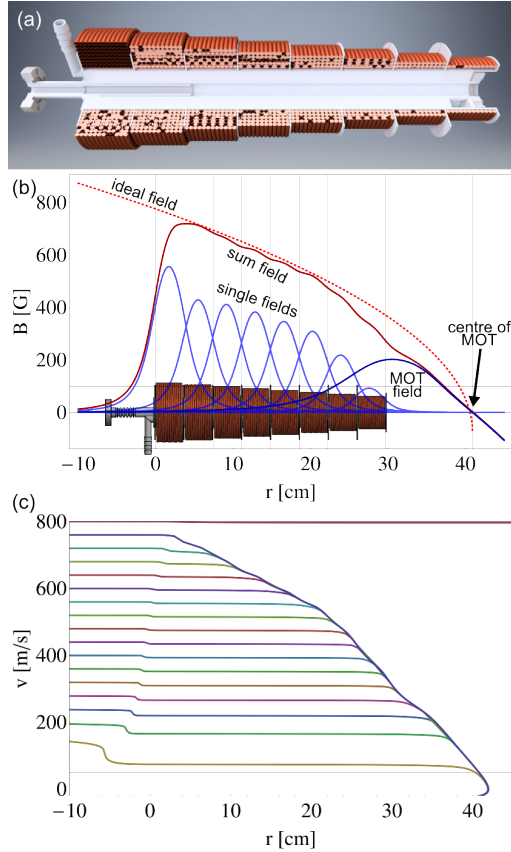
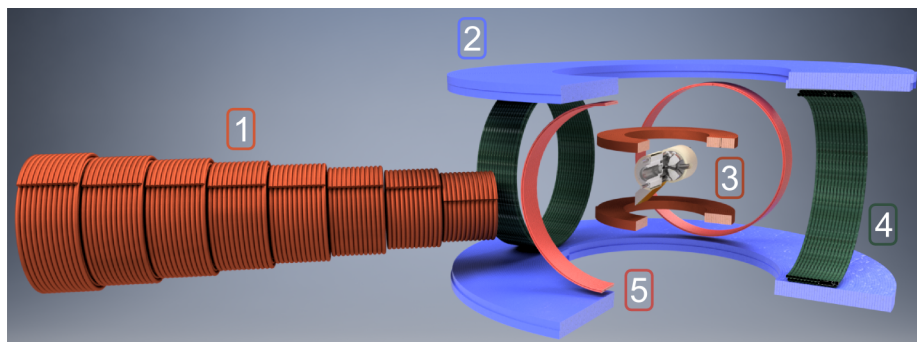


**Figure 4.16:** (a) Sectional drawing of Zeeman slower. The  $^6\text{Li}$  atoms approach from the left. As they traverse, the inner diameter of the tube increases in 2 steps from 6 mm over 8 mm to 13 mm. Due to Joule heating the Zeeman slower needs to be water-cooled. For this the cooling water flows subsequently through four chambers in-between the coils and the vacuum tube. (b) Simulation of the horizontal magnetic fields for the Zeeman slower design. The sum field is composed of the single magnetic fields generated by eight coils with decreasing number of windings at the Zeeman slower and the quadrupole field of the MOT coils. Here, the horizontal MOT field is essential to bridge the space between the Zeeman slower and the MOT region. (c) Phase space diagram for  $^6\text{Li}$  atoms of different velocity classes transiting the Zeeman slower. The ideal field in (b) would efficiently decelerate all desired velocity classes with  $v_{\text{mean}} \leq 800$  m/s.



coil	name	$B/I$ (G/A)	$\nabla B/I$ (G/(A cm))	$I_{\max}$ (A)	$N$	$R$ ( $m\Omega$ )	water cooled
1	Zeeman slower	see text	–	s.t.	s.t.	s.t.	yes
2	MOT coils	–	0.8	53	98	190	yes
3	Feshbach coils	2.63	1.17	320	16	10.6	yes
4	radial compensation coils	9.6	–	50	30	70	no
5	axial compensation coils	0.7	–	10	30	260	no

**Figure 4.17 & Table 4.3:** CAD drawing of coil setup with ion trap for orientation. Additional information on the particular coils is given in the table. Here,  $B/I$  and  $\nabla B/I$  denote the magnetic field strength and magnetic field gradient at the center of the ion trap per amp, respectively.

## 4.8 Magnetic field coils

A multitude of magnetic field coils has been implemented into the setup providing the magnetic fields necessary. They are shown in figure 4.17.

### Zeeman slower

As explained in chapter 4.7.4 and shown in figure 4.16 (b) the magnetic field of the Zeeman slower continuously decreases starting from approximately 735 G to 0 G as the decelerating atoms approach the MOT. It is composed of eight magnetic field coils with shrinking number of windings as listed in table 4.4.

coil	1	2	3	4	5	6	7	8
N	415	325	297	264	232	198	130	64
R ( $m\Omega$ )	1492	1082	979	852	730	613	392	193
I (A)	6.4	6.4	6.4	6.4	6.4	6.4	6.4	5.4

**Table 4.4:** Number of windings (N) of, resistance of and applied current at respective Zeeman slower coils.

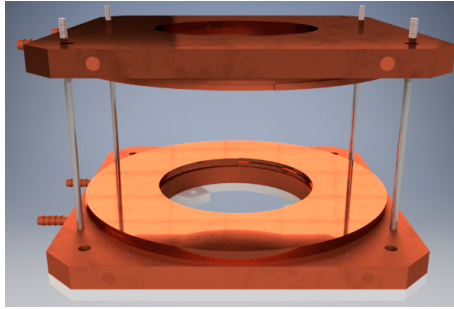


**Figure 4.18:** CAD drawing of MOT coil assembly. Each coil is fixed to a 20 mm thick, water-cooled, copper heat sink. The lower heat sink is screwed on a 10 mm thick aluminum board at the bottom, which itself is screwed on ITEM profiles. This board also serves as mount for the main vacuum chamber (Through boreholes in the center clearance hole).

### MOT coils

Subsequently the atoms are pre-trapped in a MOT, while the magnetic field of the MOT coils also contributes to the magnetic field of the Zeeman slower.

To form a magnetic gradient field there are two coils in anti-Helmholtz configuration on top and below the main vacuum chamber. Thus, the vertical distance between the coils is relatively large with approximately 125 mm. The coil wire<sup>33</sup> has a rectangular cross section and is helically wound. Two layers, each with 49 windings, form one coil with  $N = 98$  windings, while each coil is fixed to a water-cooled, copper heat sink which also serves as mount. A CAD drawing of the MOT coil assembly is shown in figure 4.18. In the experiment the MOT coils are supplied with  $I = 38$  A which generates a magnetic gradient field of  $\nabla B_z = 2\nabla B_{\text{rad}} \approx 36$  G/cm in the center of the chamber.

<sup>33</sup>Karl Ruggaber GmbH & Co. KG, 5,00x1,40mm Multogan / Damid 200, Grade 2,  $T_{\text{max}} = 200^\circ\text{C}$



**Figure 4.19:** (a) Sectional drawing and (b) picture of assembled Feshbach coil setup.

### Feshbach coils

The most sophisticated magnetic field coils in our setup are the high-current coils as shown in figure 4.19. The initial design was – as the design of the Li oven and Zeeman slower – adapted from the group of Prof. Selim Jochim at the University of Heidelberg [113]. In Heidelberg these coils have been developed to scan the atomic scattering length over a wide range ( $B_{\max} = 1500$  G) to tune the strength of the atom-atom interaction by means of Feshbach resonances.

In order to create a degenerate Fermi gas the design goal for the coils in our setup is to excite the broad Feshbach resonance between the energetically lowest Zeeman hyperfine levels of the  ${}^6\text{Li } 2\text{S}_{1/2}$  ground state ( $|F = 1/2, m_F = 1/2\rangle \leftrightarrow |F = 1/2, m_F = -1/2\rangle$ ) at 834 G [114] (hence the name "Feshbach coils"). Additionally, as explained in chapters 5 and 6 the Feshbach coils serve to support the MOT, to form a magnetic trap, to realize the magnetic transport of the  ${}^6\text{Li}$  atoms to the  $\text{Yb}^+$  ions and also to generate the magnetic fields necessary for operations on the  $\text{Yb}^+$  ions such as state preparation.

The whole design is optimized for optimal heat transport from the coil and the electrical connectors to the cooling body. Besides, their tiny inductance due to a small number of windings allows for fast switching the coils on or off as well as for fast switching from Helmholtz to anti-Helmholtz configuration<sup>34</sup> both in the order of 1 ms. As an additional feature, the coils fit exactly in the re-entrant viewports presented in chapter 4.7.3. Thus, the distances from the coils to the interaction region is minimized ensuring the highest fields possible, as the field strength of a Helmholtz-coil pair scales with the inverse of the distance.

The possibility to provide large magnetic fields, by powering the coils with high currents results from the special and unconventional construction method

<sup>34</sup>Details about the home-made high-current switch can be found in Ref. [104].

applied for building the coils. Similar to the MOT coil, an isolated wire<sup>35</sup> with rectangular cross section is wound helically. As a next step, the thermal conductivity between the coil and the water-cooled heat sink is improved significantly. In order to do so, the coating at the upper surface of the coil is removed before the coil and the electrical connectors are directly adhered to the heat sink with electrical insulating epoxy of high thermal conductivity<sup>36</sup>. The distance between the wire and cooling body is about 0.1 mm.

A detailed construction manual and documentation can be found in appendix D.

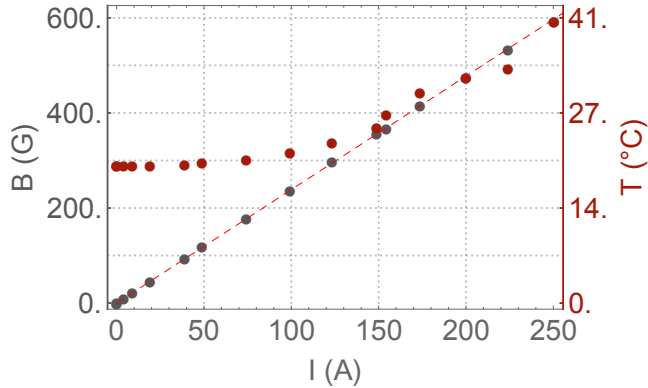


**Figure 4.20:** Magnetic field and temperature measurement for a single Feshbach coil in dependence to electric current (continuous operation). The temperature is measured at the most critical point, the junction from coil to connector.

Both Feshbach coils are driven separately<sup>37</sup> which, in anti-Helmholtz configuration, allows to dynamically shift the height of the magnetic quadrupole field minimum.

Figure 4.20 shows a magnetic field measurement at the center of a single Feshbach coil. Additionally, the temperature of the coil is traced at the junction from coil to connector as it is the location of highest electrical resistance. From

<sup>35</sup>MEFFERT Elektro - Isoliertechnik GmbH, Flachlackdraht, IEC 60317-29, G2, dimensions: 6.30 x 1.00 mm,  $T_{\max} = 200^{\circ}\text{C}$

<sup>36</sup>EPO-TEK® T905BN-3, Thermal Adhesive Two-part, thermal conductivity: 2.02 W/mK

<sup>37</sup>Delta Elektronika, SM15-400,  $U_{\max} = 15.0\text{ V}$ ,  $I_{\max} = 400\text{ A}$ ,  $P_{\max} = 6000\text{ W}$

this and similar measurements we conclude, that the coils can safely be operated with a maximum continuous current of  $I = 220$  A. By measuring the resistance of the coil we can estimate the residual mean thickness<sup>38</sup> of the coil wire to be 5.84 mm. With the number of windings ( $N = 16$ ) and the distance of the coils to the center ( $d = 2.3$  mm) we can simulate the magnetic field for any current at every location.

The calculated strength of the magnetic field generated by both Feshbach coils at the ion position in dependence to the electric current at both coils is  $B(I) = 2.63 \times I$ . To excite the Feshbach resonance at 834 G a current of 317 A needs to be supplied. We expect that the time needed for evaporative cooling is in the order of 2.5 s [115]. For short pulses of  $t \leq 3$  s and maximum currents of  $I = 320$  A no significant heating of the coils was observed such that the coils are well suited for the experiment.

### Compensation coils

As the position of the MOT is not located in the center of the chamber, an additional homogeneous magnetic field pushes the minimum of the magnetic gradient field of the MOT coils to the desired position. Subsequently, for the magnetic transport of the  ${}^6\text{Li}$  atoms, the field minimum is dynamically moved from the MOT location into the ion trap. Also further experimental procedures with the atoms and ions require magnetic fields in all axes. Therefore, additional two pairs of magnetic field coils have been implemented into the setup as shown in figure 4.17.

---

<sup>38</sup>While removing the coating of the wound coil at the upper surface also some wire material is taken off to guarantee for optimal smoothness of the surface.

## 4.9 Laser setup

	$\lambda$ (nm)	manufacturer	application	$P_{\max}$ (mW)	$\emptyset$ (mm <sup>2</sup> )
<b>Yb I</b>	399	home-made	photoionization	120	3
<b>Yb II</b>	369	Toptica	<i>D1</i>	12.5	3
	329	Toptica	<i>D2</i>	300	1
	935	Toptica	Repumper	86	3
	638	home-made	Re-Repumper	150	3
<b><sup>6</sup>Li</b>	671	Toptica	<i>D2</i>	517	3
	671	Radiant Dyes	<i>D1</i>	15	3
	1070	IPG	crossed ODT	200 W	44

**Table 4.5:** Laser systems in the experiment. More information on the systems is given in the corresponding sections.

In order to drive all relevant transitions of the Yb atom and ion as well as of neutral lithium eight different laser systems are operated at the experiment. The laser systems application and their basic properties are listed in table 4.5.

### 4.9.1 Laser systems for Yb

The experiments presented in this thesis are performed on Yb<sup>+</sup> ions of isotopes <sup>171</sup>Yb<sup>+</sup>, <sup>174</sup>Yb<sup>+</sup> and <sup>176</sup>Yb<sup>+</sup>. While the latter do not possess a nuclear spin, <sup>171</sup>Yb<sup>+</sup> has a spin- $\frac{1}{2}$  nucleus resulting in a hyperfine substructure. In figure 4.21 the relevant energy level structure, transitions and lifetimes of <sup>171</sup>Yb<sup>+</sup> are shown<sup>39</sup>. The inset shows the hyperfine structure of the <sup>2</sup>S<sub>1/2</sub> ground state.

#### Laser system for photoionization of neutral Yb

Isotope-selective two-step photoionization of neutral Yb atoms is employed in order to load Yb<sup>+</sup> ions into the Paul trap [116]. The scheme of this resonantly enhanced process is shown in figure 4.22.

A beam of neutral atoms is generated in the Yb oven as explained in section 4.4.3 and crosses the center of the ion trap where it is overlapped with

<sup>39</sup>See also appendix A for more informations and references.

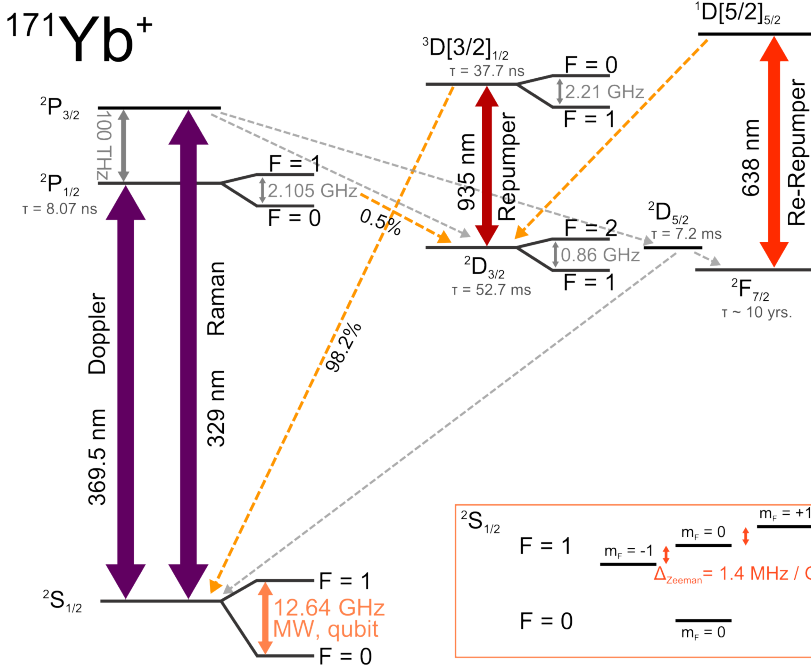
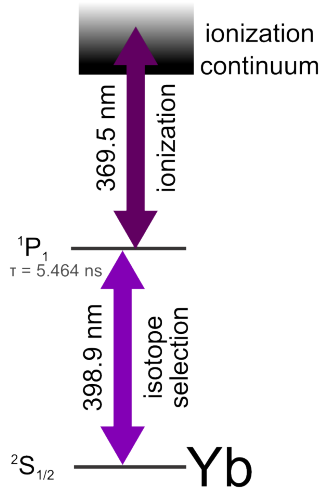


Figure 4.21: Relevant energy levels and transitions of  $^{171}\text{Yb}^+$ .

two laser beams in order to perform the ionization process. The first step of the two-step process is a resonant excitation from the  $^1S_0$  ground state to the excited state  $^1P_1$  with an atomic radiative lifetime of  $\tau_P = 5.464 \text{ ns}$ , hence a natural linewidth of  $\Gamma_P = \tau^{-1} = 2\pi \times 29.1 \text{ MHz}$  and saturation intensity  $I_{\text{sat},^1P_1} = 60 \text{ mW/cm}^2$  [117]. In order to drive the transition a home-made, grating-stabilized external-cavity diode laser (ECDL) system in Littrow configuration<sup>40</sup> at  $\lambda = 398.9 \text{ nm}$  provides  $P \approx 1.5 \text{ mW}$  optical power, focused through the center of the ion trap with a waist of  $w = 0.75 \text{ mm}$ , yielding  $I_{\text{peak}} \approx 80 \text{ mW/cm}^2$  [118].

Isotope selectivity stems from the isotope shift of the  $^1S_0 \leftrightarrow ^1P_1$  line, listed in table A.3. Thus, it is realized by tuning the wavelength of the first step laser on resonance of a particular isotope's transition. A scheme of the 398.9 nm laser system is shown in figure 4.23. As the laser beam orientation is orthogonal to

<sup>40</sup>Detailed information on the home-made laser systems can be found in Ref. [118].



**Figure 4.22:** Scheme for isotope-selective two-step photoionization of neutral Yb atoms. By tuning the wavelength of the first step laser the  $^1P_1$  state of a certain isotope in a mixture of natural isotopic abundance can selectively be excited. The second step laser, to reach the continuum, at  $\lambda = 369.5$  nm also acts as Doppler cooling laser for  $Yb^+$  ions.

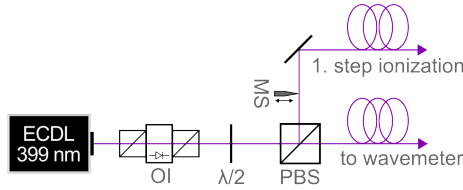


**Figure 4.23:** Scheme of 398 nm laser setup.

the direction of the atom beam, the effect of first order Doppler broadening is mitigated. Frequency stabilization is realized by means of a software lock. Here, the laser frequency, measured by the wavemeter, is continuously monitored and compared to a set frequency. Direct grating feedback corrects for occurring frequency-deviations. Compared to state-of-the-art active stabilization techniques as locking to a reference cavity, software frequency stabilization has a longer response time resulting in short-time frequency fluctuations and strongly depends on the accuracy and sensitivity of the wavemeter used. However, depending on the application it can be advisable to use this technique as it is a simple and relatively cheap solution.

The second step is a non-resonant excitation with wavelength  $\lambda < 394$  nm as it is sufficient for exceeding the ionization energy. A suitable laser system which is already part of the setup is the 369 nm Doppler cooling laser for  $Yb^+$ . The

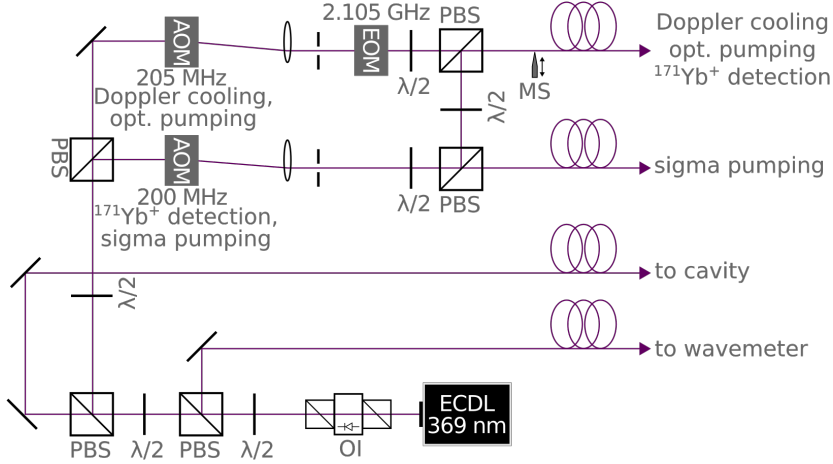


**Figure 4.24:** Scheme of 369 nm laser setup.

two laser beams are superposed at the ion trap center. Home-made mechanical shutters (MS) [118,119] in the beam paths allow for controlled loading of ions. Here, the ion loading rate strongly depends on the atom flux which in turn depends on the oven temperature. It can therefore be tuned from a few ions per second to reliable single ion loading.

### Laser system to drive the $D1$ line of $\text{Yb}^+$ for Doppler cooling, state preparation and state detection

Doppler cooling of  $\text{Yb}^+$  ions is performed close to resonance on the  $^2S_{1/2} \leftrightarrow ^2P_{1/2}$  dipole transition. The  $^2P_{1/2}$  state has a lifetime of  $\tau = 8.07(9)$  ns, thus a natural linewidth of  $\Gamma_P = 2\pi \times 19.7(2)$  MHz and the transition has saturation intensity  $I_{\text{sat},D1} = \pi\hbar c\Gamma_{SP}/(3\lambda^3) = 51 \text{ mW/cm}^2$  [120]. Additionally, the transition is used for state initialization and state detection of  $\text{Yb}^+$  ions as explained in chapter 5.4. A scheme of the laser setup is shown in figure 4.24. The laser system is an ECDL<sup>41</sup> which is locked to a home-made low-finesse cavity by means of Pound-Drever-Hall (PDH) method [121] as described in chapter 4.9.3. Two tunable acousto-optic modulators (AOMs)<sup>42</sup> provide shifting of the laser beams to the desired frequency.

<sup>41</sup>Toptica, SYST DL PRO, cw, 370 nm,  $P_{\text{max}} = 12.5$  mW

<sup>42</sup>Gooch and Housego, AOM 3200-1210, 200 MHz, 325–365 nm, aperture: 0.25 mm

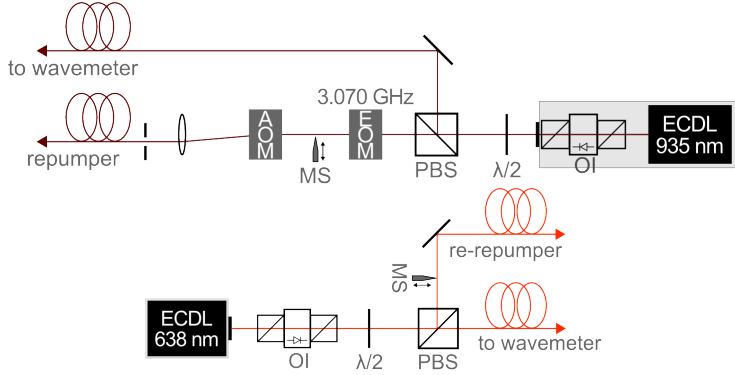


**Figure 4.25:** Scheme of 935 nm and 638 nm laser setups.

For Doppler cooling of  $\text{Yb}^+$  ions a laser beam with  $P \approx 25 \mu\text{W}$  optical power is focused through the center of the ion trap with a waist of  $w = 0.12 \text{ mm}$ , yielding a peak intensity of  $I_{\text{peak}} \approx 50 \text{ mW/cm}^2$ .

**special case:**  $^{171}\text{Yb}^+$  As the hyperfine splitting between the  $^2\text{P}_{1/2}$  sub-states in  $^{171}\text{Yb}^+$  is  $\Delta E = 2.105 \text{ GHz}$ , there is a small but non-negligible off-resonant coupling between the states  $^2\text{S}_{1/2} |F=1\rangle$  and  $^2\text{P}_{1/2} |F=1\rangle$  leading to indirect optical pumping into the "dark" state  $^2\text{S}_{1/2} |F=0\rangle$ . A microwave (MW) field with frequency  $f_{\text{MW}} = 12.64 \text{ GHz}$  is irradiated which couples both  $^{171}\text{Yb}^+$   $^2\text{S}_{1/2} |F=0,1\rangle$  hyperfine states, closing the cooling cycle<sup>43</sup>. The 2.105 GHz electro-optic modulator (EOM)<sup>44</sup> is used for reliable state preparation as explained in chapter 5.4.1.

### Repumper and re-repumper

During Doppler cooling there is a small probability that the excited state  $^2\text{P}_{1/2}$  leaks to the metastable  $^2\text{D}_{3/2}$  state ( $\tau = 52.7 \text{ ms}$ ) with a branching ratio of about 1:200. An additional ECDL<sup>45</sup>, the so-called repumper, couples this state to the short-living  $^3\text{D}[3/2]_{1/2}$  state ( $\tau = 37.7 \text{ ns}$ ) which decays to the  $^2\text{S}_{1/2}$  ground

<sup>43</sup>More information on the MW source can be found in Ref. [104].

<sup>44</sup>QUBIG, EO-T2100M3-VIS, resonant, high-Q electro-optic phase modulator, tunable resonance frequency: ca. 2.0–2.2 GHz (preset: 2105 MHz), MgO:LN  $3 \times 3 \text{ mm}$  aperture

<sup>45</sup>Toptica, SYST DL PRO, cw, 935 nm,  $P_{\text{max}} = 86.0 \text{ mW}$

state with a probability of 98.2%. In case of  $^{171}\text{Yb}^+$  an EOM<sup>46</sup> adds sidebands on the repumper-transition to depopulate both  $^2\text{D}_{3/2}$  hyperfine states. The repumper is stabilized via software frequency stabilization as described above.

Additionally, non-radiative processes, such as collisions with background gas molecules may cause the  $\text{Yb}^+$  ion state to decay from one of the excited states to the energetically lower state  $^2\text{F}_{7/2}$  which has a lifetime of  $\tau \approx 10$  years. A home-made, grating-stabilized ECDL (see Ref. [118]), the so-called re-repumper, at  $\lambda \approx 638$  nm couples this state to the  $^1\text{D}[5/2]_{5/2}$  state which decays to the  $^2\text{D}_{3/2}$  state and such is fed back into the cooling cycle. Also the re-repumper is stabilized via software frequency stabilization. A scheme of both laser setups is shown in figure 4.25.

### Laser system to drive the $D_2$ line of $\text{Yb}^+$ for Raman spectroscopy and optical pumping to $^2\text{F}_{7/2}$

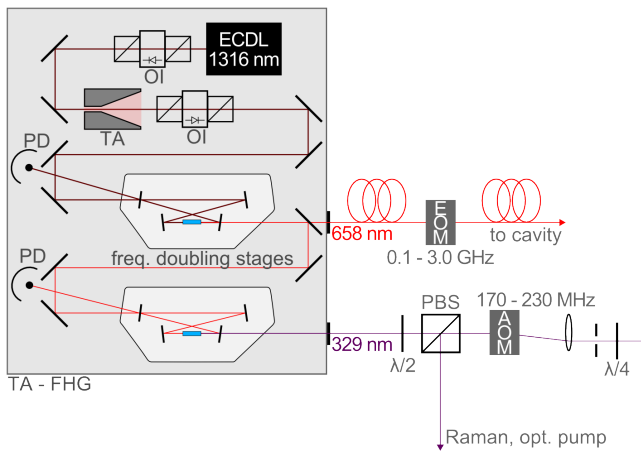


**Figure 4.26:** Scheme of 329 nm ( $D_2$  line) laser setup (see text for description).

The  $^2\text{S}_{1/2} \leftrightarrow ^2\text{P}_{3/2}$  dipole transition ( $D_2$  line) is used for Raman spectroscopy and for optical pumping of the  $\text{Yb}^+$  ion into the very long lived  $^2\text{F}_{7/2}$  state with  $\tau \approx 10$  yr. The lifetime of the  $^2\text{P}_{3/2}$  state is  $\tau = 6.15(9)$  ns yielding a natural linewidth of  $\Gamma_{\text{P}} = 2\pi \times 25.9(4)$  MHz [120].

<sup>46</sup>QUBIG, EO-T3070M3-VIS, resonant, high-Q electro-optic phase modulator, tunable resonance frequency: ca. 2.9-3.1 GHz (preset: 3070 MHz), MgO:LN 3x3mm aperture

The transition is driven with a frequency-quadrupled high power laser system<sup>47</sup>. Here, the laser beam, emitted in a grating-stabilized ECDL, is amplified in a tapered semiconductor amplifier (TA) before being frequency quadrupled in a cascade of two second harmonic generation (SHG) stages, which are composed of a resonant cavity and a non-linear crystal (see figure 4.26). After the first SHG stage, a small fraction of the light is coupled out for frequency stabilization with an external optical cavity (see section 4.9.3). Here, a tunable EOM allows to offset the carrier frequency from the resonance frequency of the carrier mode at the cavity. The AOM in double-pass is used for pulse shaping and frequency scanning of the main beam before being coupled to the experiment.

## 4.9.2 Laser systems for ${}^6\text{Li}$

A detailed description of  ${}^6\text{Li}$ , with all necessary properties of the relevant transitions and energy levels used below, can be found in Ref. [122]. The relevant energy levels and transitions of  ${}^6\text{Li}$  are shown in figure 4.27<sup>48</sup>. Two laser systems drive the  $D1$  and  $D2$  line, respectively. A full description of the laser setup for  ${}^6\text{Li}$  is given in Ref. [104].

### Laser system to drive the $D2$ line of ${}^6\text{Li}$

Trapping, cooling and imaging of neutral  ${}^6\text{Li}$  atoms is performed on the  $D2$  line ( ${}^2\text{S}_{1/2} \leftrightarrow {}^2\text{P}_{3/2}$  transition) with wavelength  $\lambda = 670.977$  nm. The  ${}^2\text{P}_{3/2}$  state has a lifetime of  $\tau = 27.102$  ns and thus a natural linewidth of  $\Gamma_{D2} = 2\pi \times 5.872$  MHz and saturation intensity  $I_{\text{sat},D2} = 2.54$  mW/cm<sup>2</sup> [122].

A scheme of the laser setup is shown in figure 4.28. An ECDL system with TA<sup>49</sup> provides  $P_{\text{max}} = 517.0$  mW optical power. Between the first optical isolator (OI) and the TA a probe beam is diverted to monitor the wavelength. The ECDL is stabilized with a reference optical cavity and additionally offset-locked to a spectroscopy lithium cell as described in section 4.9.3.

Due to a small hyperfine constant of the  ${}^2\text{P}_{3/2}$  state<sup>50</sup> the splitting of its hyperfine states ( $\Delta E_{\text{total},2\text{P}_{3/2}}/h = 4.4$  MHz) cannot be resolved. In contrast, the hyperfine constant of the  ${}^2\text{S}_{1/2}$  state<sup>51</sup> leads to a total splitting of

<sup>47</sup>Toptica, SYST TA-FHG PRO, cw, design wavelength: 323 nm,  $P > 300$  mW (323–326 nm), Coarse tuning: 323–330 nm

<sup>48</sup>See also appendix B for more informations and references.

<sup>49</sup>Toptica, SYST TA PRO 670, cw, 671 nm,  $P_{\text{max}} = 517.0$  mW

<sup>50</sup> $A_{2\text{P}_{3/2}} = -1.155$  MHz [122]

<sup>51</sup> $A_{2\text{S}_{1/2}} = 152.136$  MHz [122]

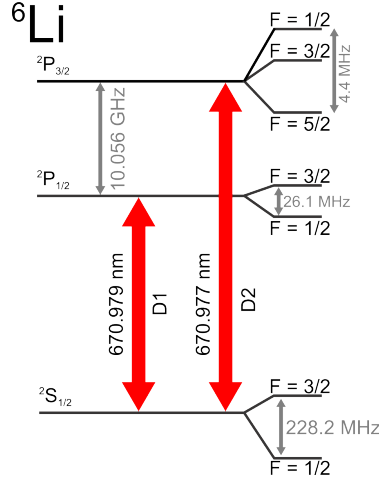


**Figure 4.27:** Relevant energy levels and transitions of  ${}^6\text{Li}$  (taken from Ref. [122]). Energy splittings are not to scale.

$\Delta E_{\text{total}, {}^2S_{1/2}}/h = 228.2 \text{ MHz}$ . Therefore, in order to close the cooling cycle the following two transitions are driven:

$$\begin{aligned} \text{Cooling transition:} & \quad {}^2S_{1/2} |F = 3/2\rangle \leftrightarrow {}^2P_{3/2} \\ \text{Repumper transition:} & \quad {}^2S_{1/2} |F = 1/2\rangle \leftrightarrow {}^2P_{3/2} \end{aligned}$$

In the laser setup a fraction of the laser light is shifted by 228.2 MHz using an AOM<sup>52</sup> (1) in order to drive both transitions. Both beams are being superposed at a polarizing beam splitter (PBS) (2) before being coupled into the experiment. An AOM<sup>53</sup> at  $-100 \text{ MHz}$  (3) is used for fast switching on/off of the MOT beams and the Zeeman slower beam. For the latter, an AOM<sup>54</sup> (4) shifts the frequency by additional  $-70 \text{ MHz}$  to be red detuned from the thermal and Doppler broadened transition of the hot atoms counterpropagating to the laser beam. For absorption imaging the frequency of the light is shifted by  $-80 \text{ MHz}$  to be on resonance with the  $D2$  line via an additional AOM<sup>55</sup> (5). Before being coupled to the external optical cavity and spectroscopy cell for frequency sta-

<sup>52</sup>Goch and Housego, AOM 3200-125, 200 MHz, 470–690 nm, aperture: 1.5 mm

<sup>53</sup>Goch and Housego, AOM 3100-125, 100 MHz, 470–690 nm, aperture: 1.5 mm

<sup>54</sup>Goch and Housego, AOM 3080-125, 80 MHz, 442–633 nm, aperture: 2 mm

<sup>55</sup>Goch and Housego, AOM 3080-122, 80 MHz, 780–950 nm, aperture: 1 mm



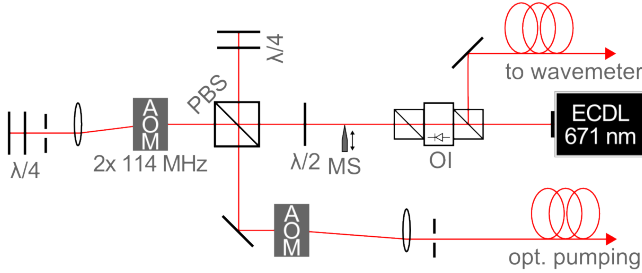


**Figure 4.29:** Scheme of 671 nm ( $D1$  line) laser setup.

The AOM<sup>58</sup> in double-pass configuration adds a fraction of laser light shifted by 228.2 MHz which corresponds to the repumper transition as described for the  $D2$  line laser setup (see 4.9.2) while the second AOM<sup>59</sup> in single-pass configuration in combination with an iris provide pulse shaping. A mechanical shutter is used to additionally block the laser beam.

### Laser system for the crossed optical dipole trap

After trapping and pre-cooling of the  ${}^6\text{Li}$  atoms they are to be loaded into a crossed ODT. The trapping potential is created by two red-detuned far-off resonant laser beams focused through the ion trap center under  $\phi = 4^\circ$  angle of incidence. As explained in Ref. [20], crossed ODTs are best suited for evaporative cooling since they provide reasonable trapping volumes and tight confinement independent of the magnetic field.

In the experiment a single-mode, Yb cw fiber laser system<sup>60</sup> operating at  $\lambda = 1070\text{ nm}$  provides  $P_{\text{max}} = 200\text{ W}$  optical power to create a suitable deep trapping potential as the trap depth is proportional to laser intensity. In order to illustrate the beam paths and the shape of the trapping potential the intensity profile of the laser field within the ion trap is plotted in figure 4.30.

The experiments presented in this thesis were performed in the magnetic trap. In November 2017, the group achieved optical trapping of  ${}^6\text{Li}$  atoms as will be presented in the PhD thesis by Henning Fürst [104].

<sup>58</sup>Gooch and Housego, AOM 3100-125, 100 MHz, 470–690 nm, aperture: 1.5 mm

<sup>59</sup>Gooch and Housego, AOM 3100-125, 100 MHz, 470–690 nm, aperture: 1.5 mm

<sup>60</sup>IPG Laser GmbH, YLR-200-LP-WC, Ytterbium Fiber Laser LP,  $P_{\text{max}} = 200\text{ W}$ , water cooled, with guide laser

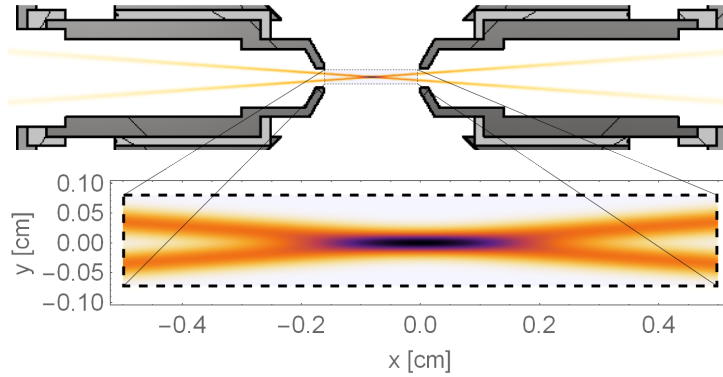


**Figure 4.30:** Intensity profile of the crossed ODT within the ion trap.

### 4.9.3 Frequency stabilization

The main  $\text{Yb}^+$  ion ECDLs ( $D1$  and  $D2$ , see 4.9.1) and the main  $^6\text{Li}$  ECDL ( $D2$ , see 4.9.2) are frequency stabilized on an external optical reference cavity. Additionally, for the latter the cavity resonance is locked to a lithium spectroscopy cell via saturated absorption spectroscopy.

Frequency stabilization is appropriate for applications such as Doppler cooling as here the laser frequency is red detuned close to resonance. A stable laser frequency provides reliable cooling without fluctuations in temperature. Furthermore, when driving an atomic transition the fluctuation of the laser frequency needs to be small compared to the linewidth of the resonance. Additionally, locking the cavity resonance to the spectroscopy transition of  $^6\text{Li}$  provides absorption imaging exactly on resonance of the transition which is essential to get an accurate atom number.

#### Optical reference cavity

The basic cavity design and the setup for laser frequency stabilization is shown in figure 4.31<sup>61</sup>. The optical cavity is composed of a plane<sup>62</sup> (1) and a concave<sup>63</sup>

<sup>61</sup>For the design see appendix E.

<sup>62</sup>Altechna, Partially reflecting mirror, Material: UVFS, Diameter: 12.7 mm ( $\pm 0.1$  mm), Thickness: 5 mm ( $\pm 0.1$  mm), Coatings: S1: PR( $R=99.0\% \pm 0.2\%$ ), S2: AR( $R < 0.25\%$ )

<sup>63</sup>Altechna, Partially reflecting concave mirror, same parameters as plane mirror, radius of curvature (ROC):  $ROC = -250$  mm

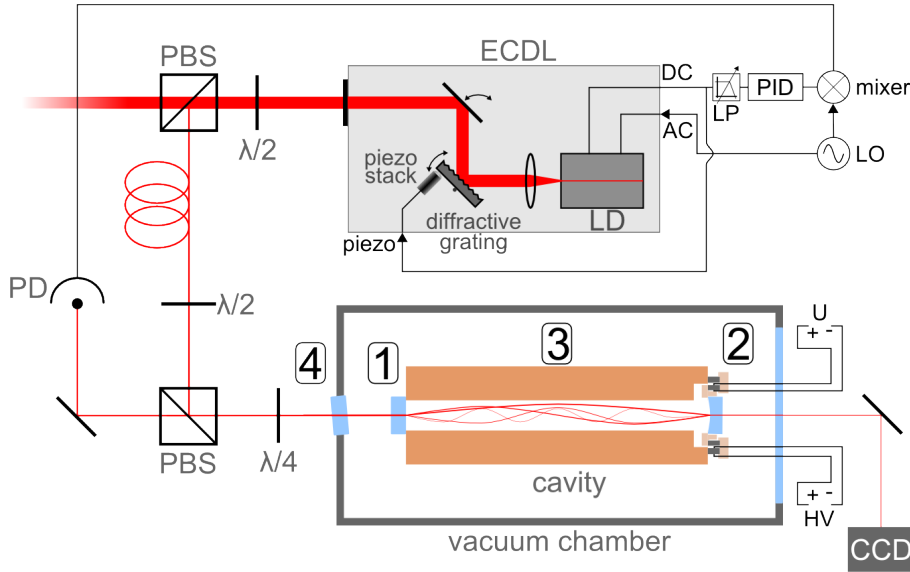


**Figure 4.31:** Frequency stabilization with an optical cavity. (1) partial reflection (PR) coated plane mirror, (2) PR coated plano-concave mirror in piezo assembly, (3) Zerodur spacer, (4) AR coated precision window under 5° angle.

(2) mirror arranged in hemispherical configuration. The mirrors are PR coated for the particular wavelengths providing a reflectivity of  $R = 99.0(2)\%$ . The plano-concave cavity mirror is mounted on an assembly<sup>64</sup> of two custom-made ring-shaped piezo elements<sup>65</sup>. Due to the arrangement the thermal expansion of both piezo elements cancel each other. A custom-made Zerodur-block<sup>66</sup> with a borehole (3) serves as mount with cavity length  $L_{cav} = 100$  mm. Due to its tiny coefficient of thermal expansion<sup>67</sup>  $L_{cav}$  is insensitive to slight temperature drifts of the system. For additional stabilization and to decouple it from the environment the cavity is placed in a vacuum chamber with  $p \leq 1.33 \times 10^{-8}$  mbar. Here, the entrance window<sup>68</sup> (4) is built-in under an angle of 5° to the beam path in order to prevent reflections superimposing with the cavity modes. The char-

<sup>64</sup>For a sectional drawing see figure E.1

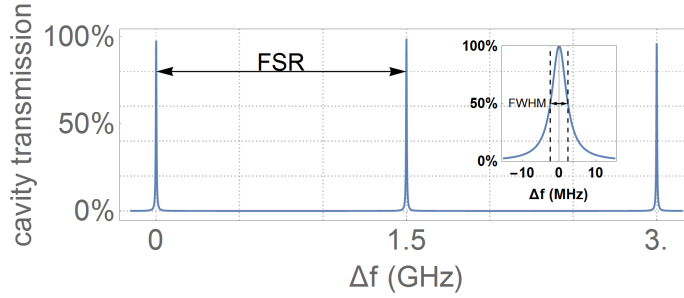
<sup>65</sup>Ferroperm, Pz26,  $P_{max} = 10$  W/cm<sup>2</sup> of radiating surface,  $U_{max} = 200$  V<sub>AC</sub>/mm

<sup>66</sup>Schott AG Advanced Optics, ZERODUR®, expansion class: 0

<sup>67</sup> $\alpha(0\text{ }^\circ\text{C} - 50\text{ }^\circ\text{C}) = 0 \pm 0.020 \times 10^{-6}$  K<sup>-1</sup>

<sup>68</sup>Thorlabs GmbH, WG11050, AR coated for 650–1050 nm or 350–700 nm, respectively.

acteristic optical cavity parameters are illustrated in figure 4.32 and table 4.6.



reflectivity of mirrors M1, M2	99%
ROC (M2)	-250 mm
Cavity length $L_{cav}$	100 mm
finesse $\mathcal{F}$	313
FSR	1.5 GHz
FWHM	4.8 MHz

**Figure 4.32 & Table 4.6:** Optical Cavity parameters.

A small fraction of the laser light emitted by the ECDL is coupled into the cavity. A customized CCD camera<sup>69</sup> is used to monitor the transmitted signal of the cavity modes while a photodiode (PD)<sup>70</sup> provides monitoring of the back reflection from the cavity.

Frequency stabilization is accomplished by means of PDH method as follows: A local oscillator (LO)<sup>71</sup> connected to the laser diode (LD) of the ECDL provides sideband modulation in the laser frequency spectrum. The obtained PD signal is mixed with the LO signal in order to generate an error signal. The error signal is fed into a PID regulator<sup>72</sup> with integrated low-pass filter (LP) which regulates the voltage at the piezo at the grating of the ECDL and the current

<sup>69</sup>Logitech, C525 HD webcam USB, objective removed by hand

<sup>70</sup>Thorlabs GmbH, PDA10A-EC - Si Fixed Gain Detector, 200–1100 nm, 150 MHz BW, 0.8 mm<sup>2</sup>

<sup>71</sup>Toptica, PDD 110/F, Fast Pound-Drever-Hall Detector Module, Integrated RF oscillator: 20 MHz, tunable from 12–35 MHz

<sup>72</sup>Toptica, PID 110, PID Regulator Module

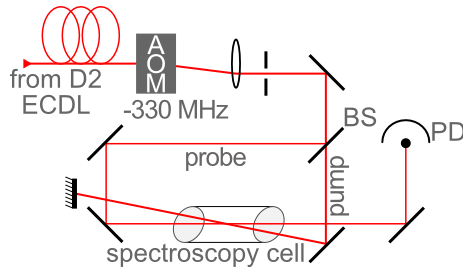


**Figure 4.33:** Frequency lock via saturated absorption spectroscopy.

at the LD in order to lock the ECDL.

The outer one of the two piezo rings is supplied with a static high voltage (HV)<sup>73</sup> in order to tune the resonance frequency of the cavity to the desired region of interest and to match the strong TEM<sub>00</sub> for locking. The inner piezo ring, supplied by an HV amplifier<sup>74</sup>, provides fine-tuning of the laser frequency during operation.

### Absorption spectroscopy

Part of the <sup>6</sup>Li D2 laser light, which is used for frequency stabilization via the optical reference cavity, is sent to a lithium spectroscopy vapor cell setup<sup>75</sup>, as shown in figure 4.33, to perform Doppler-free saturated absorption spectroscopy [123]. A detailed description of the process can be found in numerous publications as well as in my diploma thesis [62].

The error signal is obtained in almost the same manner as with the optical reference cavity (see above): By mixing the modulated spectroscopy signal of the weak probe beam with the LO signal a derivative signal is generated which is the error signal. The LO signal which is used for modulation and mixing is the same as for the frequency stabilization with the optical reference cavity. The error signal is used for stabilizing the resonance of the cavity to the spectroscopy signal. A tunable AOM<sup>76</sup> at -330 MHz compensates for the shift of the double-pass AOM at the D2 setup (see figure 4.28).

<sup>73</sup>ISEG Spezialelektronik, EBS 8030 504 SHV, Bipolar, 8 Channel,  $-3\text{ kV} \leq V_{\text{out}} \leq +3\text{ kV}$  and  $I_{\text{outnom}} = 0.5\text{ mA}$  per channel

<sup>74</sup>TEM Messtechnik GmbH, miniPiA 103, Piezo Amp, three channels, offset, gain, resonance filter

<sup>75</sup>Made available by Prof. Jook Walraven (UvA).

<sup>76</sup>Gooch and Housego, AOM 3350-125, 350 MHz, 470–850 nm, aperture: 1.5 mm

## 4.10 Optical access

Optical access for both, laser beams and imaging, was strongly emphasized when designing the setup. Optimal access is granted at two spatial locations at different horizontal levels as shown in figure 4.34.

1. The lower level is at the MOT mirror. The MOT is i.a. formed by two retroreflected circular polarized laser beams. The MOT mirror reflects one of these beams by  $90^\circ$  while the second beam path is orthogonally passing the mirror. The MOT is formed at the overlap of both beams and the reflected beam. An additional laser beam is the Zeeman slower beam, counterpropagating to the direction of the  ${}^6\text{Li}$  atom beam. To measure and optimize the loading rate of the MOT a collimated laser beam is used for absorption imaging.
2. The second location is at the center of the ion trap, where  $\text{Yb}^+$  ions are trapped, prepared and overlapped with  ${}^6\text{Li}$  atoms. The design of the trap allows for optical access:
  - In the direction of the trap axis through the end caps. This is utilized for the crossed optical dipole trap (see figure 4.30), for the first step of the two-step ionization of neutral  $\text{Yb}$  and for the repumper and re-repumper for  $\text{Yb}^+$ .
  - In the horizontal plane under an angle of  $45^\circ$  to the trap axis. All laser beams necessary to cool and manipulate  $\text{Yb}^+$  are coupled in here.
  - From the top and below. This is used for fluorescence- and absorption-imaging and might be useful to send in additional laser beams.

## 4.11 Imaging setup

A sketch of the setup for detecting the fluorescence signal of the  $\text{Yb}^+$  ions is shown in figure 4.35. The fluorescence light (1) is collected with an aspheric lens<sup>77</sup> (2) before being guided to the imaging systems using dielectric mirrors<sup>78</sup> (3) and (5). Here, a bandpass filter<sup>79</sup> (6) cleans the signal from stray light and a

<sup>77</sup>Thorlabs, AL4532-A,  $\varnothing 45$  mm S-LAH64 Aspheric Lens,  $f=32.0$  mm,  $\text{NA}=0.61$ , ARC: 350 – 700 nm

<sup>78</sup>Thorlabs, BB2-E02,  $\varnothing 2"$  Broadband Dielectric Mirror, 400 – 750 nm

<sup>79</sup>Thorlabs, FGUV11-UV,  $\varnothing 25$  mm UG11 Colored Glass Filter, AR Coated: 290 – 370 nm

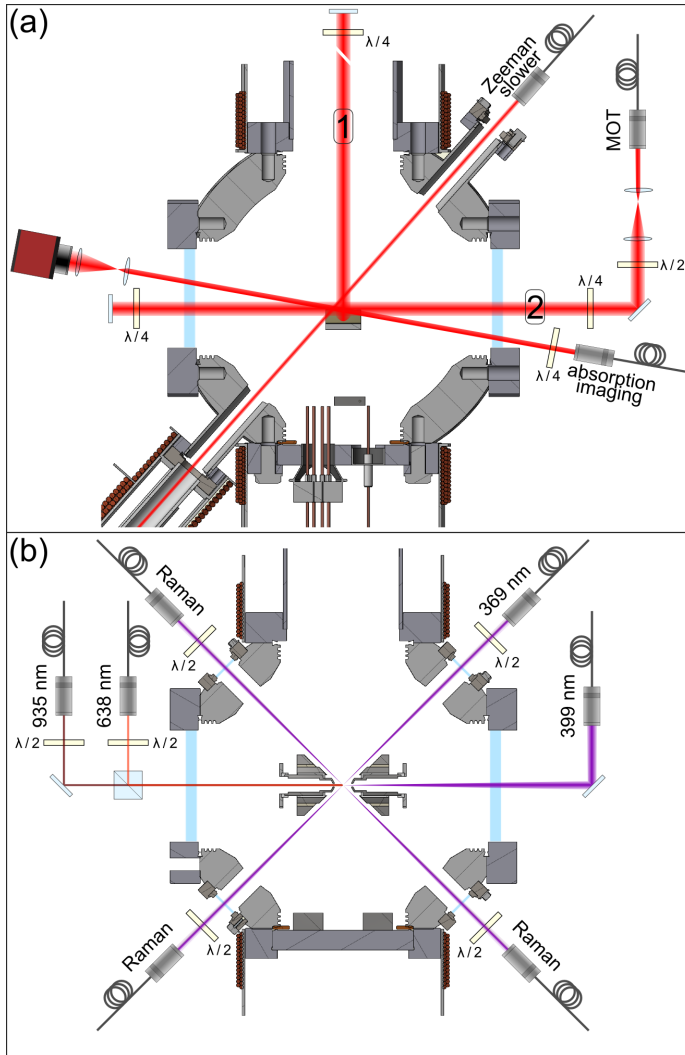


**Figure 4.34:** Sectional drawings of the experimental setup at the main chamber at two different horizontal levels in order to visualize the orientation of the laser beams and optical access. (a) Lower level: One of the two retro-reflected MOT beams (1) is additionally reflected at the in-vacuum mirror while the second beam (2) passes it in front. The Zeeman slower beam, pointing in the direction of the  ${}^6\text{Li}$  oven, passes the mirror under an angle of  $42^\circ$ . An additional beam is used for absorption imaging of the MOT. (b) Upper level: Horizontal cut through center of ion trap. Free apertures in the end caps provide laser access not only for the optical dipole trap but also for additional laser beams. All beams shown here serve for trapping, cooling and manipulating  $\text{Yb}^+$  ions.

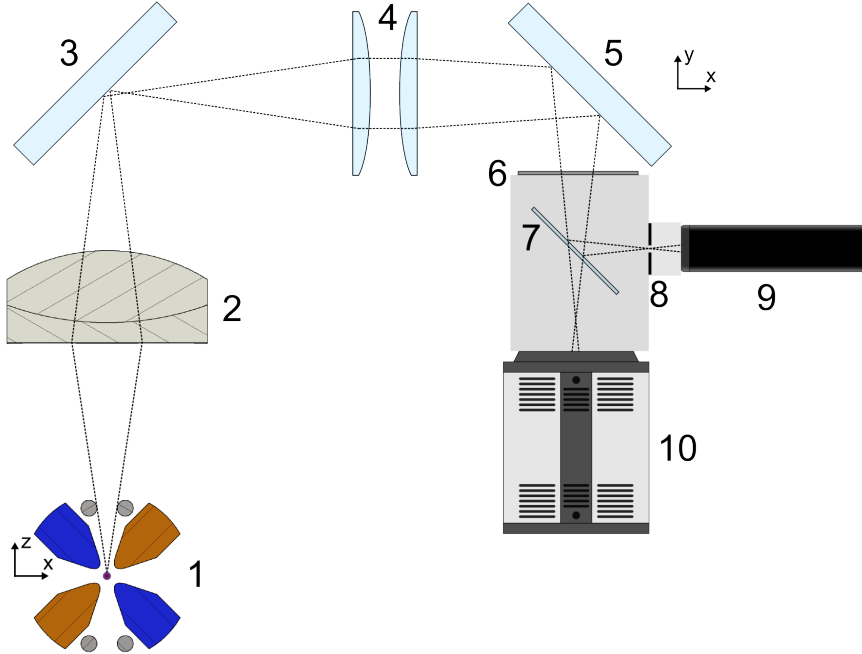


**Figure 4.35:** Sketch of imaging setup (not to scale).

beam splitter<sup>80</sup> (7) splits the signal in order to provide imaging with a camera<sup>81</sup> and with a Photomultiplier tube (PMT)<sup>82</sup>. An additional slit<sup>83</sup> (8) at the focal point of the signal for the PMT optimizes the signal-to-noise ratio. The two lenses<sup>84</sup> (4) collimate the light before creating an image at the two imaging planes.

We image the MOT via absorption imaging at the lower level as shown in figure 4.34 (a). For additional absorption imaging of the atomic cloud in the crossed ODT at the ion location the imaging system will be upgraded. For this

<sup>80</sup>Edmund optics, UV Plate Beamsplitter, 70R/30T 50mm Dia., Coating: BBAR ( $R_{\text{avg}} < 1\%$ ,  $R_{\text{abs}} < 2\%$  over 250 – 450 nm)

<sup>81</sup>Andor Zyla 5.5

<sup>82</sup>Sens-Tech, photodetector module P25PC-16

<sup>83</sup>OWIS, SP 40

<sup>84</sup>Thorlabs, LA1979-A, N-BK7 Plano-Convex Lens,  $\varnothing 50.8$  mm,  $f = 200.0$  mm, AR Coating: 350-700 nm

purpose the second mirror (5) will be replaced with a longpass dichroic mirror transmitting the absorption imaging beam and reflecting the fluorescence light of the ions, followed by an additional lens for collimating the laser beam and a camera<sup>85</sup>.

---

<sup>85</sup>The camera for absorption imaging is a Stingray F-033.



## 5 — Trapped ions

Experiments on hybrid atom-ion systems in the ultracold regime require full control over both constituents. Concerning the ions, state-of-the-art techniques need to be employed in order to coherently control their motional and internal states. In this chapter we explain the preparation of  $\text{Yb}^+$  ions in our setup and characterize the ion trap.

## 5.1 Introduction

Initializing  $\text{Yb}^+$  ions for the experiment involves the ionization, loading and cooling process (see section 4.9.1) as well as state preparation. In chapter 7 experiments are presented, where we study collisions between  ${}^6\text{Li}$  atoms and  $\text{Yb}^+$  ions. Those are conducted on several isotopes of  $\text{Yb}^+$  prepared in particular electronic states. The trapping behavior of the ion trap as well as first conclusions from simple trap frequency measurements are illustrated and discussed in section 5.2. In section 5.3 the ion trap is characterized and compared to the simulations from section 4.5. Here, the geometrical factors of the ion trap can be deduced from a set of measured radial and axial trap frequencies. The methods for state preparation and detection are presented in section 5.4. The  $\text{Yb}^+$  ions are initialized in the electronic ground state  ${}^2\text{S}_{1/2}$  or in one of the excited electronic states  ${}^2\text{P}_{1/2}$ ,  ${}^2\text{D}_{3/2}$  or  ${}^2\text{F}_{7/2}$ . With a nuclear spin of  $I = 1/2$  the isotope  ${}^{171}\text{Yb}^+$  can be prepared in a certain  ${}^2\text{S}_{1/2}$  hyperfine state. On the one hand, those hyperfine states are of particular interest for quantum information and quantum simulation experiments as pointed out in section 5.4.2. On the other hand they form a system which is ideally suited to measure state coherence as described in section 5.5.

A set of methods is applied in order to reduce the kinetic energy of the  $\text{Yb}^+$  ions by compensating for excess MM as explained in section 5.6. As a result we can tune the MM energy of the ions by deliberately adjusting the voltage at the compensation electrodes. This effect is exploited in the atom-ion collision measurements in chapter 7 in order to tune the collision energy.

## 5.2 Ion trapping

Neutral Yb atoms are ionized by isotope-selective two-step photoionization of neutral Yb atoms as explained in chapter 4.9.1. This technique provides a high loading efficiency of single ions allowing to precisely control the quantity of ions in a trapped ion crystal. Additionally, in the experiment the Yb oven is driven continuously with a small current to avoid fluctuations of the vacuum pressure while maintaining the pressure at a low level. This ensures constant and long lifetimes of the trapped ions and atoms.

The crystalline Yb in the oven (see chapter 4.4.3) is of natural abundance, allowing to choose between the isotopes. The particular resonance wavelengths of the single isotopes are determined by taking a laser-induced fluorescence spectrum of the  ${}^1\text{S}_0 \rightarrow {}^1\text{P}_1$  transition of neutral Yb as shown in figure 5.1. In order

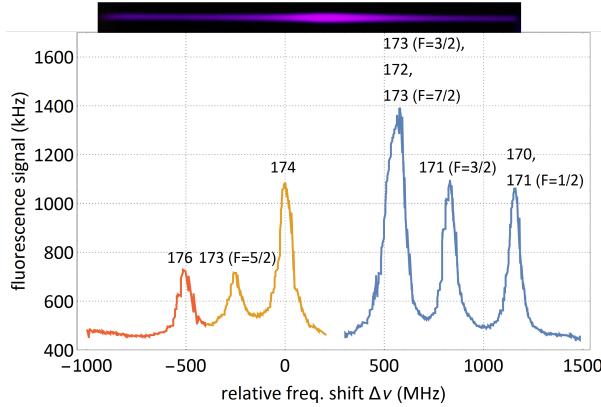


**Figure 5.1:** Laser-induced fluorescence spectrum of neutral Yb. The isotope shift for the  $^1S_0 \rightarrow ^1P_1$  transition is measured, with  $^{174}\text{Yb}$  as reference at  $\nu = 751.52622$  THz ( $\lambda = 398.91151$  nm). The spectrum is composed of three measurements (red / yellow / blue) due to limited mode-hop free range of the home-made ECDL. The particular isotopes are identified using Ref. [124]. The picture on top of the spectrum is a photograph of our first fluorescence measurement in a simple vacuum setup.

to preserve resonant loading of the desired isotopes, those spectra are taken regularly. For the measurement the  $\lambda = (370 \pm 2)$  nm bandpass filter at the objective of the imaging system is replaced with a  $\lambda = (395.0 \pm 5.5)$  nm bandpass filter<sup>1</sup>. The fluorescence spectrum is taken by scanning the wavelength of the home-made  $\lambda = 398.9$  nm ECDL. Additionally, the Yb oven is operated at a higher current ( $I_{\text{Yb-oven}} = 3\text{--}4$  A) than during normal operation to increase the flux, improving the signal-to-noise ratio. As has been pointed out in chapter 4.9.1, the laser beam orientation is perpendicular to the oven to avoid first order Doppler broadening. By comparing the relative frequency shifts of the peaks in the spectrum with the isotope shifts given in table A.3 [124], the particular isotopes can be identified. We note, that for the transitions of  $^{170}\text{Yb}^+$  and  $^{172}\text{Yb}^+$  there is significant overlap with transitions of other isotopes near-by, such that these isotopes are harder to load deterministically.

A set of pictures of trapped  $^{174}\text{Yb}^+$  ions is shown in figure 5.2. With a stable background gas pressure of  $p \leq 10^{-10}$  mbar the lifetime of the trapped ions in the trap could not be measured as complete losses are rare. Background

<sup>1</sup>Semrock, FF01-395/11-25, BrightLine single-band bandpass filter, center wavelength: 395 nm, guaranteed minimum bandwidth: 11 nm.

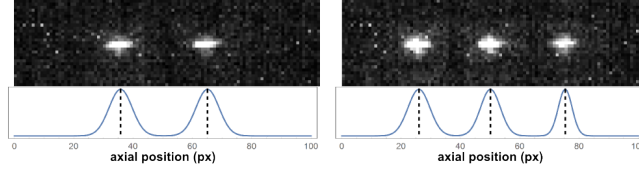


**Figure 5.2:** Pictures of trapped  $^{174}\text{Yb}^+$  ions in our ion trap. The setup allows to load single or multiple  $\text{Yb}^+$  ions of selected isotope and quantity. The axial positions of the single ions are determined by fitting a Gaussian distribution to the camera picture. Each picture is an average of ten images in order to determine the ion positions in the crystals with increased precision.

gas collisions with electronically excited ions<sup>2</sup> may lead to population of the  $^2\text{F}_{7/2}$  state which can be observed as single ions in a crystal turn dark while the positions of the ions in the crystal remain unchanged. Here, the re-pumper (see chapter 4.9.1) returns the ions back into the cooling cycle.

The inter-ion distance as marked in the fits in figure 5.2 can be determined following Ref. [125]. The inter-ion spacing  $\Delta d(N)$  in a crystal with  $N$  ions is given by

$$\Delta d(N) = 2 \left( \frac{Q^2}{4\pi\epsilon_0 m_{\text{ion}} \omega_{\text{ax}}^2} \right)^{\frac{1}{3}} \Delta u(N) \quad , \quad (5.1)$$

with  $\Delta u(2) = -2(1/2)^{2/3}$ ,  $\Delta u(3) = -2(5/4)^{1/3}$  and  $\omega_{\text{ax}}$  the axial trap frequency which is the only variable which has to be measured. The principle of trap frequency measurements is to drive the harmonic oscillation of trapped ions by an externally applied sinusoidal driving force of strength  $F_0$  and frequency  $\omega_{\text{ext}}$ . By scanning  $\omega_{\text{ext}}$  over the resonance frequency of the ions the amplitude of their harmonic oscillation rapidly grows which can be observed as a change in their fluorescence level [126]. The additional driving frequency is generated by a signal generator<sup>3</sup> with tunable frequency and amplitude. It is applied to the system via one of the end caps or via one of the compensation electrodes to drive the axial or radial oscillation, respectively. The frequency is scanned stepwise while the ions are continuously cooled and their fluorescence is observed. If on resonance, the ions blur and for high amplitudes the ion crystal completely melts. This can also be observed as a drop of fluorescence signal at the PMT.

<sup>2</sup>As during the laser cooling cycle.

<sup>3</sup>Hewlett Packard, 3310A Function Generator, frequency range 0.0005 Hz to 5 MHz, max. output level 30 V<sub>p-p</sub>

By reducing the amplitude, the effect gets weaker while the respective trap frequency can be determined with increasing accuracy.

For the ion crystals in figure 5.2 we measured an axial trap frequency of  $\omega_{\text{ax}} = 2\pi \times 40.9(1)$  kHz yielding inter-ion distances of  $\Delta d_{\text{min}}(2) = 28.92(2)$   $\mu\text{m}$  and  $\Delta d_{\text{min}}(3) = 24.73(2)$   $\mu\text{m}$ . Those can be related to the inter-ion distances we get from the Gaussian fits in the camera pictures and thus obtain the magnification of the imaging system<sup>4</sup>  $M_{\text{Imaging}} = 6.5(1)$ .

### 5.3 Ion trap characterization

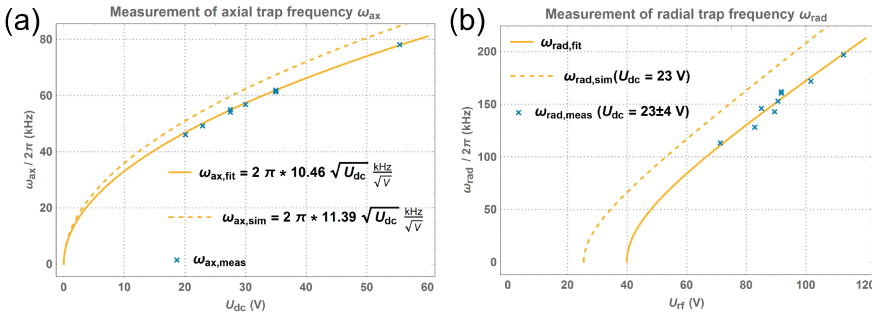


**Figure 5.3:** Trap frequency measurements: (a) Axial trap frequency  $\omega_z/2\pi$  to end cap voltage  $U_{\text{dc}}$ . (b) Radial trap frequency  $\omega_{\text{rad}}/2\pi$  to rf amplitude  $U_{\text{rf}}$ .

In order to characterize the ion trap, we measured the axial and radial ion trap frequencies  $\omega_{\text{ax}}$  and  $\omega_{\text{rad}}$  as a function of the applied voltages. The results of those measurements are shown in figure 5.3. In principle, the analysis of those measurements is similar to the procedure in chapter 4.5 and the geometrical factors could be estimated from the fits in figure 5.3. However, as the trap parameters ( $U_{\text{dc}}$ ,  $U_{\text{rf}}$  and  $\Omega$ ) slightly vary between single measurements a more precise approach is to evaluate the corresponding  $a$  and  $q$  parameters as they are proportional to  $U_{\text{dc}}/\Omega^2$  and  $U_{\text{rf}}/\Omega^2$ , respectively. They are plotted in figure 5.4. From the fits the geometrical factors are found to be:

$$\begin{aligned} \kappa_{\text{ax,meas}} &= 0.097 \pm 0.001 & (\kappa_{\text{ax,sim}} &= 0.115, \text{ rel. dev.: } 15.7\%) \\ \kappa'_{\text{rad,meas}} &= 0.797 \pm 0.048 & (\kappa'_{\text{rad,sim}} &= 0.974 \text{ rel. dev.: } 18.1\%) \end{aligned}$$

These values are in rough agreement with the simulations in chapter 4.5.

<sup>4</sup>The pixel size of the CMOS chip in the camera system (Andor, Zyla 5.5) is  $6.5 \times 6.5$   $\mu\text{m}^2$ .

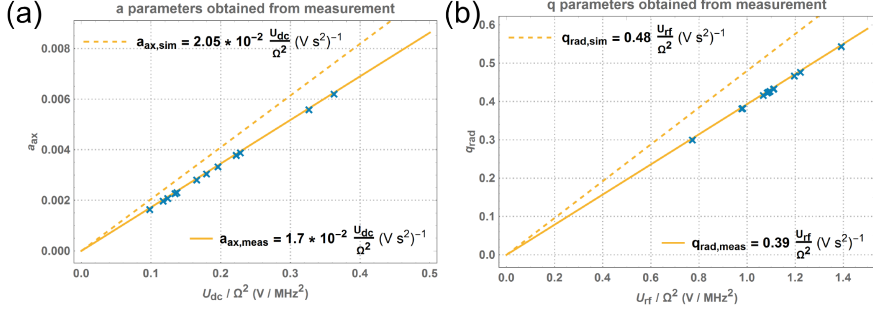


**Figure 5.4:** (a)  $a$  and (b)  $q$  parameters obtained from measurement in comparison to simulation.

## ${}^6\text{Li}^+$

In chapter 7 we examine inelastic collisions between  ${}^6\text{Li}$  atoms and  $\text{Yb}^+$  ions. Here, a possible chemical process is charge transfer ( $\text{Li} + \text{Yb}^+ \rightarrow \text{Li}^+ + \text{Yb}$ ). This gives rise to the question if also  ${}^6\text{Li}^+$  ions would be trapped in the ion trap.

With the geometrical factors calculated above, the stability parameters  $a$  and  $q$  for  ${}^6\text{Li}^+$  are  $a_{\text{ax}} = 0.05$  and  $q_{\text{rad}} = 5.4$ , with  $\Omega = 2\pi \times 2 \text{ MHz}$ ,  $U_{\text{dc}} = 15 \text{ V}$  and  $U_{\text{rf}} = 75 \text{ V}$ . These values are far off the first stability region and thus  ${}^6\text{Li}^+$  ions will be expelled from the trap as also our simulations show.

## 5.4 State preparation and state detection

The atom-ion collision experiments presented in chapter 7 are performed on several isotopes of  $\text{Yb}^+$ . The ions are initially prepared in the  ${}^2\text{S}_{1/2}$  ground state as well as in the excited electronic states  ${}^2\text{P}_{1/2}$ ,  ${}^2\text{D}_{3/2}$  and  ${}^2\text{F}_{7/2}$ . The isotope  ${}^{171}\text{Yb}^+$ , which has a nuclear spin  $I = 1/2$  is initially prepared in the  ${}^2\text{S}_{1/2} |F = 0\rangle$  hyperfine ground state.

### 5.4.1 Electronic state preparation

State preparation is always initiated with Doppler cooling on the  ${}^2\text{S}_{1/2} \rightarrow {}^2\text{P}_{1/2}$   $D1$  transition while continuously pumping the  ${}^2\text{D}_{3/2} \rightarrow {}^2\text{D}[3/2]_{1/2}$  repumper transition (see chapter 4.9.1), followed by an individual sequence depending on the state of choice as illustrated in figure 5.5.

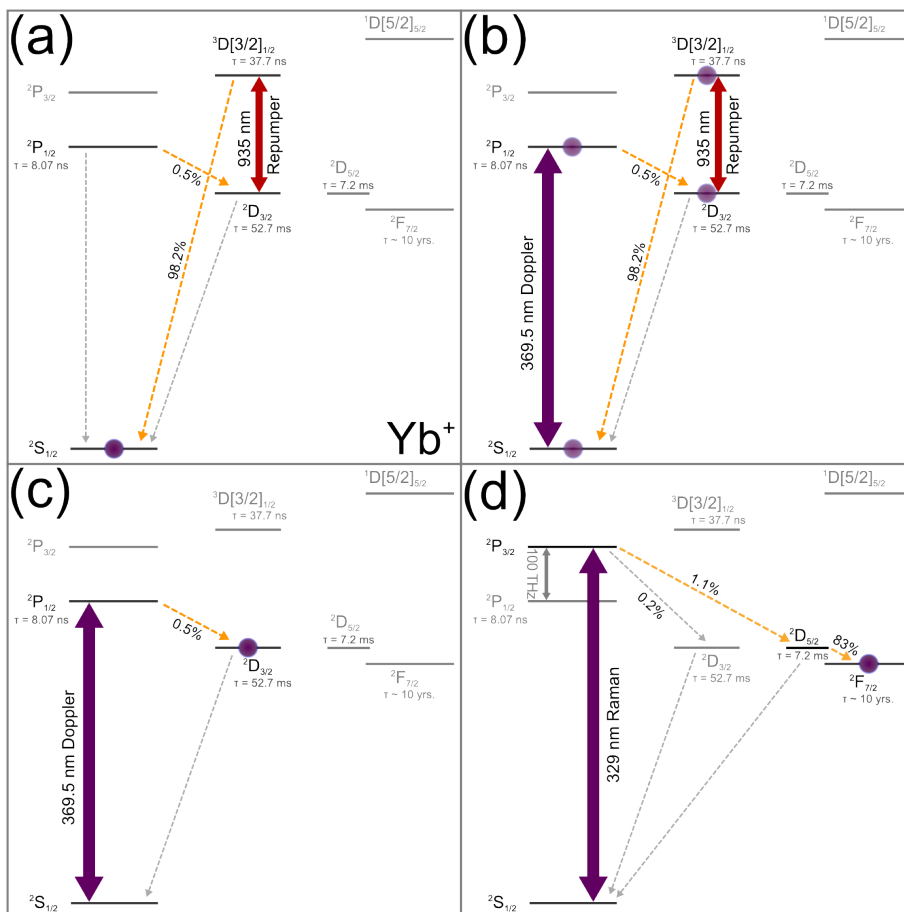


**Figure 5.5:** Principle of state preparation for  $\text{Yb}^+$  isotopes without nuclear spin. Preparation of the (a)  $^2\text{S}_{1/2}$  ground state. (b)  $^2\text{P}_{1/2}$  excited state. (c)  $^2\text{D}_{3/2}$  excited state. (d)  $^2\text{F}_{7/2}$  excited state.

(a) The  $^2S_{1/2}$  ground state is prepared by switching off the 369 nm Doppler cooling beam. Thus, an ion in the  $^2P_{1/2}$  state may spontaneously decay to the  $^2S_{1/2}$  ground state or, with a branching ratio of  $\approx 1/200$ , to the  $^2D_{3/2}$  state. In that case the continuously running 935 nm Repumper beam pumps the ion to the  $^2D[3/2]_{1/2}$  state which rapidly decays to the  $^2S_{1/2}$  ground state.

(b) Due to its short lifetime of  $\tau_P = 8.07$  ns the  $^2P_{1/2}$  state cannot be prepared as a pure state, but only a fraction of the population is in the  $^2P_{1/2}$  state during Doppler cooling. In Ref. [34] a method is presented to experimentally measure the  $^2P_{1/2}$  state population fraction  $p(^2P_{1/2}) = \tau_P/\tau_c$  during Doppler cooling. Here,  $\tau_c$  is the average time between two spontaneous decays from the  $^2P_{1/2}$  state to the  $^2D_{3/2}$  state and  $\tau_P = 200/\Gamma_P$  is the average time the ion is in the  $^2P_{1/2}$  state during  $\tau_c$ . It is given by the probability for spontaneous decays from the  $^2P_{1/2}$  state to the  $^2D_{3/2}$  state ( $\approx 1/200$ ) and the natural linewidth of the  $^2P_{1/2}$  state  $\Gamma_P = 2\pi \times 19.7(2)$  MHz. We measure the  $^2P_{1/2}$  state population fraction to be  $p(^2P_{1/2}) = 0.26(5)$ .

(c) In order to effectively populate the  $^2D_{3/2}$  state, the 935 nm repumper beam is turned off while constantly driving the  $^2S_{1/2} \rightarrow ^2P_{1/2}$  Doppler cooling transition.

(d) To prepare the  $^2F_{7/2}$  state, we use the frequency-quadrupled ECDL at 329 nm to drive the  $^2S_{1/2} \rightarrow ^2P_{3/2}$   $D2$  transition. From state  $^2P_{3/2}$  the ion can cascade to the  $^2F_{7/2}$  state. Since this process relies on the decay of the  $^2D_{5/2}$  state, which has a lifetime of 7.2 ms [127], the required preparation time is much longer than for the other states which has to be considered in the experimental sequence. Successful state preparation is checked by observing no fluorescence when driving the Doppler and repumper transition.

#### 5.4.2 Spin preparation and spin detection in $^{171}\text{Yb}^+$

Over the last few years, a host of possible applications for hybrid atom-ion systems have been put forward aiming at, e.g., probing atomic systems with ions [42] or to use the system for quantum computation [31, 43] and quantum simulation [32]. These applications require an accurate control over the spin of the ion or the availability of two energy levels that may be employed as a long-lived qubit. In  $\text{Yb}^+$ , the isotope  $^{171}\text{Yb}^+$  is used in quantum information and simulation experiments [128, 129]. Due to its nuclear spin of  $I = 1/2$ , it

has a simple hyperfine structure which features a 12.64 GHz transition [130] between the  $^2S_{1/2}$  ground hyperfine states  $|F = 0, m_F = 0\rangle \rightarrow |F = 1, m_F = 0\rangle$ , as shown in figure 5.6. Since the transition frequency is insensitive to magnetic field noise in first order, this represents an excellent qubit [128, 131, 132]. In this section we describe the preparation procedure of the  $^{171}\text{Yb}^+$  hyperfine states in our experimental setup.

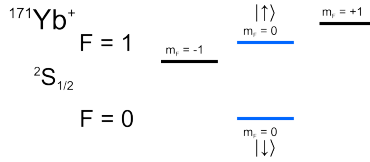


**Figure 5.6:** Hyperfine splitting of the  $^2S_{1/2}$  ground state in  $^{171}\text{Yb}^+$ . The states  $|\uparrow\rangle$  and  $|\downarrow\rangle$  form the spin qubit.

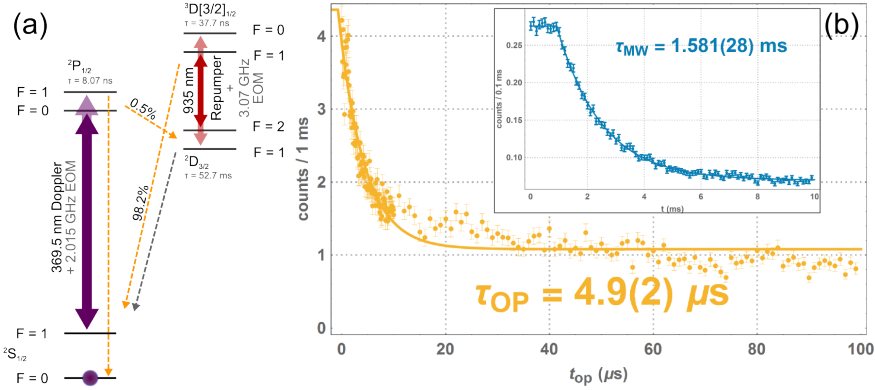


**Figure 5.7:** (a) Initialization scheme of the  $^2S_{1/2} |F = 0\rangle$  ground hyperfine state in  $^{171}\text{Yb}^+$  (see text). (b) Experimental preparation of the  $^{171}\text{Yb}^+ ^2S_{1/2} |F = 0\rangle$  ground hyperfine state. (blue) By switching off the  $f_{\text{MW}} = 12.64$  GHz MW off-resonant coupling to the  $^2P_{1/2} |F = 1\rangle$  state leads to population of the  $^2S_{1/2} |F = 0\rangle$  state. Each point was averaged over 10 000 measurements. (yellow) Optical pumping via the  $^2P_{1/2} |F = 1\rangle$  state significantly reduces the exponential decay time by a factor of  $10^3$ . Each point was averaged over 200 measurements.

In order to initialize  $|\downarrow\rangle$  after Doppler cooling, the  $f_{\text{MW}} = 12.64$  GHz MW is turned off while the cooling laser is phase modulated at 2.105 GHz (see chap-

ter 4.9.1). A scheme of this process is shown in figure 5.7 (a). The frequency modulation leads to optical pumping into the  ${}^2P_{1/2} |F = 1\rangle$  state which decays to  $|\downarrow\rangle$ . Experimental results on the population efficiency of  $|\downarrow\rangle$  with and without optical pumping are compared in figure 5.7 (b). These measurements were performed on a Doppler cooled  ${}^{171}\text{Yb}^+$  two-ion crystal. For the off-resonant population transfer measurement, only the  $f_{\text{MW}} = 12.64$  GHz MW is turned off, while optical pumping is achieved by simultaneously switching on the EOM for a certain time  $t$ , followed by state detection for 1 ms.

The hyperfine state is determined by scattering photons on the closed  ${}^2S_{1/2} |F = 1\rangle \rightarrow {}^2P_{1/2} |F = 0\rangle$  transition. When the ion is in  $|F = 0\rangle$ , it scatters no photons and we identify a dark ion with this state. Subsequent optical pumping and fluorescence detection during Doppler cooling allow us to distinguish the *dark* state  $|F = 0\rangle$  from ion loss.

Without optical pumping the exponential decay time from  $|F = 1\rangle$  to  $|F = 0\rangle$ , due to off-resonant coupling of the Doppler cooling beam to  ${}^2P_{1/2} |F = 1\rangle$ , is  $\tau_{\text{MW}} = 1.581(28)$  ms. With optical pumping it is reduced to  $\tau_{\text{OP}} = 4.9(2)$   $\mu\text{s}$ , thus ensuring fast hyperfine state initialization.

After preparing the state  $|\downarrow\rangle$ , the ions can be prepared in a particular  ${}^2S_{1/2} |F = 1, m_F\rangle$  state with MW  $\pi$ -pulses resonant on the  $|\downarrow\rangle \rightarrow |F = 1, m_F\rangle$  transition as shown in figure 5.8 (a). In order to characterize the Zeeman splitting of the  $|F = 1, m_F = \pm 1\rangle$  hyperfine sub-states, spectra were measured as shown in figure 5.8 (b). Here, the yellow colored spectrum with the MW and Doppler beam constantly running features much broader peaks which are shifted to the red by  $\sim 1$  MHz with respect to the blue colored spectrum where the MW pulses were applied after turning off the Doppler cooling beam. The blue colored spectrum exhibits small, broad peaks shifted to the red which may result from leaking Doppler light during the MW pulse.

## 5.5 Coherence time of the spin qubit

Coherent control over the  $\text{Yb}^+$  ion's motional and spin states is crucial in order to perform experiments on the atom-ion system in the quantum regime. Main limiting factors may be magnetic field noise due to varying current in the magnetic field coils as well as fluctuations of laser or MW frequency and power. The hyperfine states of the  ${}^2S_{1/2}$  ground state in  ${}^{171}\text{Yb}^+$  provide a highly sensitive system in order to characterize and optimize the experimental setup. For instance, magnetic field noise leads to fluctuations of the Zeeman split  ${}^2S_{1/2} |F = 1, m_F = \pm 1\rangle$  energy levels leading to phase fluctuations and conse-

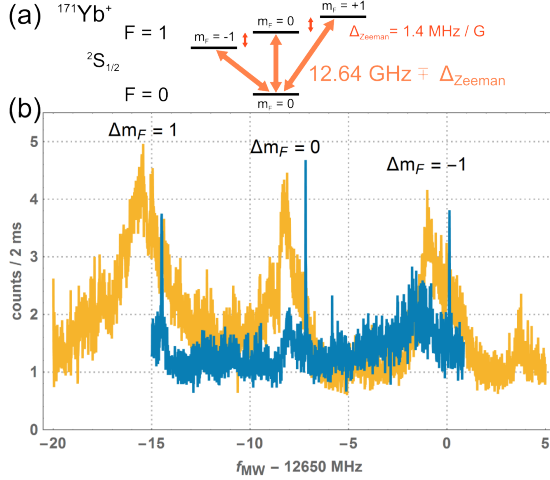


**Figure 5.8:** (a) A particular  ${}^2S_{1/2} |F=0, m_F=0\rangle \rightarrow {}^2S_{1/2} |F=1, m_F\rangle$  transition can be driven by applying a MW  $\pi$ -pulse of frequency  $f_{MW} = 12.64 \text{ GHz} \pm \Delta_{\text{Zeeman}}$ , with  $\Delta_{\text{Zeeman}}$  the Zeeman splitting of the  $|F=1, m_F = \pm 1\rangle$  hyperfine sub-states. (b) MW spectrum of Zeeman split  ${}^2S_{1/2} |F=1, m_F\rangle$  hyperfine sub-states with  $B \approx 5 \text{ G}$ . For both spectra the ion was initially prepared in the  ${}^2S_{1/2} |F=0\rangle$  ground hyperfine state by  $100 \mu\text{s}$  optical pumping. To obtain the blue spectrum the Doppler beam was turned off after the initialization followed by a 3 ms MW pulse with frequency  $f_{MW} = 12.64 \text{ GHz} \pm \delta f$  and 2 ms state-selective fluorescence detection. For the yellow spectrum the MW and Doppler cooling beam were running continuously while scanning the MW frequency. For both spectra the frequency was scanned in steps of 10 kHz.

quently to decoherence. This sets an upper limit for the duration of experiments that rely on spin coherence.

When exposed to MW radiation near-resonant to a  ${}^2S_{1/2}$  ground state  $|F=0, m_F=0\rangle \rightarrow |F=1, m_F\rangle$  transition, the state population oscillates back and forth between the respective lower and upper levels. This well-known behavior is called *Rabi flopping* and the probability for finding the ion in state  $|\downarrow\rangle$  is given by [133]

$$|p_{|\downarrow\rangle}(t)|^2 = \frac{\Omega_0^2}{\Omega^2} \sin^2\left(\frac{\Omega t}{2}\right) \quad \text{with} \quad \Omega^2 = \Omega_0^2 + \Delta^2. \quad (5.2)$$

Here,  $\Omega_0$  is the Rabi frequency and  $\Delta$  is the detuning from resonance. Rabi flop measurements are suited to make first qualitative predictions on the co-

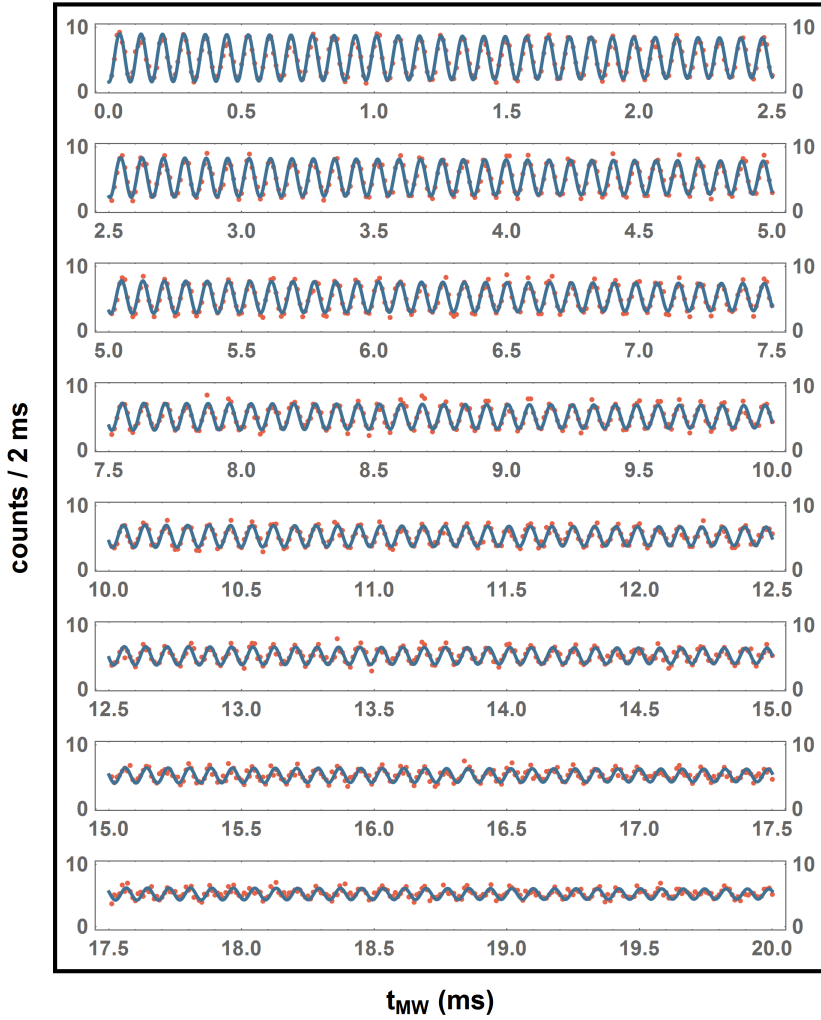


**Figure 5.9:** MW Rabi oscillations on the carrier qubit clock transition. For the measurement, taken with a two-ion crystal, the MW pulse length  $t_{\text{MW}}$  was scanned in steps of  $10\ \mu\text{s}$  followed by 2 ms state detection. The Rabi frequency, extracted from the fit, is  $\Omega_0 = 12.3825(1)\ \text{kHz}$  and the state population has a coherence time of  $t_{\text{coh.}} = 13.1(3)\ \text{ms}$ . Each point was averaged over 85 measurements.

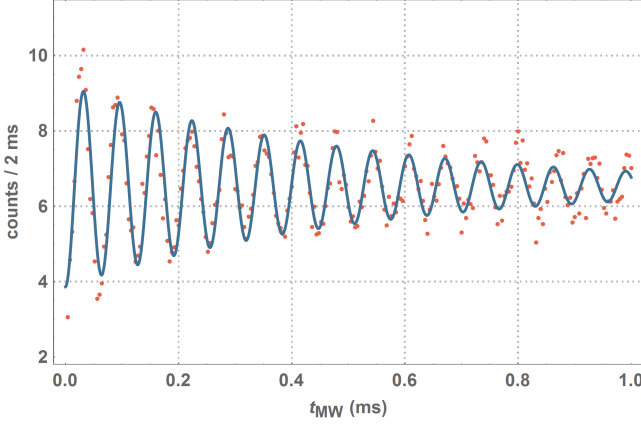


**Figure 5.10:** MW Rabi oscillations on the ground state  $|F = 0, m_F = 0\rangle \rightarrow |F = 1, m_F = -1\rangle$  transition. For the measurement, taken with a three-ion crystal, the MW pulse length  $t_{\text{MW}}$  was scanned in steps of  $10 \mu\text{s}$  followed by 2 ms state detection. The  $y$ -axis shows the number of photons detected during a 2 ms state-detection pulse. The Rabi frequency, extracted from the fit, is  $\Omega_0 = 15.65(1)$  kHz and the state population has a coherence time of  $t_{\text{coh.}} = 0.52(4)$  ms. Each point was averaged over 250 measurements.

herence time  $t_{\text{coh.}}$  of the particular populated quantum states. Figures 5.9 and 5.10 show Rabi oscillations measured on the  ${}^2\text{S}_{1/2}$  qubit transition  $|\downarrow\rangle \rightarrow |\uparrow\rangle$  and  $|F = 0, m_F = 0\rangle \rightarrow |F = 1, m_F = -1\rangle$  transition, respectively. Those were taken shortly after setting up the system and before further optimizations were realized as explained in section 5.6 and in Ref. [104]. For the measurement the  ${}^{171}\text{Yb}^+$  ion crystal is prepared in the  $|\downarrow\rangle$  state via  $100 \mu\text{s}$  optical pumping as explained in the previous section before being exposed to MW radiation for a certain time  $t_{\text{MW}}$  followed by 2 ms state detection. For both measurements the pulse time  $t_{\text{MW}}$  was scanned in steps of  $10 \mu\text{s}$ . Both measurements show a damped oscillation. This damping which governs the state decoherence results from dephasing processes which can have various causes [133]. The coherence time  $t_{\text{coh.}}$  can be extracted from the envelope of the fits to the decreasing amplitude which is proportional to  $\exp[-t_{\text{MW}}/t_{\text{coh.}}]$ . Here, the coherence time of the magnetic field insensitive qubit transition compared to the  $|0, 0\rangle \rightarrow |1, -1\rangle$  transition is longer by a factor of about 25.

An accurate characterization of state coherence is achieved via the *Ramsey*

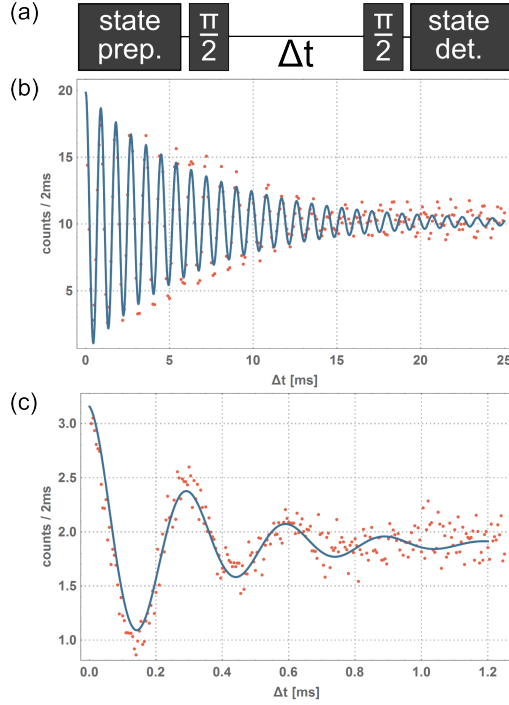


**Figure 5.11:** Ramsey interferometry measurement. (a) Sequence: After state preparation via  $100 \mu\text{s}$  optical pumping a  $\pi/2$ -pulse is applied on the transition such that the ion state is in a coherent superposition of both states. After the delay time  $\Delta t$  a second  $\pi/2$ -pulse is applied followed by state detection. By setting the pulses slightly off-resonant to the transition (with  $\Omega \gg \Delta$ ), the spin superposition acquires a phase difference as compared to the MW, which becomes visible as Ramsey fringes as a function of delay time  $\Delta t$ . (b) Ramsey measurement on the carrier qubit clock transition with a three-ion crystal. For this measurement the MW frequency was set to  $\nu_{\text{MW}} = 12.642814 \text{ GHz}$  yielding a Rabi frequency of  $\Omega_0 = 12.11 \text{ kHz}$  and a  $\pi/2$ -pulse time of  $t_{\pi/2} = 20.65 \mu\text{s}$ . The state population has a coherence time of  $t_{\text{coh.}} = 6.9(3) \text{ ms}$  which is of the same order as in the Rabi measurement. Each point was averaged over 250 measurements. (c) Ramsey measurement on the ground state  $|F = 0, m_F = 0\rangle \rightarrow |F = 1, m_F = 1\rangle$  transition with a single ion. For this measurement the MW frequency was set to  $\nu_{\text{MW}} = 12.635415 \text{ GHz}$  yielding a Rabi frequency of  $\Omega_0 = 20.15 \text{ kHz}$  and a  $\pi/2$ -pulse time of  $t_{\pi/2} = 12.41 \mu\text{s}$ . The state population has a coherence time of  $t_{\text{coh.}} = 0.31(2) \text{ ms}$  which is also of the same order as in the Rabi measurement. Each point was averaged over 250 measurements.

*method* [134]. A scheme of the process is given in figure 5.11 (a). After  $|\downarrow\rangle$  state initialization a MW  $\pi/2$ -pulse is applied – e.g. on the spin qubit transition – leading to the coherent superposition state  $(|\downarrow\rangle - i|\uparrow\rangle)/\sqrt{2}$ . By slightly detuning the pulse from resonance, the atomic state acquires a small phase evolution with respect to the MW field:  $(|\downarrow\rangle - \exp(i\varphi)|\uparrow\rangle)/\sqrt{2}$ . A second MW  $\pi/2$ -pulse is applied projecting the phase into the populations of the atomic states  $|\uparrow\rangle$  or  $|\downarrow\rangle$  followed by state detection. As a result, the detected state oscillates between  $|\uparrow\rangle$  and  $|\downarrow\rangle$  as a function of delay time  $\Delta t$ . Decoherence due to e.g. magnetic field noise reduces the contrast of these oscillations, allowing us to obtain the coherence time.

In the figures 5.11 (b) and (c) Ramsey measurements are shown for the  ${}^2\text{S}_{1/2}$  spin qubit transition and  $|0,0\rangle \rightarrow |1,1\rangle$  transition, respectively. Those were measured during the same measurement run as the Rabi flops above before optimizing the setup. From the fits we obtain coherence times which are shorter but of the same order as those obtained from the Rabi flop measurement.

We suspect that residual magnetic field noise is the main limitation in the coherence time. Note that, although the  $|0,0\rangle \rightarrow |1,0\rangle$  transition is magnetic field insensitive in first order, it does experience a quadratic Zeeman shift at low fields. Since we cannot operate at zero magnetic field, as coherent population trapping would prevent the ion from scattering light, the qubit always experiences an amount of magnetic field noise.

## 5.6 Micromotion compensation

In a Paul trap, the motion of an ion is composed of a secular motion of radial and axial frequencies  $\omega_{\text{rad/ax}}$  in the harmonic pseudopotential, and a superimposed, driven oscillation at the trap drive frequency  $\Omega$  referred to as micromotion (MM) (see chapter 2.3.1). Ideally, the motion in the axial direction of the trap is purely secular while in radial direction the MM causes more complex dynamics. The kinetic energy of the ion is given by [76]

$$E_{\text{yb},i} = E_{\text{therm},i} + E_{\text{MM},i} \quad (5.3)$$

with

$$E_{\text{therm},i} = \frac{1}{2}k_B T_i \cong \frac{1}{4}m_{\text{ion}}u_i^2\omega_i^2. \quad (5.4)$$

Here,  $u_i$  is the amplitude of the ion's secular motion in direction  $i = (\text{rad}, \text{ax})$  and  $E_{\text{MM},ax} = 0$ .

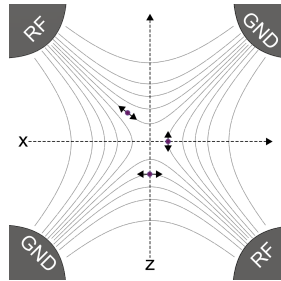


**Figure 5.12:** Sectional drawing of the ion trap in the radial  $x$ - $z$ -plane. If shifted off the nodal center of the rf potential, an ion performs MM along the rf quadrupole field lines (gray) with increased amplitude.

However, as mentioned in chapter 3.5.2 there might be imperfections in the experimental setup causing a dc electric field at the rf trap minimum  $\mathbf{E}_{dc}$ . This may originate from several sources, e.g. surface contaminations on the trap electrodes with dipolar impurity atoms, insufficient shielding of external stray fields, etc. The additional field  $\mathbf{E}_{dc}$  shifts the ion out of the nodal position of the quadrupole rf field causing additional MM in radial or axial direction which is called *excess* MM (see figure 5.12). Yet another reason for excess MM is a possible phase shift between the voltage signals at both rf blades leading to additional MM along the axis between those. Like the inherent MM it is a non-thermal, driven motion which adds to the kinetic energy and cannot be reduced by cooling techniques.

In order to minimize the kinetic energy of the ion it is essential to compensate for excess MM. Additionally, as MM causes disadvantageous side effects as transition line broadening, a low amplitude MM is favorable in order to allow for, e.g., effective Doppler cooling and precision spectroscopy.

Several precautions were taken in advance in order to cope with excess MM in our experiment presented in chapter 4.4. For example, both, the self-supporting design of the blade electrodes ensuring high precision of the alignment and a single electrical connection exactly at the center between both electrodes prevent possible phase shifts. Furthermore, four compensation electrodes and independently connected end cap electrodes allow for shifting the ion's average position in all three dimensions.

We employ microwave sideband spectroscopy on a single  $^{171}\text{Yb}^+$  ion [135, 136] and infer an ion temperature of about 4 mK after Doppler cooling and a heating rate of  $\leq 4$  mK/second. The excess MM, caused by a displacement of the ion out of the node of the dynamic electric quadrupole potential, can easily take values up to several Kelvin if not compensated carefully. We use a set of complementary methods in order to compensate for axial and radial excess MM

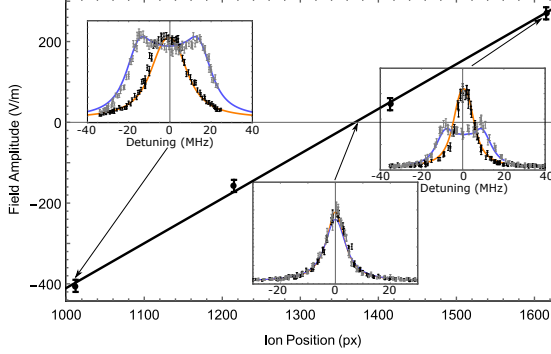


**Figure 5.13:** Oscillating electric field amplitude at 225 V trap drive amplitude in dependence to the axial ion position. The zero crossing corresponds to the position of minimal axial MM. At this position, the end cap voltages for axial confinement are 15 V and 15.4 V, respectively. The insets show the linewidth measurement and fitted at three positions. Far away from the center, the transition is clearly broadened at 225 V trap drive amplitude (blue) compared to the measurement at 67 V amplitude (orange). At the center, both measurements show similar broadening.

in our setup which are described in this section.

### 5.6.1 Axial micromotion compensation

The MM of an  $^{174}\text{Yb}^+$  ion along the axial  $y$ -direction of the ion trap is determined by observing the MM-induced line broadening of the  $^2D_{3/2} \rightarrow ^3D[3/2]_{1/2}$  repumper transition at 935 nm wavelength with a laser beam aligned parallel to the trap axis in dependence to the axial position of the ion. To avoid saturation broadening, the laser power is reduced as much as possible. Still, the transition may be broadened by thermal motion of the ion, laser linewidth and the Zeeman splitting in a magnetic field yielding a linewidth of  $\Gamma_0 > \Gamma_{\text{nat}}$ . Taking these effects into account, the line shape is given by [76]

$$\Gamma_{\text{MM}}(\Delta) = b \sum J_n(\beta_{\text{MM}})^2 \frac{\Gamma_0^2}{(\Delta - n\Omega)^2 + \Gamma_0^2}. \quad (5.5)$$

Here,  $b$  is a constant,  $J_n$  is the  $n$ th Bessel function,  $\beta_{\text{MM}} = k \cdot u_{\text{MM}}$  is the modulation index due to the MM amplitude  $u_{\text{MM}}$  and  $\Delta$  the laser detuning from resonance. For each axial position of the ion the linewidth is measured at

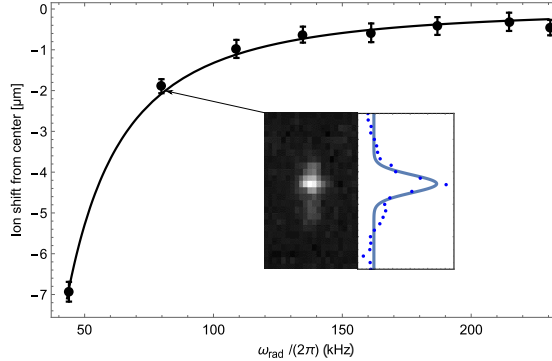


**Figure 5.14:** Radial ion position shift in the  $x$ -direction plotted against the radial confinement. The measured positions are fitted with a model function in order to determinate the DC electric field. The insets show a camera image of an ion and a Gaussian fit to the fluorescence.

two trap drive amplitudes of 225 V and 67 V. Thus, the line shape is measured at two values for  $\beta_{\text{MM}}$  differing by a factor of 3.3 which allows to determine  $\Gamma_0$  and the MM-induced broadening. From a combined fit as shown in the insets of figure 5.13 we get a linewidth without MM of  $\Gamma_0 \approx 2\pi \times 4$  MHz and a position-dependent MM amplitude as shown in figure 5.13. At a trap drive amplitude of 75 V, as used for the atom-ion collision experiments in chapter 7, we calculate an upper bound to the amplitude of the oscillating electric field in the trap center of  $\mathbf{E}_{\text{ac,ax}} \leq 15 \text{ V} \cdot \text{m}^{-1}$  corresponding to a MM energy of  $E_{\text{MM}} \leq k_{\text{B}} \times 2.5$  mK. At these settings, the axial field gradients can be described by an axial stability parameter  $q_{\text{ax}} = 0.0023$ , which result in axial MM energies of about 3 mK for the outer ions in a 5-ion crystal.

## 5.6.2 Radial micromotion compensation

In both radial directions the time-averaged ion position is monitored with respect to the radial confinement by varying the trap drive amplitude. From these position shifts the dc electric field  $\mathbf{E}_{\text{dc,rad}}$  responsible for the radial ion shift can be deduced.

In the horizontal  $x$ -direction this is done by taking camera pictures while varying the radial trap frequency from  $\omega_{\text{rad}} = 2\pi \times 40$  kHz to  $\omega_{\text{rad}} = 2\pi \times 220$  kHz as shown in figure 5.14. The ion position is determined with an accuracy of

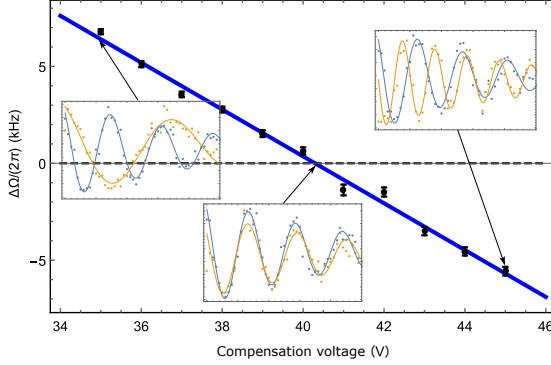


**Figure 5.15:** Radial position shift of an  $^{171}\text{Yb}^+$  ion in the vertical  $z$ -direction plotted against the compensation voltage. The frequency difference of the  $^2\text{S}_{1/2}$  ground state  $|F=0, m_F=0\rangle \rightarrow |1, 1\rangle$  transition in a magnetic field gradient is shown for different compensation voltages. The insets show the Ramsey measurements at radial trap frequencies of  $\omega_{\text{rad}} = 2\pi \times 80$  kHz (yellow) and  $\omega_{\text{rad}} = 2\pi \times 230$  kHz (blue). For optimal compensation the applied voltages at the upper (lower) compensation electrodes are  $\approx (-)20$  V which corresponds to a dc electric offset field of  $E_{\text{dc}} \approx 35 \text{ V}\cdot\text{m}^{-1}$ .

200 nm by fitting a Gaussian distribution to the camera pictures (see inset of figure 5.14). The main limiting factor is the compensation of the horizontal ion position with the compensation electrodes. Here,  $\pm 1$  V at the electrodes yields only  $10^{-3} \text{ V}\cdot\text{m}^{-1}$  at the ion position<sup>5</sup>. Thus,  $\mathbf{E}_{\text{dc}}$  needs to be reduced beforehand as far as possible which is done by regularly *baking*<sup>6</sup> the rf electrodes.

In vertical  $z$ -direction the ion position cannot be determined precisely with the camera, as it is imaged from above (see figure 4.35). Here, the magnetic field sensitivity of the  $^2\text{S}_{1/2}$  ground state  $|F=0, m_F=0\rangle \rightarrow |1, 1\rangle$  transition in  $^{171}\text{Yb}^+$  is utilized. For the measurement a vertical magnetic field gradient of  $g_z = 0.15 \text{ T}\cdot\text{m}^{-1}$  is applied leading to a frequency shift of  $2.1 \text{ kHz}\cdot\mu\text{m}^{-1}$ . As shown in figure 5.15 the ion position is precisely determined with respect to the rf node by means of Ramsey spectroscopy (see section 5.5) at two different radial confinements of  $\omega_{\text{rad}} = 2\pi \times 80$  kHz and  $\omega_{\text{rad}} = 2\pi \times 230$  kHz.

With these two techniques the radial MM energy is  $E_{\text{MM}} \leq k_{\text{B}} \times 2 \text{ mK}$  at optimal compensation, yielding a residual electric stray field of  $\mathbf{E}_{\text{dc},x} \leq 0.7 \text{ V}\cdot\text{m}^{-1}$ .

<sup>5</sup>In vertical  $z$ -direction the  $\pm 1$  V generates an electric field of  $0.7 \text{ V}\cdot\text{m}^{-1}$ .

<sup>6</sup>With helical resonator No. 2 (see chapter 4.6), the ion trap is driven with high frequency and amplitude which leads to a temperature rise in the trap electrodes, due to their rather large capacity.

Additionally, the latter measurement allows to acquire the MM energy as a function of the applied voltage at the compensation electrodes. Here, a voltage of  $\pm 1$  V applied to the compensation electrodes yields a dc electric offset field of  $\Delta E_{\text{dc}} = 0.29(2) \text{ V}\cdot\text{m}^{-1}$ . The energy is then given by

$$E_{\text{MM}}(\Delta E_{\text{dc}}) = \frac{\Delta E_{\text{dc}}^2 \times e^2}{2 m_{\text{ion}} \times \omega_{\text{rad}}^2}, \quad (5.6)$$

where  $e$  is the elementary charge. This allows us to tune the MM energy as applied in the collision experiments in chapter 7.

## 5.7 Conclusions and outlook

In this chapter the ion trap is characterized. The measurement results are summarized in table 5.1. The performance of our ion trap was investigated in the first part of this chapter. We are able to resonantly load  $\text{Yb}^+$  ions of selected isotope and quantity. Those can be prepared in the electronic ground state  $^2\text{S}_{1/2}$  or in the excited electronic states  $^2\text{P}_{1/2}$ ,  $^2\text{D}_{3/2}$  or  $^2\text{F}_{7/2}$ . Here, the  $^2\text{S}_{1/2}$  ground state of the isotope  $^{171}\text{Yb}^+$  features a simple hyperfine structure. We use the magnetic field-insensitive "clock" transition  $|F=0, m_F=0\rangle \rightarrow |1, 0\rangle$  as well as the magnetic field-sensitive transitions  $|0, 0\rangle \rightarrow |0, \pm 1\rangle$  in order to measure the coherence of the state populations allowing to characterize decoherence in the setup. To optimize the coherence time, the magnetic noise in the setup needs to be reduced. This may be done by stabilizing the current in the magnetic field coils with a PID controller. Another highly effective technique which is relatively easy to employ is triggering on the 50 Hz ac-line for each measurement. The implementation of magnetic shielding is also recommended in order to suppress external magnetic field noise [137].

In the second part of the chapter we use a set of methods in order to identify and compensate for excess MM. At optimal compensation we reach MM energies of  $E_{\text{MM,rad}} \leq k_{\text{B}} \times 2 \text{ mK}$  in radial direction and  $E_{\text{MM,ax}} \leq k_{\text{B}} \times 2.5 \text{ mK}$  in axial direction. Those relate to radial and axial residual electric stray fields of  $\mathbf{E}_{\text{dc,rad}} \leq 0.7 \text{ V}\cdot\text{m}^{-1}$  and  $\mathbf{E}_{\text{ac,ax}} \leq 15 \text{ V}\cdot\text{m}^{-1}$ . For comparison, in Ref. [102] the residual fields are compensated to  $\mathbf{E}_{\text{dc,rad/ac,ax}} = 0.02/0.06 \text{ V}\cdot\text{m}^{-1}$  which in our case would yield a residual MM energy of  $E_{\text{MM,rad/ax}} \approx k_{\text{B}} \times 2/117 \mu\text{K}$  corresponding to a collision energy of  $E_{\text{col,rad/ax}} \approx k_{\text{B}} \times \frac{3}{2} \frac{\mu}{m_{\text{ion}}} E_{\text{MM,rad/ax}} = k_{\text{B}} \times 0.07/3.97 \mu\text{K}$ , neglecting the energy of the  $^6\text{Li}$  atoms. Therefore, we plan to enhance MM compensation. In the first place, our experimental setup will

$\kappa_{\text{ax}}$	0.097(1)
$\kappa_{\text{rad}}$	0.797(48)
$t_{\text{coh.}, 0,0\rangle\rightarrow 1,0\rangle}$	6.9(3) ms
$t_{\text{coh.}, 0,0\rangle\rightarrow 1,1\rangle}$	0.31(2) ms
thermal energy	$k_B \times 4 \text{ mK}$
heating rate	$\leq k_B \times 4 \text{ mK/s}$
$E_{\text{MM,ax}}$	$\leq k_B \times 2.5 \text{ mK}$
$E_{\text{MM,rad}}$	$\leq k_B \times 2 \text{ mK}$

**Table 5.1:** Summary of the results obtained in the ion trap measurements. Here,  $\kappa_{\text{ax/rad}}$  is the axial/radial geometry factor of the ion trap,  $t_{\text{coh.},|A\rangle\rightarrow|B\rangle}$  is the coherence time of the state population when driving the  $|A\rangle \rightarrow |B\rangle$  transition and  $E_{\text{MM,ax/rad}}$  is the residual axial/radial MM energy after MM compensation.

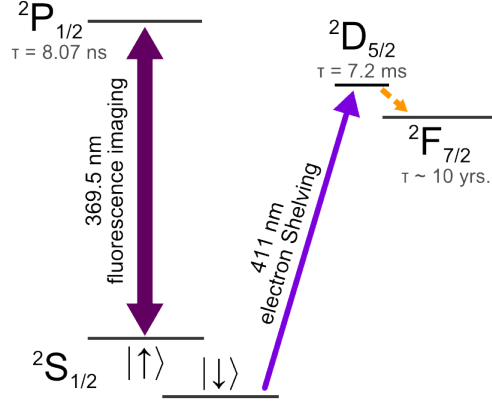


**Figure 5.16:** Electron shelving scheme. The population of  $|\downarrow\rangle$  is pumped into the  ${}^2F_{7/2}$  state by driving the  ${}^2S_{1/2} \rightarrow {}^2D_{5/2}$  transition.

be optimized by adding two additional pairs of compensation electrodes to the ion trap in order to more efficiently compensate in the horizontal  $x$ -direction. Even so, the sensitivity and accuracy of MM detection needs to be improved. On the one hand, this may be done by using the 329 nm frequency-quadrupled high power laser system (see chapter 4.9.1) in Raman configuration. On the other hand there will be a 411 nm laser system for projective measurements via electron shelving as described below. Due to its small linewidth, the motional sidebands can be resolved which will improve the accuracy of MM detection and thus will allow for better compensation.

The scheme for the electron shelving method [138] is shown in figure 5.16. Here, the Zeeman split  ${}^2S_{1/2}$  ground state or, in case of  ${}^{171}\text{Yb}^+$ , one of the  ${}^2S_{1/2}$  hyperfine states is selectively excited into the state  ${}^2D_{5/2}$ , which decays into metastable state  ${}^2F_{7/2}$ , before applying fluorescence detection. This will improve the fidelity of state detection.



## 6 — Trapped atoms

To perform atom-ion experiments in the ultracold regime, the initialization of both, atoms and ions, in a defined target state is of utmost importance. In this chapter we report on the preparation of a cold cloud of neutral  ${}^6\text{Li}$  atoms in our experiment and the transport of the atomic cloud to the  $\text{Yb}^+$  ions. The individual stages are explained and characterized in terms of trapped atom numbers and achieved temperatures.

## 6.1 Introduction

Atom-ion experiments in the quantum regime, as planned for future experiments with this experimental setup (see chapter 1), require ultracold atomic gases. Following Ref. [139], creating a degenerate Fermi gas of  ${}^6\text{Li}$  can be achieved by trapping and cooling in a magneto optical trap (MOT), optical trapping in a crossed optical dipole trap (ODT) and forced evaporative cooling.

In this chapter, we explain the trapping of neutral  ${}^6\text{Li}$  atoms in our setup and the transport of the atoms to the location of the  $\text{Yb}^+$  ions. This procedure is used in chapter 7, where we describe the first experimental results on interacting  ${}^6\text{Li}$  atoms and  $\text{Yb}^+$  ions. In the future, we plan to further cool the atoms to reach quantum degeneracy. However, the experiments described in this thesis deal only with thermal clouds of  ${}^6\text{Li}$  atoms. The setup and operation of the optical dipole trap and the subsequent evaporative cooling stage will be described in Ref. [104].

Our experimental sequence is presented in section 6.2. Following this scheme, we are able to provide  $7 \times 10^6$   ${}^6\text{Li}$  atoms at the ion position at a temperature of  $T = 0.6(2)$  mK. The peak density of the atomic cloud is  $\rho_{\text{Li}} = 49(15) \times 10^{14} \text{ m}^{-3}$ .

## 6.2 Sequence

A protocol of the sequence to provide atoms for the collision experiments in chapter 7 is shown in figure 6.1. Additionally, the MOT loading and compression, as well as the magnetic trap and the transport of the atomic cloud are illustrated in figure 6.2.

### magneto optical trap (MOT)

${}^6\text{Li}$  atoms evaporated in the Li oven at  $400^\circ\text{C}$  form an atom beam with a mean velocity of several 100 m/s which is decelerated in the Zeeman slower (see section 4.7.4). They are loaded into a mMOT as shown in figure 6.2. The mMOT is made using two pairs of circularly polarized<sup>1</sup> counterpropagating laser beams  $-34$  MHz red detuned from the  $D2$  cooling transition and superimposed at the node of a magnetic quadrupole field. In contrast to a standard MOT where three pairs of counterpropagating laser beams ensure cooling and trapping in all axes [141], one of the two cooling laser beam pairs is reflected at the MOT mirror in the center under an incident angle of  $45^\circ$ . Consequently, an atom

---

<sup>1</sup> $\sigma^+$  polarized with respect to the direction of propagation.

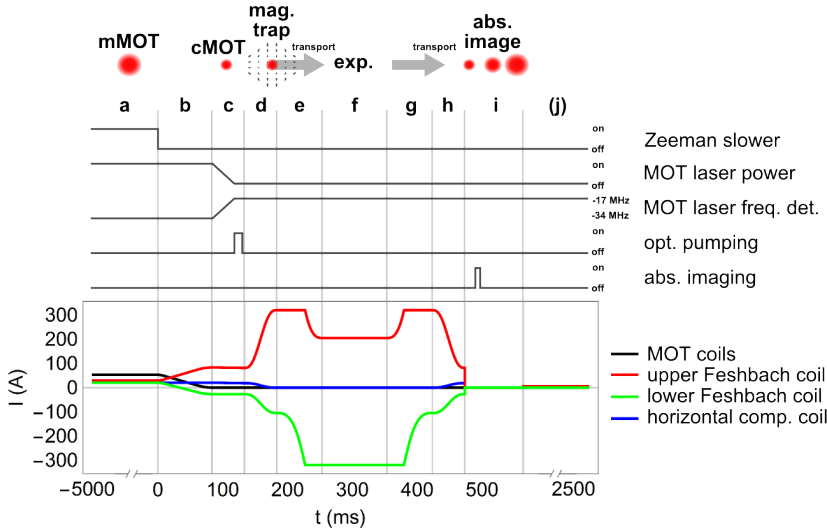


**Figure 6.1:** Experimental sequence protocol to provide <sup>6</sup>Li atoms at the ion location. The vertical lines separate the particular stages which are: (a) Trapping and cooling of <sup>6</sup>Li atoms in a mirror MOT (mMOT); (b) transfer of the MOT into the magnetic gradient field of the Feshbach coils; (c) MOT compression and the preparation of the atoms in a low-field seeking state with subsequent magnetic trapping; (d)–(e) adiabatic transport of the atomic cloud into the ion trap center; (f) atom-ion experiment; (g)–(h) adiabatic transport back to the MOT location; (i) absorption imaging of the atomic cloud; (j) state detection of the ions (see chapter 7). See text for further information. Graphics adapted from Ref. [140].

located at the overlap of the two beams and the reflected beam is in an equal light field as in a standard MOT [142]. A mMOT provides confinement and cooling of the atoms close to a surface, hence, in our case at a minimal distance to the Paul trap.

Initially, the magnetic quadrupole field for the MOT is generated by the MOT coils (see chapter 4.8), while dynamically adjustable currents in the horizontal compensation coils and Feshbach coils allow to generate homogeneous fields in order to displace the quadrupole field minimum in horizontal and vertical direction (see figure 6.1 (a)). In 3 s loading time and with a magnetic field gradient of  $g_z = 36 \text{ G/cm}$  about  $50 \times 10^6$  <sup>6</sup>Li atoms are trapped in an atomic cloud of diameter  $\approx 2 \text{ mm}$ . The atoms are cooled close to the Doppler

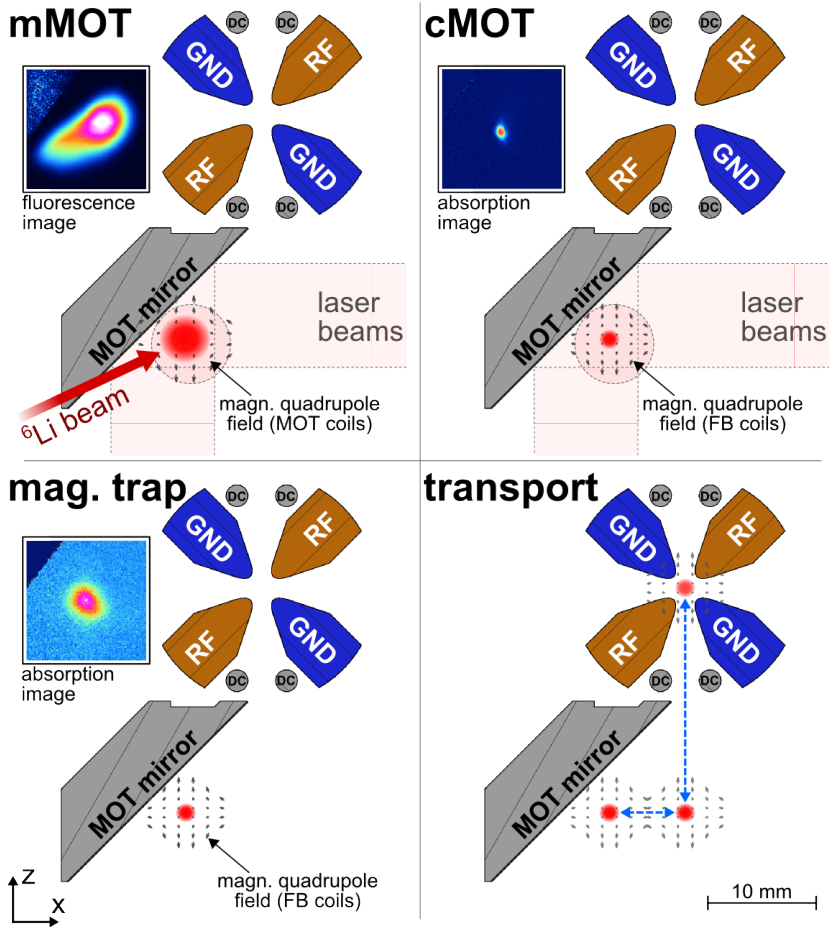


**Figure 6.2:** Sectional drawings of the trap setup to illustrate the steps in the sequence. The insets show fluorescence or absorption images of the atomic cloud. In the first stage,  ${}^6\text{Li}$  atoms in an atom beam from a Zeeman slower are loaded into a mMOT approximately 20 mm below and slightly shifted horizontally from the ion trap center. After the MOT has been transferred from the quadrupole field of the MOT coils to the quadrupole field of the Feshbach coils the size of the atomic cloud is reduced in a compressed MOT (cMOT) shortly before the atomic cloud is transferred into a magnetic trap in the same magnetic field. The transport into the ion trap and back to the MOT location is performed by shifting the field minimum of the quadrupole field.

temperature of  $T_D = 141 \mu\text{K}$ .

After the loading process, the Zeeman slower beam is turned off and the mechanical shutter at the  ${}^6\text{Li}$  oven is closed to increase the lifetime of the MOT. Subsequently, the current in the MOT coils is decreased while simultaneously tuning the Feshbach coils from Helmholtz to anti-Helmholtz configuration by applying opposite currents (see figure 6.1 (b)). As a result the MOT has been transferred from the magnetic quadrupole field of the MOT coils, which are slow but allow for a large capture volume, into the field of the Feshbach coils at the same position. The Feshbach coils provide a smaller capture volume, but the current applied can be changed much quicker due to their lower inductance.

### compressed MOT (cMOT) and magnetic trap

The minimum distance between two blade electrodes of the Paul trap is 1.8 mm. Thus, the diameter of the atomic cloud needs to be reduced in order to enable the transfer into the ion trap. To compress the MOT we reduce the laser power of the MOT beams while tuning the cooling laser closer to resonance (from  $-34$  to  $-17$  Mhz – see figure 6.1 (c)). The diameter of the atomic cloud in the cMOT is significantly reduced as can be seen in the inset in figure 6.2. At the end of this stage the  ${}^6\text{Li}$  atoms are spin polarized into the  ${}^2\text{S}_{1/2} |F = 3/2, m_F = 3/2\rangle$  state by a pulse of circular polarized light resonant on the  $D1$  transition and thus transferred into a magnetic trap as shown in figure 6.2. We trap  $25 \times 10^6$  atoms in the magnetic trap, at a temperature of  $T \approx 180 \mu\text{K}$ . The size of the atomic cloud in the magnetic trap with a magnetic field gradient of  $g_z = 44 \text{ G/cm}$  is  $\sigma_{\text{ax}} \approx 1000 \mu\text{m}$  and  $\sigma_{\text{vert}} \approx 600 \mu\text{m}$ .

### transport

The transport of the atomic cloud into the ion trap is performed in two steps (see figure 6.2). First, the cloud is moved to the horizontal center exactly underneath the center of the ion trap (see figure 6.1 (d)) before being elevated to the ion position (see figure 6.1 (e)). To ensure an adiabatic transport of the atomic cloud the position of the trap minimum as well as the magnetic gradients during the transport are parameterized to follow a smooth polynomial function assuring a soft compression, acceleration and deceleration of the atoms<sup>2</sup> as presented in Ref. [104]. During the transport the magnetic trap is compressed further to a final gradient of  $280 \text{ G/cm}$  within the time  $T_{\text{tr}} = 120 \text{ ms}$ . This reduces atom losses during the transport caused by geometrical cutoff at the compensation electrodes, and rf evaporation in the immediate vicinity of

<sup>2</sup>Due to the vanishing first and second order derivatives at the endpoints.

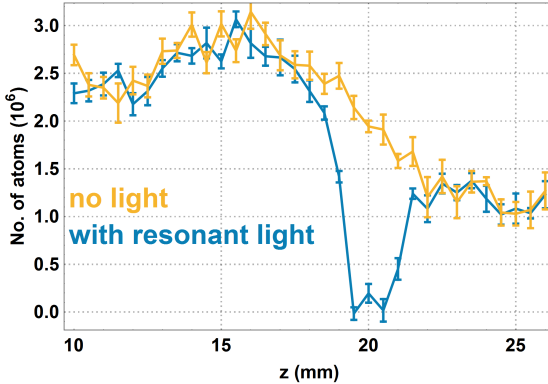


**Figure 6.3:** Elevation height scan of the atomic cloud with and without resonant light on the  $D1$  transition of  ${}^6\text{Li}$  at the ion position. Note that the height given here follows from magnetic field calculations.

the rf electrodes. In the present setup, the magnetically trapped atomic cloud cannot be imaged accurately inside the ion trap due to limited optical access. Thus, in order to measure the temperature of the atomic cloud as well as the atom number after the transport, the atomic cloud is transported back to the initial MOT location (see figure 6.1 (g)–(h)). Upon arrival, the magnetic fields are ramped to zero which takes  $\approx 2$  ms and absorption imaging is performed (see figure 6.1 (i)). From comparing these results with measurements without transport we conclude, that we provide  $7 \times 10^6$  atoms at the location of the ions, at a temperature of  $T = 0.6(2)$  mK.

### 6.3 Elevation height measurement

To overlap the atoms and ions, the elevation height of the atomic cloud needs to be determined. This was done using two different measurement methods. First, the elevation height was scanned while at maximum elevation a low power laser pulse resonant with the  $D1$  transition of  ${}^6\text{Li}$  and focused onto the ion position was applied. To ensure the alignment of the laser beam it was coupled in via the same fiber coupler used for the 935 nm repumper transition in  $\text{Yb}^+$  through the holes in the end caps (see figure 4.34). The result is shown in figure 6.3. Without light the number of atoms starts decreasing when elevated higher than  $\approx 17$  mm. This is due to the geometrical cutoff at the compensation electrodes and ion trap blades and rf evaporation at the rf blades. With resonant light this effect can also be observed. In addition, the picture changes significantly when the atomic cloud is hit by the laser light, as the atom number drops to zero.

From this we estimate the vertical ion position to be  $z \approx 20$  mm with respect to the MOT which was used as rough setting.

A much more precise and elegant approach is to use  $\text{Yb}^+$  ions as sensor. Collisions between the atoms and electronically excited ions lead to ion losses while the ion loss rate depends on the density of the atomic cloud. Thus, by measuring the loss rate in dependence to the position of the atomic cloud the relative position between the atoms and ions can be determined with much higher accuracy. Additionally, since we could not reliably image the atoms within the ion trap yet, we can use this measurements to determine the local atomic density at the ions. These measurements were done within the scope of the experiments explained in chapter 7 and the results are found in section 7.4.1.

## 6.4 Conclusions and outlook

Stage	No. of atoms	T (mK)	$g_z$ (G/cm)	$(\sigma_{\text{ax}} \times \sigma_{\text{vert}})$ (mm $\times$ mm)
MOT	$\approx 50 \times 10^6$	$\approx 0.141$	36	$\approx (2 \times 2)$
mag. trap (at MOT)	$\approx 25 \times 10^6$	$\approx 0.18$	44	$\approx (1 \times 0.6)$
mag. trap (at ions)	$\approx 7 \times 10^6$	0.6(2)	280	$(0.47(4) \times 0.41(4))$

**Table 6.1:** Characteristic values of the main trapping stages for providing cool  ${}^6\text{Li}$  atoms at the ion position.

We have presented and characterized atom trapping as performed in our setup. The characteristics of the main stages are listed in table 6.1. The trap suffers from losses during the transfer into the magnetic trap and the transport. It is crucial to reduce those losses in order to maintain enough atoms to efficiently perform evaporative cooling to quantum degeneracy in future experiments. The scheme leaves considerable room for improvements and optimizations. First of all, absorption imaging needs to be established at the ion location in order to precisely measure the atom number and the temperature of the atomic cloud allowing to improve those parameters. Here, it is advantageous to realize the crossed ODT as the smaller dimensions of such a trap enable us to use the same objective as for the  $\text{Yb}^+$  ions. Besides, the performance of the transfer into the magnetic trap may be increased by optimizing the optical pumping process and by sub-Doppler cooling the atomic cloud in a gray molasses cooling scheme as

an intermediate step [143, 144]. To do so, the switch-off time of the magnetic field coils which is  $\approx 2$  ms needs to be reduced, e.g. by realizing a critically damped response with appropriate electrical circuits.

## 7 — Observation of collisions between cold Li atoms and $\text{Yb}^+$ ions

In this chapter we report on the observation of cold collisions between  ${}^6\text{Li}$  atoms and  $\text{Yb}^+$  ions<sup>1</sup>. For the atoms and ions prepared in the  ${}^2\text{S}_{1/2}$  ground state, the charge-transfer and association rate is found to be at least  $10^3$  times smaller than the Langevin collision rate. These results confirm the excellent prospects of  ${}^6\text{Li}\text{-Yb}^+$  for sympathetic cooling and quantum information applications. For  $\text{Yb}^+$  ions prepared in the excited electronic states  ${}^2\text{P}_{1/2}$ ,  ${}^2\text{D}_{3/2}$  and  ${}^2\text{F}_{7/2}$ , we find that the reaction rate is dominated by charge transfer and does not depend on the ionic isotope or the collision energy in the range  $\sim 1\text{--}120$  mK. The low charge-transfer rate for ground-state collisions is corroborated by theory, but the  $4f$  shell in the  $\text{Yb}^+$  ion prevents an accurate prediction for the charge-transfer rate of the  ${}^2\text{P}_{1/2}$ ,  ${}^2\text{D}_{3/2}$  and  ${}^2\text{F}_{7/2}$  states. Using *ab initio* methods of quantum chemistry the atom-ion interaction potential has been calculated up to energies of  $30 \times 10^3 \text{ cm}^{-1}$  in Ref. [145]. These are used to give qualitative explanations of the observed rates.

---

<sup>1</sup>This chapter was published as *Observation of collisions between cold Li atoms and  $\text{Yb}^+$  ions* by J. Joger, H. Fürst, N. Ewald, T. Feldker, M. Tomza and R. Gerritsma, Phys. Rev. A **96**, 030703(R) (2017) [145].

## 7.1 Introduction

Now, having achieved ion trapping (see chapter 5) and atom trapping (see chapter 6), we are in a position to produce a cold mixture of trapped ions and atoms. In this chapter, we will study the occurrence of chemical reactions between  $\text{Yb}^+$  ions and  ${}^6\text{Li}$  atoms. For our system to be of use in quantum technology applications, it is crucial that inelastic collision rates are low compared to elastic rates. Inelastic collisions can occur in the form of charge transfer  $\text{Li} + \text{Yb}^+ \rightarrow \text{Li}^+ + \text{Yb}$  or molecule formation  $\text{Li} + \text{Yb}^+ \rightarrow (\text{LiYb})^+$ . These elementary chemical reaction processes can be very efficiently studied in atom-ion systems, as the trapped ions allow for full control over their internal states and kinetic energy, while sophisticated detection schemes allow for studying the reaction products and their kinetic energy as well as branching ratios.

This chapter is structured as follows: Once the experimental setup is recapitulated in section 7.2 the sequence to perform the experiment is presented in section 7.3. As ion losses due to atom-ion collisions are proportional to the density of the atomic cloud at the ion position it can be measured very sensitively as shown in section 7.4.1. In section 7.4.2 we present experimentally determined rates for inelastic collisions between  ${}^6\text{Li}$  atoms and  ${}^{171}\text{Yb}^+$ ,  ${}^{174}\text{Yb}^+$  and  ${}^{176}\text{Yb}^+$  ions in the mK regime. We show that the inelastic rate for ground state atoms and ions is at least  $10^3$  times smaller than the Langevin collision rate, which should be sufficiently small for sympathetic cooling and quantum applications. These findings are in agreement with recent calculations [63, 146]. Furthermore, we prepare the ions in excited electronic states and show that the main inelastic process occurring in this situation is charge transfer. We find that for the  ${}^2P_{1/2}$  state and  ${}^2F_{7/2}$  state in the isotopes  ${}^{174}\text{Yb}^+$  and  ${}^{176}\text{Yb}^+$ , the inelastic rate approaches the Langevin collision rate, whereas for the metastable  ${}^2D_{3/2}$  state, we find inelastic rates that are more than an order of magnitude smaller. In section 7.4.3 we show that the charge transfer rate is almost independent of the collision energy, suggesting that charge transfer is to be associated with Langevin collisions. Our results do not depend strongly on the ionic isotope. In section 7.5, we provide qualitative arguments for the observed rates using theoretical calculations of the excited states of the  $(\text{LiYb})^+$  system.

## 7.2 Experimental setup

We overlap a cloud of  ${}^6\text{Li}$  atoms with a crystal of 2–5  $\text{Yb}^+$  ions for a certain interaction time to observe inelastic collision processes such as charge transfer

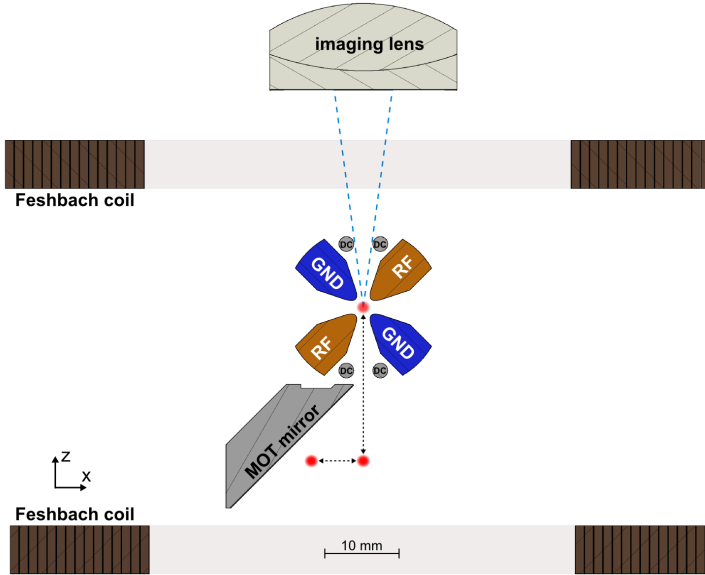


**Figure 7.1:** Sectional drawing of the setup used for the combined trapping, cooling and overlapping of  ${}^6\text{Li}$  atoms and  $\text{Yb}^+$  ions. The atoms are cooled in a mirror MOT about 20 mm below the Paul trap before they are magnetically transported into the ion trapping region.

or molecule formation. While the former leads to ion loss, because  $\text{Li}^+$  ions have a charge-to-mass ratio outside of the stability region of our Paul trap (see chapter 5.3), the latter results in a trapped, dark  $(\text{LiYb})^+$  molecular ion. After the interaction, the atoms are released and we image the ion crystal.

The techniques used for the initialization and state detection of  $\text{Yb}^+$  as well as for the trapping and transport of  ${}^6\text{Li}$  were explained in detail in chapter 5 and 6. Here, a short summary is given for completeness.

The main part of our experimental setup, which is presented in chapter 4 is sketched in Fig. 7.1. In 3 seconds we load about  $50 \times 10^6$   ${}^6\text{Li}$  atoms into a mMOT. The atoms are cooled close to the Doppler temperature of  $T_D = 141 \mu\text{K}$  before they are spin polarized into the  $F = 3/2, m_F = 3/2$  ground state and transferred into a magnetic trap. We trap  $25 \times 10^6$  atoms in the magnetic trap, at a temperature of  $T \approx 180 \mu\text{K}$ . The initial size of the atomic cloud in the magnetic trap is  $\sigma_{\text{ax}} \approx 1000 \mu\text{m}$  and  $\sigma_{\text{vert}} \approx 600 \mu\text{m}$ . During the transport

into the Paul trap we compress the magnetic trap from an initial gradient of  $g_z(0) = 0.44 \text{ T/m}$  to a final gradient of  $g_z(T_{\text{tr}}) = 2.8 \text{ T/m}$  within the time  $T_{\text{tr}} = 120 \text{ ms}$ . This reduces the size of the atomic cloud<sup>2</sup> leading to a higher atom density while reducing atom losses during the transport. Finally,  $7 \times 10^6$  atoms are trapped at the location of the ions at a temperature of  $T = 0.6(2) \text{ mK}$ .

At the Paul trap we apply an oscillating voltage with frequency  $\Omega_{\text{rf}} = 2\pi \times 2 \text{ MHz}$  and amplitude  $V_0 = 75 \text{ V}$  to two diagonally opposing blades and dc voltages of  $V_{\text{dc}} \approx 15 \text{ V}$  to the end caps, which yields radial and axial trap frequencies of  $\omega_{\text{rad}} = 2\pi \times 150 \text{ kHz}$  and  $\omega_{\text{ax}} = 2\pi \times 45 \text{ kHz}$ . The ions' kinetic energy is composed of the thermal energy in the order of  $T_{\text{Yb}} \approx 4 \text{ mK}$  after Doppler cooling, and the MM energy. We measure and compensate the MM in all three dimensions by using a set of complementary methods as described in chapter 5.6.

### 7.3 Experimental sequence

For the collision measurements we prepare the ions in the  $^2S_{1/2}$  ground state, or in one of the excited states  $^2P_{1/2}$ ,  $^2D_{3/2}$ ,  $^2F_{7/2}$ , as described in chapter 5.4. As the preparation time of the  $^2F_{7/2}$  state is much longer as for the other states, it is prepared before loading the atoms. Thus, the atoms interact with the ion already during the vertical transport and we correct the bare interaction time of  $25 \text{ ms}$  to  $\tau_F = 39 \text{ ms}$  as described in appendix F. For the other electronic states, the ions are initially in the  $^2S_{1/2}$  ground state during the transport of the atoms and only prepared in the desired state after arrival of the atoms.

Before and after the interaction we detect the ions by imaging the fluorescence light onto a sCMOS camera (see chapter 4.11) and determine the number of lost ions within the experimental run. The interaction time was set such that on average less than one ion was lost per experimental run. For a precise determination of the atom number, the atoms are transported back to their initial location and released from the magnetic trap. We apply a homogeneous magnetic field and after a time of flight of  $2 \text{ ms}$  we take an absorption image with circular polarized light resonant on the  $^2S_{1/2} \rightarrow ^2P_{3/2}$  transition.

---

<sup>2</sup>The size of the atomic cloud at the ion position is determined in section 7.4.1.

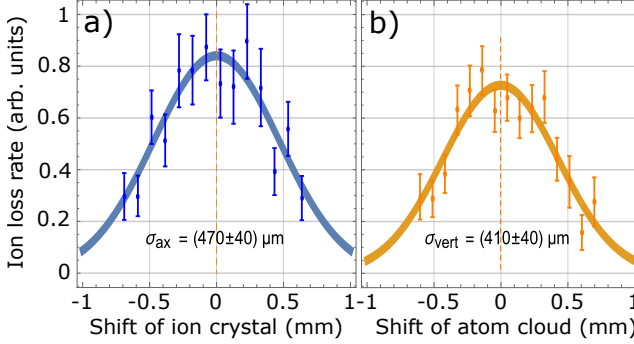


**Figure 7.2:** a) Density profile of the atomic cloud along the symmetry axis of the Paul trap (magnetic field gradient  $g_{\text{rad}} = 1.4 \text{ T/m}$ ). Ions are prepared in the metastable  $^2D_{3/2}$  state. We shift the ions along the trap axis and measure the loss rate at each position with an interaction time of 100 ms. b) Density profile in vertical direction ( $g_z = 2.8 \text{ T/m}$ ). The ions are kept in the axial center of the cloud and the atomic cloud’s transport elevation is scanned. Again, loss rates in the  $^2D_{3/2}$  state for an interaction time of 100 ms are measured.

## 7.4 Results

### 7.4.1 Density profile of the atomic cloud

To obtain the Langevin collision rate, we first measure the density profile of the atomic cloud by measuring ion loss rates of  $^{174}\text{Yb}^+$  ions prepared in the metastable  $^2D_{3/2}$  state as a function of the relative position within the atomic cloud. The vertical density profile is obtained by measuring the loss rates at different transport elevations of the magnetic trap minimum, while the horizontal density profile is determined by shifting the ion string to different positions along the symmetry axis of the Paul trap by tuning end cap voltages. From the density profile shown in Fig. 7.2 we determine the size of the atomic cloud to be  $\sigma_{\text{ax}} = 470(40) \mu\text{m}$  and  $\sigma_{\text{vert}} = 410(40) \mu\text{m}$ , which in combination with the atom number measurements gives us the atom density in the center of the cloud  $\rho_{\text{Li}} = 49(15) \times 10^{14} \text{ m}^{-3}$ . From this, we determine the rate of Langevin collisions to be  $\gamma_{\text{L}} = 2\pi\rho_{\text{Li}}\sqrt{C_4/\mu} = 23(7) \text{ s}^{-1}$ . Here,  $C_4$  is proportional to the polarizability of the atom and  $\mu$  is the reduced mass. In these measurements, the collision energy was set to  $\sim 30\text{--}50 \text{ mK}$ . In this range, the inelastic rate does not depend on the exact collision energy as described below.

### 7.4.2 Loss rates

From the Langevin rate and the observed ion loss rates, we obtain the fraction of Langevin collisions that lead to ion losses. The measured loss rates in units of Langevin collision rates are given in Table 7.1. For the  $^2S_{1/2}$  state only an upper bound is given as the observed loss rates are too low to be measured precisely with the currently available experimental setup.

State	$^{174}\text{Yb}^+$	$^{176}\text{Yb}^+$	$^{171}\text{Yb}^+$
$^2S_{1/2}$	$\leq 10^{-3}$	$\leq 2 \times 10^{-4}$	$\leq 2 \times 10^{-4}$
$^2P_{1/2}$	0.50(4)(20)	0.50(6)(20)	—
$^2D_{3/2}$	0.030(1)(11)	0.025(1)(10)	—
$^2F_{7/2}$	0.46(3)(16)	0.41(3)(14)	—

**Table 7.1:** Loss rates in units of Langevin collision rates for the isotopes  $^{174}\text{Yb}^+$ ,  $^{176}\text{Yb}^+$ ,  $^{171}\text{Yb}^+$  in ground and excited states. For the  $^2S_{1/2}$  and  $^2F_{7/2}$  state, the collision energy was set to  $\approx 1$  mK, whereas for the  $^2P_{1/2}$  and  $^2D_{3/2}$  states we took the average over the collision energy range  $\approx 1$ –100 mK (see Fig. 7.3). Errors are given for statistical and systematic uncertainties. The systematic uncertainty comes from the determination of the Langevin rate  $\gamma_L$  which affects all rates equally, as well as the  $^2P_{1/2}$  state population fraction for the loss rate of the  $^2P_{1/2}$  state. For the ground state, only upper boundaries could be determined as the rates lie close to background ion loss. For the measurement of the  $^2S_{1/2}$  state of  $^{171}\text{Yb}^+$ , the ion was prepared in the  $F = 0$  hyperfine ground state.

In principle, the methods developed in hybrid atom-ion systems also allow for studying collision-induced quenching to other electronic states [34]. Our results did not show evidence of collision-induced quenching from the  $^2F_{7/2}$  state to the electronic ground state. However, our experimental sequence does not allow for detection of quenching from the  $^2P_{1/2}$  and  $^2D_{3/2}$  state to the electronic ground state. During all measurements, we saw only few occurrences of dark ions and the rate is too low to distinguish these from unavoidable occurrences of  $^2F_{7/2}$  states or impurity ions induced by background gas collisions. From this we conclude that charge transfer dominates over association and quenching in the  $^2F_{7/2}$  state and over association in the  $^2D_{3/2}$  and  $^2P_{1/2}$  state.

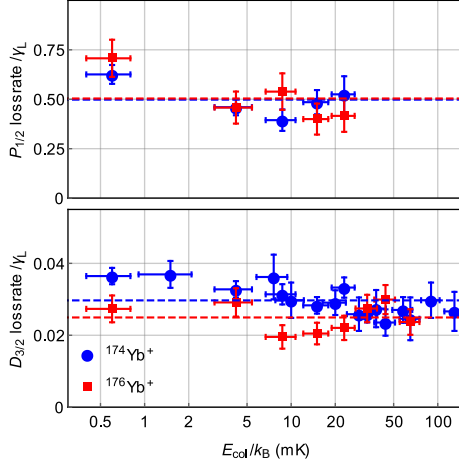


**Figure 7.3:** Collision energy dependence of ion loss rates for  $^{174}\text{Yb}^+$  ions (blue) and  $^{176}\text{Yb}^+$  ions (red), prepared in the  $^2P_{1/2}$  state (upper) and  $^2D_{3/2}$  state (lower). The dashed lines indicate the mean values of each rate.

### 7.4.3 Energy dependence of loss rates

We have also studied the energy dependence of the charge transfer rates for the  $^2P_{1/2}$  and  $^2D_{3/2}$  states. The average collision energy is given by [54]

$$E_{\text{col}} = \frac{3}{2} \frac{\mu}{m_{\text{Yb}}} \times E_{\text{Yb}} + \frac{3}{2} \frac{\mu}{m_{\text{Li}}} \times E_{\text{Li}}, \quad (7.1)$$

where  $m_{\text{Yb,Li}}$  and  $E_{\text{Yb,Li}}$  are the mass and kinetic energy of the  $\text{Yb}^+$  ions and  $^6\text{Li}$  atoms, respectively. Due to the high mass ratio  $m_{\text{Yb}}/m_{\text{Li}} \approx 29$ , the collision energy at low temperatures is limited by the temperature of the  $^6\text{Li}$  atoms ( $T_{\text{Li}} = 0.6(2)$  mK) even though the  $\text{Yb}^+$  ions' combined thermal and MM energy may be up to  $E_{\text{Yb}}/k_B \approx 10$  mK at optimal compensation [104]. For higher collision energies we deliberately apply a dc electric field of up to  $E_{\text{dc}} = 35$  V/m in radial direction, leading to a MM energy of up to  $E_{\text{MM}} = k_B \times 4$  K and a collision energy of up to  $E_{\text{col}} = k_B \times 120$  mK (see chapter 5.6.2).

We measure the loss rates in the energy range of  $E_{\text{col}}/k_B = 1$ –120 mK. The results are shown in Fig. 7.3. The measured charge transfer rates are mostly independent of collision energy from which we conclude that the inelastic processes occur during Langevin collisions, whose rate is independent of collision

energy [147].

## 7.5 Theory

In this section the results are compared with *ab initio* molecular structure calculations performed by Michał Tomza [63, 145].

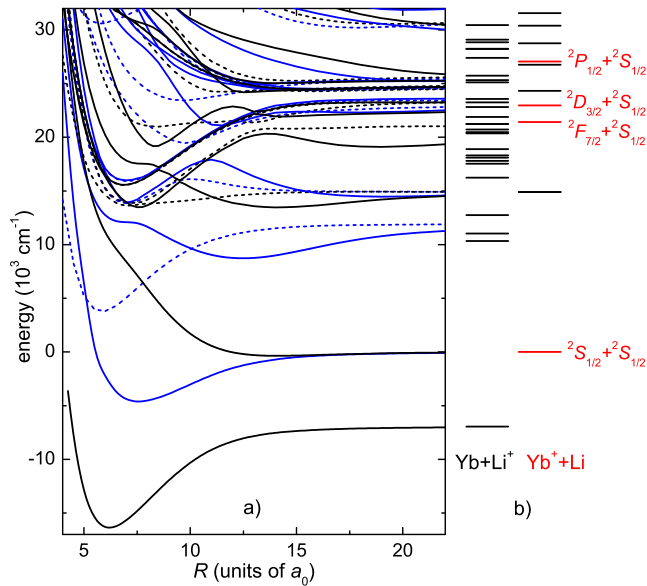


**Figure 7.4:** Energy spectrum of the system: a) Nonrelativistic potential energy curves of the  $(\text{LiYb})^+$  molecular ion. Black and blue lines correspond to singlet ( $S = 0$ ) and triplet ( $S = 1$ ) states, whereas solid and dashed lines represent states with the projection of the electronic orbital angular momentum on the molecular axis equal to zero ( $\Lambda = 0$ ,  $\Sigma$  symmetry) and non-zero ( $|\Lambda| > 0$ ), respectively. The lowest 5 electronic states are taken from Ref. [63]. b) Possible ion-atom dissociation thresholds with thresholds investigated in this work highlighted in red. Experimental energies are taken from the NIST database [148].

Fig. 7.4 presents non-relativistic electronic states of the  $(\text{LiYb})^+$  molecular ion up to an energy of about  $30 \times 10^3 \text{ cm}^{-1}$  above the  $\text{Yb}^+(^2S_{1/2}) + \text{Li}(^2S_{1/2})$  entrance channel. For comparison, Fig. 7.4 shows also all atomic dissociation

thresholds. The large number of atomic thresholds and electronic states makes it very difficult to build a complete microscopic *ab initio* model of charge transfer processes in the  $(\text{LiYb})^+$  system. Nevertheless, several conclusions can be drawn from the analysis of its electronic structure.

The small rates of the charge transfer for  $\text{Yb}^+$  ions in the  $^2S_{1/2}$  state are related to the large separation of the  $\text{Yb}^+(^2S_{1/2})+\text{Li}(^2S_{1/2})$  threshold from other thresholds, reducing potential losses due to spin-orbit [149] and non-adiabatic [150] couplings. At the same time, the relatively small photon energy realized in radiative charge transfer reduces its Einstein coefficients<sup>3</sup>.

The large rates of the charge transfer for  $\text{Yb}^+$  ions in the  $^2P_{1/2}$  state are due to relatively large spin-orbit coupling of the  $^2P$  state ( $^2P_{1/2}$ - $^2P_{3/2}$  splitting over  $3300\text{ cm}^{-1}$ , see table A.1) and the large number of accessible channels for both radiative and non-radiative losses.

The relatively small charge transfer rate of the  $^2D_{3/2}$  state can be related to the smaller spin-orbit coupling of the  $^2D$  state, which results in a splitting between the  $^2D_{3/2}$  and  $^2D_{5/2}$  states of  $< 1400\text{ cm}^{-1}$ . In addition, the  $\text{Yb}^+(^2D_{3/2})+\text{Li}(^2S_{1/2})$  threshold is surrounded by charge-transferred thresholds with a different configuration of *f*-shell electrons which should result in small coupling and mixing between related molecular electronic states.

Similarly, the large charge transfer rates for the  $^2F_{7/2}$  state can be related to the very large spin-orbit coupling for the  $^2F$  state which results in a splitting between the  $^2F_{7/2}$  and  $^2F_{5/2}$  states of  $> 10\,100\text{ cm}^{-1}$ . Such a strong spin-orbit coupling efficiently mixes many electronic states associated with several thresholds providing opportunities for efficient radiative and non-radiative charge transfer. In contrast to the  $^2D_{3/2}$  state, the  $\text{Yb}^+(^2F_{7/2})+\text{Li}(^2S_{1/2})$  threshold is surrounded by charge-transferred thresholds with the same configuration of *f*-shell electrons within several hundred  $\text{cm}^{-1}$ . Therefore, large coupling and mixing between related molecular electronic states is expected.

The comparison of the present results with charge transfer rates measured for  $\text{Yb}^+(^2F_{7/2})+\text{Rb}(^2S_{1/2})$  and  $\text{Yb}^+(^2D_{3/2})+\text{Rb}(^2S_{1/2})$  [34] suggests that in fact the electronic configuration of atomic thresholds and related molecular states surrounding the entrance channel determines the short-range probability of charge transfer. In Ref. [34], faster charge transfer rates were measured for  $\text{Yb}^+$  ions in the  $^2D_{3/2}$  state as compared to the  $^2F_{7/2}$  state (opposite to the present system). However, the  $\text{Yb}^+(^2D_{3/2})+\text{Rb}(^2S_{1/2})$  threshold is surrounded by charge-transferred thresholds with the same configuration of *f*-

---

<sup>3</sup>The Einstein coefficient  $A$  ( $B$ ) gives the probability for a emission (absorption) process to occur [133].

shell electrons, whereas the  $\text{Yb}^+(^2F_{7/2})+\text{Rb}(^2S_{1/2})$  threshold is surrounded by charge-transferred thresholds with a different configuration of  $f$ -shell electrons (also opposite to the present system and in agreement with our qualitative explanation).

## 7.6 Conclusions

We have presented experimental data on cold collisions between Li atoms and  $\text{Yb}^+$  ions that address two important issues: First of all, we have shown that inelastic collision rates for atoms and ions prepared in their electronic ground states are at least  $10^3$  times smaller than the Langevin rate. This is in agreement with theory [63, 146]. These results are of key interest for experiments aiming to use atom-ion systems for sympathetic cooling [30, 41, 68] and in quantum information applications [31–33]: due to the large mass ratio  $\text{Yb}^+-\text{Li}$  may be the only combination that can reach the quantum regime in a Paul trap [50].

Secondly, the study of cold chemical processes such as the charge transfer observed in this work, allows us to gain a deeper understanding of the molecular  $(\text{Li-Yb})^+$  system. The  $4f$  shell in the  $\text{Yb}^+$  ion prevents an accurate theoretical prediction of the charge transfer rate of the  $^2P_{3/2}$ ,  $^2D_{3/2}$  and  $^2F_{7/2}$  states using standard methods of quantum chemistry. Accurate measurements of chemical reactions between individual particles with full control over energy and internal states such as presented here, thus provide an excellent test bed for *ab initio* molecular structure calculations. The presented results can be used to benchmark methods designed to account for the static correlation, which is related to the heavy multireference nature, and strong relativistic effects, including huge spin-orbit coupling, that are present in the excited states of the  $(\text{LiYb})^+$  molecular ion. The development of such electronic structure methods is also relevant for systems containing other lanthanide atoms, e.g. erbium and dysprosium.

## 8 — Summary and outlook

This thesis introduces our novel experiment for which we invented and built an apparatus capable of trapping, cooling and physically overlapping  ${}^6\text{Li}$  atoms and  $\text{Yb}^+$  ions. Although our main objective of reaching the quantum regime of interacting atoms and ions has not yet been achieved in this thesis we did answer two important scientific questions that point the way towards attaining it:

1. We have found out that if we want to use the atom-ion platform as a quantum simulator we need to take into consideration the micromotion (MM) of the ions. In particular, a large ion-atom mass ratio is needed and excess MM has to be compensated very well.
2. We have found out that cold collisions between  $\text{Yb}^+$  ions and  ${}^6\text{Li}$  atoms lead to chemical reactions less than once every 1000 collisions. This important result indicates that chemical processes do not form a barrier for reaching the quantum regime and using the atom-ion system in quantum applications. Furthermore, we have studied chemical processes during collisions of atoms with  $\text{Yb}^+$  ions in electronically excited states and found charge-transfer rates. Such chemical reactions at the single particle level are of prime interest for quantum chemists. In particular, the complex level structure of  $\text{Yb}^+$  does not allow for an exact calculation of such charge transfer rates and our measurements could be used as a test bed for molecular structure calculations.

### Detailed summary

In chapter 2 we provide the basic theory of atom-ion interactions and collisions. In addition, we discuss ion trapping and atom-ion dynamics in a Paul trap. According to Ref. [50] we show, that in contrast to similar experiments on

different atom-ion species the  ${}^6\text{Li}\text{-Yb}^+$  system is most promising for reaching the  $s$ -wave scattering regime due to the large ion-atom mass ratio.

In chapter 3 we study theoretically the quantum dynamics of an ion-controlled atomic double-well system which can be seen as an atom-ion quantum simulator *unit cell*. This system was considered before [33, 61, 62], but up until now the effect of MM was not taken into account. In this thesis, we consider a more realistic case by including the MM of a trapped ion in a Paul trap. We find that the tunneling dynamics of the atoms from one side of the ion to the other is affected by MM. In particular, couplings to high energy states occur that appear as many avoided crossings in the energy spectrum. In an experiment this can cause unwanted heating and might prevent an accurate preparation of the input state. Thus, creating the double-well in the axial trap direction where there is no MM is advantageous. In addition, we study the effect of trap imperfections leading to excess MM and find, that proper MM compensation is inevitable. Either way, for a light atom and heavy ion these disturbing effects are less strong supporting our choice of species.

At the heart of this thesis in chapter 4 the experimental setup is presented. Here, we give detailed informations on the design of the ion trap and vacuum system as well as on the magnetic field coils, laser setup and the imaging system.

Chapters 5 and 6 serve to characterize the trap setup and experimental sequences in order to provide and initialize cold  $\text{Yb}^+$  ions and  ${}^6\text{Li}$  atoms, respectively, for atom-ion experiments. We have measured and compensated for excess MM of the  $\text{Yb}^+$  ions. The corresponding atom-ion collision energy is slightly larger than the  $s$ -wave scattering regime as calculated in Ref. [54]. Thus, further improvements on the experimental setup are required in the future [104].

In chapter 7 we present first experimental data on the  ${}^6\text{Li}\text{-Yb}^+$  system. Here, we study cold collisions with the  $\text{Yb}^+$  ions either in the ground state or in an excited electronic state. We find that for the ions in their electronic ground state the Langevin collision rate exceeds charge transfer rates by a factor of at least  $10^3$ . This result is of prime importance as it is a central prerequisite for sympathetic cooling and quantum information applications as stated above. For the ions in the electronic ground state the observed loss rates are corroborated by theory whereas the  $4f$  shell in the  $\text{Yb}^+$  ion prevents exact theoretical predictions for the excited electronic states. These results are of importance in order to gain deeper understanding of the molecular  $(\text{Li}\text{-Yb})^+$  system.

In conclusion, we have presented our experimental setup, characterized atom- and ion-trapping and demonstrated the feasibility of hybrid atom-ion experiments. The results gained in our first measurements proved that the  $(\text{Li}\text{-Yb})^+$  system is sufficiently long chemically stable for the desired applications. A sec-

ond requirement on the system for quantum applications is that the rates for spin-changing collisions are small. This was investigated in Ref. [151] and will be presented in Ref. [104].

### Becoming quatum

After these measurements it is appropriate to improve on the setup in order to reach the  $s$ -wave scattering regime. Thus, the collision energy has to be reduced below the  $s$ -wave limit  $E^* = k_B \times 8.58 \mu\text{K}$ . For this purpose, the total energy of both species has to be minimized before sympathetic cooling to the lowest temperature limit can be carried out successfully.

To create an ultracold fermi gas of  ${}^6\text{Li}$  atoms the additional stages, trapping in an ODT and evaporative cooling to degeneracy by exciting a magnetic Feshbach resonance, are currently being realized. To do so, a second MOT stage has been set up inside the ion trap in which the atoms are loaded from the magnetic trap and re-cooled to the Doppler limit before being transferred into the ODT. This procedure increases the atom number and thus atomic density in order to reliably perform evaporation. Following this scheme we routinely prepare atomic samples at  $T_a < 1 \mu\text{K}$ .

In order to reduce the total energy of the  $\text{Yb}^+$  ions MM compensation needs to be improved. To enhance excess MM detection an additional laser system with a narrow spectral linewidth, small enough to resolve the motional sidebands, will be used. Secondary, the design of the ion trap-mount has undergone slight modifications by adding two additional pairs of compensation electrodes in the horizontal direction. This will allow for excess MM compensation in all axes. The calculations in Ref. [54] show, that after those minor improvements in MM compensation the quantum regime is within reach. Additionally, a novel technique is presented in Ref. [102] where the atoms are used as a very sensitive probe to detect and minimize excess MM. This scheme is also applicable to our experiment and may be employed to even reduce MM further.

In order to reduce the vibrational state of the  $\text{Yb}^+$  ions close to the ground state, resolved-sideband Raman cooling could be employed [152] using the 329 nm laser system presented in chapter 4.9.1. Alternatively, sympathetic cooling by the ultracold atoms could be used. The calculations in Ref. [54] show, that this should reduce the vibrational quantum number to about  $\bar{n} = 1.2$  even with our current limits on MM compensation. Additionally, the electron shelving method [138] as described in chapter 5.7 will be employed in order to improve the fidelity of state detection.

Instead of focusing on atom-ion systems with large ion-atom mass ratios

other working groups pursue different potential solutions in order to reach the  $s$ -wave scattering regime. Those systems all have their advantages and disadvantages. For instance, both, atoms and ions, can be trapped optically in two independent or in one single ODT or optical lattice. However, optical ion trapping is a tough task as the trap depth of the optical trapping potential is much less than the trap depth of the Paul trap. Especially, the sensitivity of the ions to electric stray fields limits attainable lifetimes. Nonetheless, as the positive prospects are evident such systems are currently being realized [153–156]. In our setup many potential electric stray field sources are nearby the ion location. Thus, only hybrid electro-optical ion trapping with an ODT for the ions together with the Paul trap at low amplitude could be applicable.

In order to mitigate the MM at the ion location it is also possible to use a higher-order ion trap featuring a nearly flat trapping potential in the center [79, 157]. However, as in such a potential the ion is only weakly localized this solution is not favorable for our experiment as many of the applications intended rely on the strong localization of the ions.

Another potential solution to the MM problem was invented in our group, Ref. [43, 158]. Here, the system of trapped ions interacting with atoms, coupled to Rydberg states, is investigated theoretically. The strong polarizability of the Rydberg-dressed atoms yields a boost of the interaction strength between the atoms and ions. As a result the length scale of the interaction is in the  $\mu\text{m}$  scale such that in principle no short-range collisions occur and the effect of MM induced heating can be neglected. Interestingly, this system would allow for reaching the ultracold regime for any atom-ion mass ratio. On the other hand, the idea has the drawback that additional infrastructure is required and too strong coupling to Rydberg states may cause ionization. This system will be investigated with our setup and the results will be presented in Ref. [159].

After all, our experiment could become an exquisite device for exploring atom-ion dynamics beyond the  $s$ -wave limit [54]. It will be of great interest to measure magnetically tunable Feshbach resonances between  $\text{Yb}^+$  ions and Li atoms as predicted in Ref. [63] and to take the steps towards the full control of chemical reactions at the single particle level and towards the proposed solid-state quantum simulator [32].

## 9 — Samenvatting en vooruitzichten

In dit proefschrift wordt het ontwerp en de bouw van onze nieuwe experimentele opstelling beschreven, waarmee we  ${}^6\text{Li}$  atomen en  $\text{Yb}^+$  ionen kunnen vangen, koelen en met elkaar in wisselwerking kunnen brengen. Het belangrijkste uiteindelijke doel is het bereiken van het zogenaamde quantum regime van wisselwerkende ionen en atomen. Alhoewel dit doel binnen mijn promotie onderzoek nog niet bereikt is, beschrijf ik wel twee belangrijke wetenschappelijke resultaten die laten zien hoe het quantum regime bereikt kan worden.

1. We hebben berekend dat we als we onze ionen-atomen systeem als quantum simulator willen gebruiken, we rekening moeten houden met de zogenaamde microbeweging van de ionen in hun Paul val. Het is verstandig om een atoom-ion combinatie te gebruiken met een grote massa verhouding (zoals  $\text{Yb}^+/\text{Li}$ ) en bovendien moet de zogenaamde ‘exces’ microbeweging zeer goed gecompenseerd worden.
2. We hebben experimenteel vastgesteld dat botsingen tussen koude  ${}^6\text{Li}$  atomen en  $\text{Yb}^+$  ionen in minder dan 1 in 1000 gevallen leidt tot een chemisch proces zoals het verspringen van de lading. Dit belangrijke resultaat laat zien dat chemische processen geen barrière vormen voor het bereiken van het quantum regime en voor het inzetten van het systeem in quantum applicaties. Verder hebben we botsingen bestudeerd tussen atomen en ionen in aangeslagen elektronische toestanden en hebben we voor deze botsingen de ladingsoverdracht waarschijnlijkheid bepaald. Het bestuderen van zulke chemische processen op het enkele deeltjes niveau is van grote waarde voor quantum chemici. In dit geval vormt de complexe elektronische structuur van het  $\text{Yb}^+$  ion bijvoorbeeld een grote barrière voor het berekenen

van chemische reactie waarschijnlijkheden. Onze metingen kunnen als test case gebruikt worden in nieuwe moleculaire structuur berekeningen.

### Gedetailleerde samenvatting

In hoofdstuk 2 behandelen we de theoretische achtergrond van atoom-ion interacties en botsingen. Verder behandelen de theorie van Paul ionen vallen en de dynamica van atomen en ionen in deze vallen. In navolging van Ref. [50] laten we zien dat van alle mogelijke atoom-ion combinaties,  $\text{Yb}^+/\text{Li}$  het meest veelbelovende systeem is om het quantum, of *s*-wave, regime te bereiken door de grote massa verhouding.

In hoofdstuk 3 bestuderen we in theorie de dynamica van een enkel ion dat gevangen is in het midden van een atomaire Josephson junctie gevormd door een potentiaal met twee minima aan beide kanten van het ion. Dit systeem kan opgevat worden als een enkele ‘bouwsteen’ of eenheidscel van een te bouwen atoom-ionen kristal quantum simulator. Deze opstelling was al eerder onderwerp van theoretische studies [33, 61, 62], maar tot nu toe waren de effecten van microbeweging in de Paul val niet meegenomen in de berekeningen. Hier analyseren we de meer realistische situatie waarin er microbeweging is. We berekenen dat het quantum tunnelen van een atoom van het ene naar het andere potentiaal minimum verandert door de aanwezigheid van microbeweging. De lagere energie niveaus van de Josephson junctie koppelen met hoog ge-exciteerde energie niveaus die in een experiment tot opwarming van het systeem kunnen leiden. Bovendien laten de berekeningen zien dat het lastig zal zijn om het systeem in een goed gedefinieerde begin toestand te brengen. Een voor de hand liggende oplossing is om de Josephson junctie uit te lijnen langs de as van de ionen val, aangezien er in die richting geen microbeweging is. Wel berekenen we dat in dat geval de ‘excess’ microbeweging compensatie erg goed moet zijn. We vinden ook dat het gebruik van een zwaar ion en een licht atoom helpt om deze problemen tegen te gaan, in overeenstemming met klassieke berekeningen aan soortgelijke systemen (zie hoofdstuk 2).

De kern van dit proefschrift wordt gevormd door hoofdstuk 4, waar de experimentele opstelling wordt beschreven. Hier geven we gedetailleerde informatie over het ontwerp van de ionen val, het vacuüm systeem, de spoelen en de laser en detectie systemen.

In hoofdstukken 5 en 6 wordt de karakterisatie van de atoom en ionen vallen beschreven. We analyseren ook de experimentele stappen om koude  $\text{Yb}^+$  ionen en  ${}^6\text{Li}$  atomen te prepareren. We hebben de excess microbeweging gemeten en zo goed mogelijk gecompenseerd. De bijbehorende atoom-ion interactie energie is

nog iets groter dan de  $s$ -wave limiet [54]. Er zijn dus nog verdere verbeteringen aan de experimentele setup nodig in de toekomst [104].

In hoofdstuk 7, worden de eerste experimentele data voor het  ${}^6\text{Li}\text{-Yb}^+$  systeem gepresenteerd. We hebben koude botsingen tussen  ${}^6\text{Li}$  en  $\text{Yb}^+$  ionen bestudeerd. We vinden dat voor ionen in de elektronische grondtoestand dat de Langevin botsingsfrequentie minstens 1000 keer groter is dan de ladingsoverdracht frequentie. Dit resultaat is van enorm belang, omdat de waarschijnlijkheid van chemische processen in atoom-ion botsingen klein moet zijn om ionen te buffer-gas koelen en om het systeem bruikbaar te laten zijn in quantum applicaties. Voor ionen in aangeslagen toestanden kan de ladingsoverdracht frequentie niet nauwkeurig berekend worden door de aanwezigheid van de  $4f$  shell in  $\text{Yb}^+$ . Onze resultaten zijn van belang voor een beter begrip van het moleculaire  $(\text{Li}\text{-Yb})^+$  systeem.

Concluderend hebben we een experimentele opstelling gepresenteerd, hebben we het vangen en koelen van atomen en ionen gekarakteriseerd en de haalbaarheid van hybride, ultrakoude atoom-ion experimenten aangetoond. De resultaten uit onze eerste experimenten laten zien dat  $\text{Yb}^+/\text{Li}$  chemisch lang genoeg stabiel is voor de gewenste applicaties. Een tweede vereiste is, dat de frequentie van spin flippen tijdens botsingen klein is. Dit is onderzocht in Ref. [151], en zal in detail gepresenteerd worden in Ref. [104].

### Het quantum regime bereiken

Na de metingen die gepresenteerd zijn in dit proefschrift, ligt het voor de hand om verbeteringen aan te brengen aan de experimentele opstelling zodat het  $s$ -wave regime bereikt kan worden. Hiervoor moet de botsingsenergie kleiner zijn dan de  $s$ -wave limiet  $E^* = k_B \times 8.58 \mu\text{K}$ . Om dit te bereiken moet de energie van zowel de atomen als de ionen verder terug gebracht worden.

Op dit moment worden in het lab de stappen gezet om  ${}^6\text{Li}$  af te koelen tot een ontaard Fermi gas. Hiervoor worden de atomen in een optische dipool val geladen en verdampings-gekoeld met behulp van een Feshbach resonantie. Om dit efficiënt te doen is een tweede MOT fase geïmplementeerd in de ionen val, voordat de atomen van de magnetische val in de optische dipool val geladen worden. Op deze manier beginnen we aan het verdampingskoelen met een betere fase-ruimte dichtheid en kunnen we routinematig atoom wolken met  $T_a < 1 \mu\text{K}$  prepareren.

Om de energie van de ionen terug te brengen is het nodig om de microbeweging beter te compenseren. In de toekomst zullen we allereerst onze microbeweging detectie verbeteren door een transitie met een kleine lijnbreedte

te gebruiken zodat de microbeweging sidebands individueel gemeten kunnen worden. Verder passen we het ontwerp van de ionen val aan door twee compensatie elektrodes toe te voegen. Hiermee kan de microbeweging in alle richtingen worden gecompenseerd. In Ref. [54] hebben we berekend dat met deze verbeteringen het quantum regime binnen bereik moet zijn. Een andere techniek voor het detecteren van microbeweging in de ionen is beschreven in Ref. [102], waar de atomen gebruikt worden als detector van microbeweging. Deze techniek kan ook in ons experiment worden toegepast, waarmee we de microbeweging nog verder terug kunnen brengen.

Om de vibrationele toestand van de ionen of te koelen tot dicht bij de grondtoestand kunnen we gebruik maken van ‘resolved sideband cooling’ [152] middels onze 329 nm laser. Buffer-gas koelen door de ultrakoude atomen kan ook gebruikt worden. De berekeningen in Ref. [54] laten zien dat dit de vibrationele ionen toestand zou moeten afkoelen tot  $\bar{n} = 1.2$  vibrationele quanta gemiddeld. Tot slot kan *electron shelving* [138] gebruikt worden om de toestandsbepaling van de ionen verder te verbeteren.

Behalve het toepassen van ion-atoom combinaties met een grote massa verhouding, proberen sommige groepen andere technieken te gebruiken om het quantum regime van wisselwerkende atomen en ionen te bereiken. Deze technieken hebben elk hun eigen voor- en nadelen. Ionen kunnen bijvoorbeeld optisch gevangen worden, waardoor er geen microbeweging is [154, 155]. Nadeel is dat optisch vangen van ionen erg lastig is omdat de valdiepte zo gering is in vergelijking met een Paul val. Ongecontroleerde elektrische velden kunnen daardoor voor een geringe levensduur zorgen. In onze opstelling zou eventueel een hybride optische-Paul val een optie kunnen zijn.

Een andere optie om microbeweging tegen te gaan is om een hogere orde ionen val te gebruiken, waar de potentiaal (en dus de microbeweging) bijna verdwijnt in het midden van de val [79, 157]. Nadeel is dat de ionen niet gelokaliseerd zijn in zo een opstelling. Aangezien de toepassingen die wij op het oog hebben uitgaan van sterk gelokaliseerde ionen, is dit geen optie in onze opstelling.

Een derde potentiële oplossing voor opwarming door microbeweging is voorgesteld door onze groep [43, 158]. Hier worden de atomen waarmee het ion wisselwerkt optisch gekoppeld met Rydberg toestanden. Dit zorgt in theorie voor een enorme toename in interactie sterkte tussen de atomen en ionen aangezien de Rydberg toestanden een veel grotere polariseerbaarheid hebben. Hierdoor wordt de interactie lengte opgeblazen tot het micrometer niveau en kan de interactie zelfs afstotend gemaakt worden. Met deze setup kunnen in principe rechtstreekse botsingen voorkomen worden waardoor het systeem niet

opwarmt, ongeacht de massa verhouding. Een nadeel is dat meer infrastructuur nodig is in de vorm van Rydberg lasers en dat te sterke koppeling met de Rydberg toestanden tot ionisatie kan leiden. Dit systeem zal experimenteel onderzocht worden in Ref. [159].

We concluderen dat onze experimentele opstelling goed kan zijn om atoom-ionen dynamica in het quantum regime te bestuderen [54]. Het zal mij een groot plezier doen als het systeem uiteindelijk gebruikt kan worden om magnetische Feshbach resonanties waar te nemen tussen atomen en ionen, zoals voorspeld in Ref. [63], en om ultrakoude chemische reacties te bestuderen op het één-deeltjes niveau, en uiteindelijk om de voorgestelde quantum simulator [32] te implementeren.



# A — Yb<sup>+</sup>

state	configuration	level (cm <sup>-1</sup> )	lifetime $\tau$
<sup>2</sup> S <sub>1/2</sub>	(4 <i>f</i> <sup>14</sup> )(6 <i>s</i> )	0.00	—
<sup>2</sup> P <sub>1/2</sub>	(4 <i>f</i> <sup>14</sup> )(6 <i>p</i> )	27061.82	8.07(9) ns [120]
<sup>2</sup> P <sub>3/2</sub>	(4 <i>f</i> <sup>14</sup> )(6 <i>p</i> )	30392.23	6.15(9) ns [120]
<sup>2</sup> D <sub>3/2</sub>	(4 <i>f</i> <sup>14</sup> )(5 <i>d</i> )	22960.8	52.7(24) ms [160, 161]
<sup>2</sup> D <sub>5/2</sub>	(4 <i>f</i> <sup>14</sup> )(5 <i>d</i> )	24332.69	7.2(3) ms [127]
<sup>3</sup> D[3/2] <sub>1/2</sub>	(4 <i>f</i> <sup>13</sup> )(5 <i>d</i> )(6 <i>s</i> )	33653.86	37.7(5) [162]
<sup>2</sup> F <sub>7/2</sub>	(4 <i>f</i> <sup>13</sup> )(6 <i>s</i> ) <sup>2</sup>	21418.75	~ 10 yr [163]
<sup>2</sup> F <sub>5/2</sub>	(4 <i>f</i> <sup>13</sup> )(6 <i>s</i> ) <sup>2</sup>	31568.08	not relevant
<sup>1</sup> D[5/2] <sub>5/2</sub>	(4 <i>f</i> <sup>13</sup> )(5 <i>d</i> )(6 <i>s</i> )	37077.59	not relevant

**Table A.1:** Shell configurations, energy levels and lifetimes of the states of interest in Yb<sup>+</sup>. Unless otherwise stated, the data is taken from Ref. [148].

transition	$\lambda$ (nm)	$\Delta E/h$ (THz)
<sup>2</sup> S <sub>1/2</sub> → <sup>2</sup> P <sub>1/2</sub>	369.52	811.29
<sup>2</sup> S <sub>1/2</sub> → <sup>2</sup> P <sub>3/2</sub>	329.03	911.14
<sup>2</sup> S <sub>1/2</sub> → <sup>2</sup> D <sub>5/2</sub>	411.97	729.48
<sup>2</sup> D <sub>3/2</sub> → <sup>3</sup> D[3/2] <sub>1/2</sub>	935.19	320.57
<sup>2</sup> F <sub>7/2</sub> → <sup>1</sup> D[5/2] <sub>5/2</sub>	638.62	469.44

**Table A.2:** Relevant transitions in Yb<sup>+</sup>. Data taken from Ref. [148].

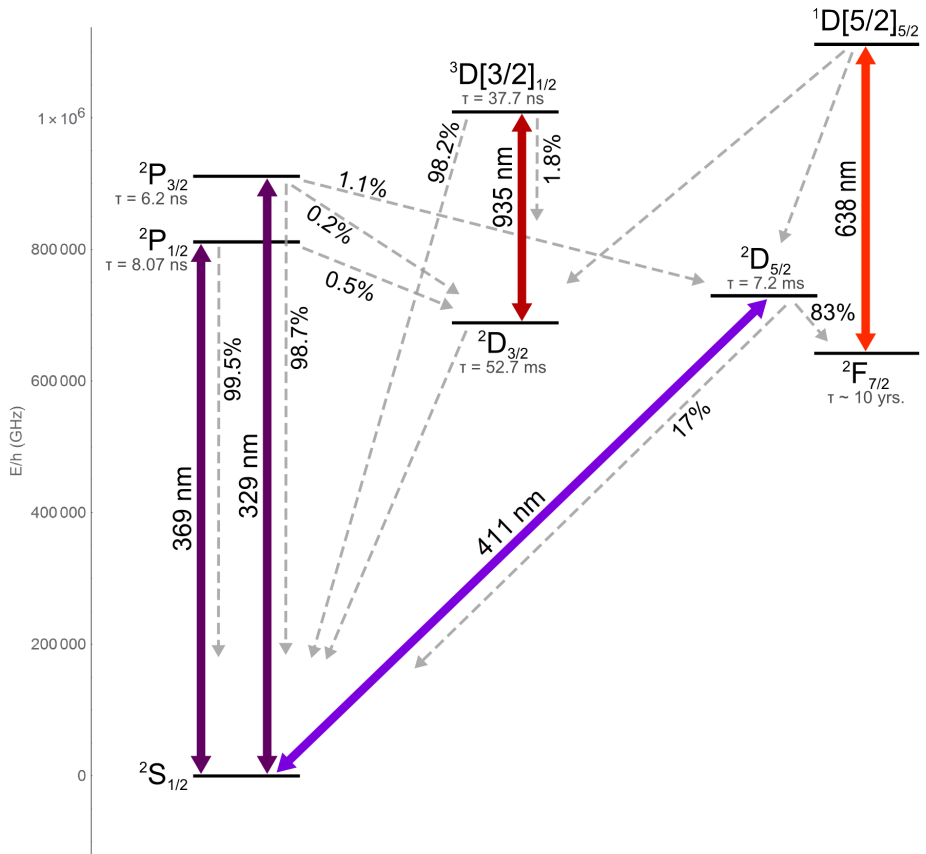


**Figure A.1:** Scheme of the relevant energy levels in Yb<sup>+</sup> (to scale) [148]. Branching ratios for the states  $^2P_{1/2}$ ,  $^2P_{3/2}$ ,  $^3D[3/2]_{1/2}$  and  $^2D_{5/2}$  taken from Ref. [128], [164], [165] and [127], respectively.

isotope	nuclear spin $I$	frequency shift relative to $^{174}\text{Yb}$ (MHz)
$^{176}\text{Yb}$	0	-509.3
$^{173}\text{Yb}$ (F=5/2)	5/2	-253.1
$^{174}\text{Yb}$	0	0
$^{173}\text{Yb}$ (F=3/2)	5/2	516.0
$^{172}\text{Yb}$	0	533.3
$^{173}\text{Yb}$ (F=7/2)	5/2	588.0
$^{171}\text{Yb}$ (F=3/2)	1/2	832.4
$^{171}\text{Yb}$ (F=1/2)	1/2	1153.7
$^{170}\text{Yb}$	0	1192.4
$^{168}\text{Yb}$	0	1187.4

**Table A.3:** Isotope shift for the  $^1\text{S}_0 \rightarrow ^1\text{P}_1$  transition of neutral Yb, with  $^{174}\text{Yb}$  as reference (taken from Ref. [124]).

isotope	PI <sup>i</sup>	D1	D2	Repump	Re-Repump
$^{176}\text{Yb}^+$	751.52571	811.28974	455.567084	320.57423	469.436719
$^{174}\text{Yb}^+$	751.52622	811.29097	455.567623	320.57175	469.43886
$^{172}\text{Yb}^+$	751.52673	811.29223	455.568200	320.56914	469.44114
$^{171}\text{Yb}^+$	751.52703	811.28853	455.566567	320.56903	469.444925
$^{170}\text{Yb}^+$	751.52744	811.29384	455.568920	320.56564	469.444075
$^{168}\text{Yb}^+$	751.52808	811.29556	455.56969	320.56193	469.44722

<sup>i</sup> Photoionization of neutral Yb.

**Table A.4:** Transition frequencies for multiple isotopes of  $\text{Yb}^+$  measured with our experimental setup (in THz). Due to additional AOMs the measured D1 frequency is shifted by  $-205$  MHz and the Repumper transition is shifted by  $-80$  MHz from the frequency at the  $\text{Yb}^+$  ions (see chapter 4.9.1).



# B — ${}^6\text{Li}$

state	configuration	$\Delta E/h$ (THz)	lifetime $\tau$
${}^2\text{S}_{1/2}$	$(1s^2)(2s)$	0.00	—
${}^2\text{P}_{1/2}$	$(1s^2)(2p)$	446.800486	27.102 ns [122]
${}^2\text{P}_{3/2}$	$(1s^2)(2p)$	446.810679	27.102 ns [122]

**Table B.1:** Shell configurations, energy levels and lifetimes of the states of interest in Li I. Unless otherwise stated, the data is taken from Ref. [148].

transition	$\lambda$ (nm)	$\Delta E/h$ (THz)
${}^2\text{S}_{1/2} \rightarrow {}^2\text{P}_{1/2}$	670.992	446.789670
${}^2\text{S}_{1/2} \rightarrow {}^2\text{P}_{3/2}$	670.978	446.799448

**Table B.2:** Transition frequencies for  ${}^6\text{Li}$  measured with our experimental setup. Due to an AOM the measured frequency is shifted by +100 MHz from the frequency at the  ${}^6\text{Li}$  atoms (see chapter 4.9.2).

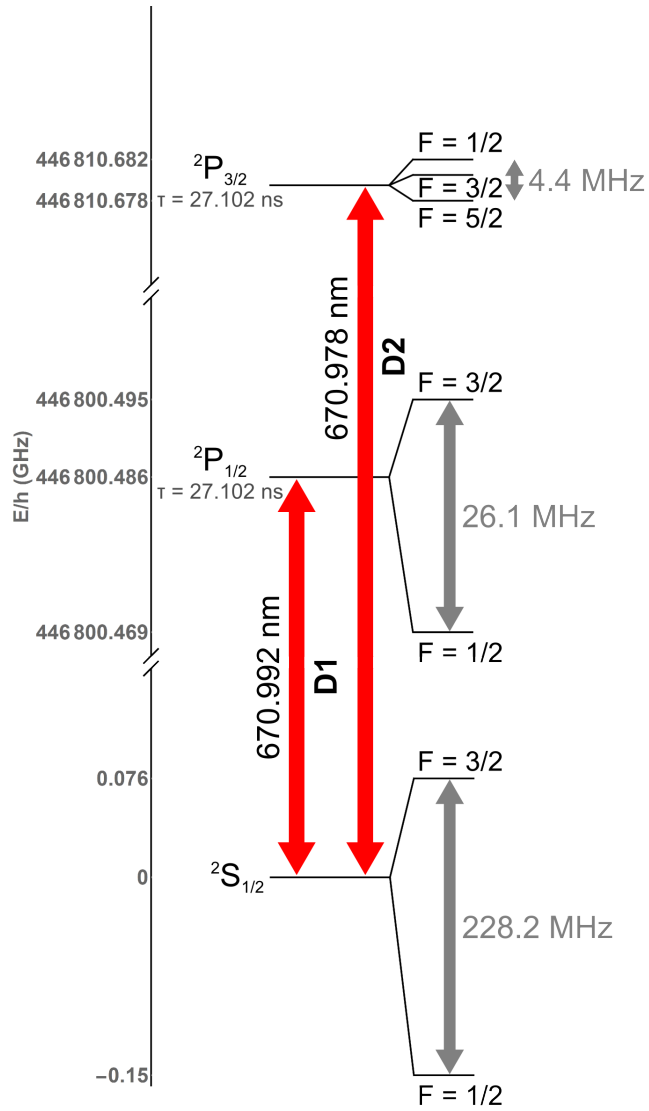


**Figure B.1:** Scheme of the relevant energy levels in  ${}^6\text{Li}$  [122, 148].

# C — Construction manual of the ion trap

The ion trap was designed and built in the Institute of Physics at the University of Mainz (Germany) and in the corresponding in-house workshop. The design is in a manner such that the main parts, namely the mount (see chapter 4.4.4), blade electrodes (see chapter 4.4.1) and end cap electrodes (see chapter 4.4.2) are made out of a single piece of stainless steel. After the metal block has been brought to the correct shape a cylinder is cut out of it from which subsequently the two blade pairs and the end caps are carved out. This ensures highest precision in fitting and alignment.

Before the ion trap is assembled all parts have to be cleaned to avoid contaminations of the vacuum system. For this purpose, it is advisable to take the following steps: First, the part is cleaned with a residue-free soap before being drained thoroughly with distilled water. Subsequently, it is cleaned in an ultrasonic bath with isopropanol and maybe afterwards even with acetone.

The assembly has to be done in a clean room in order to prevent contaminations. The construction manual is as follows:

1. Build a surface for the feedthrough flange to stand upright without bending the electrical connector wires.
2. Place a oxygen-free copper gasket at the knife-edge of the feedthrough flange.
3. Position the mount and screw it tightly using in-vacuum screws.
4. Fit the corresponding isolators to the blade electrodes.

5. Fit one of the blade electrodes with isolator into the mount and fix it at the back with a small clamp screwed on the mount.
6. Rotate the assembly such that the mounted blade electrode is at the bottom pointing upwards.
7. Use clean tweezers to put the four spherical, insulating spacers into the small cavities in the blade electrode.
8. Fit the remaining blade electrode in the setup such that the spacers are in its cavities and fix it with a clamp.
9. Rotate the assembly back to the upright orientation.
10. Fit the corresponding isolators to the end cap electrodes.
11. Fit the end cap electrodes with isolators into the blade electrodes.
12. Attach the electrical connectors to the blade electrodes and end caps.
13. Attach the isolations and clamps on the end cap electrodes, pressing both blade-end cap assemblies onto each other.
14. Demount the two clamps attached in steps 5 and 8.
15. Fit the compensation electrodes with isolations.
16. Fit the coil wire.
17. Attach the Yb oven (see chapter 4.4.3).
18. Do the wiring.
19. Attach the MOT mirror (see chapter 4.4.4).
20. Check the electrical connections.
21. Relax and enjoy a cold drink.

## D — Construction manual of the Feshbach coils

The design of our Feshbach coils was adapted from the advanced design developed in the group of Prof. Selim Jochim at the University of Heidelberg. The detailed description of the design and a construction manual (in German) can be found in Ref. [113]. We slightly changed the design in order to make the coils fit into our setup.

Here, we give a short manual of the coil building procedure as it slightly deviates from the procedure being applied in Heidelberg:

1. **Coil winding preparation:** For decent coil winding it is convenient to use a lathe. It has to be turned off and needs to be manually switchable between locked and running idle. Clamp the bottom part of the home-made coil-profile onto the locked lathe with the Teflon surface pointing to the front. Clean the coil wire and prepare an adequate amount of epoxy (EPO-TEK® 353ND).
2. **Coil winding:** Clamp the end of the wire onto the coil-profile and slightly attach the top cover of the coil-profile such that the wire can only just move in between. Put the lathe to running idle. Start winding by rotating the coil-profile while brushing the wire with epoxy. Always hold the wire tight and straight in order to minimize the distance between the single loops. After winding a few more windings then necessary lock the lathe and fix the wire with clamps and by tightening the screws of the coil-profile top cover. Cut the coil wire from the wound coil.
3. **Coil curing:** Cure the coil according to instructions manual of the epoxy for one hour in an oven pre-heated to 150°C. For this purpose, monitor

the coil temperature at the core.

4. **Coil preparation:** Demount the coil-profile top cover. Bring the coil-profile assembly to the workshop to have the upper insulating coating of the coil wire be removed (with a lathe). This has to be done with great caution such that as little as possible wire material is removed. Afterwards, demount the coil from the profile, cut the extra wire. Use sandpaper in order to remove the coating at the intended contact surfaces between the coil and connector. Clean the coil and coat the contact surfaces with solder.
5. **Heat sink preparation:** Clean the heat sink and place it on the home-made mount. Prepare an adequate amount of epoxy (EPO-TEK<sup>®</sup> T905BN-3). Apply as much epoxy onto the bottom surface of the heat sink such that it is only just covered everywhere.
6. **Attaching the coil to the heat sink:** Very carefully fit the coil onto the heat sink and use the stamp of the home-made mount to tightly press it onto the surface. During this procedure always measure for shorts between the coil and heat sink.
7. **Attaching the electrical connectors:** Coat the surfaces of the connectors which will be in contact with the heat sink with epoxy (EPO-TEK<sup>®</sup> T905BN-3). Very carefully fit the connectors onto the correct position and slightly fix them with clamps. Check the electrical connections and measure for shorts between the coil and heat sink.
8. **Curing:** Cure the epoxy for one hour at 80°C and for one additional hour at 120°C.
9. **Establish electrical connection:** Use a burner and a soldering iron to finalize the soldering between the coil and connector. Check the electrical connections and measure for shorts between the coil and heat sink.
10. **Quality check:** First turn on water cooling and check for water leaks at the heat sink and the water connections. Then very carefully measure the resistance and temperature rise at the single connections in dependence to the applied current. **BE EXTREMELY CAREFUL AT HIGH CURRENTS!**

## E — Optical reference cavity

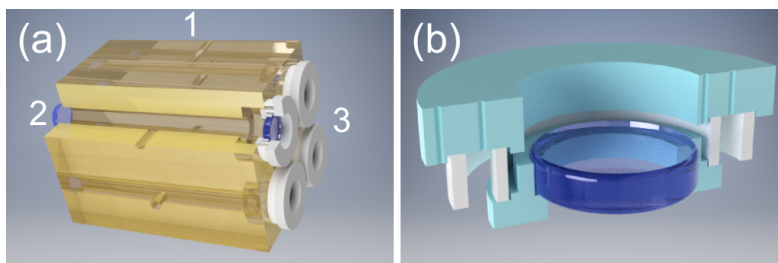


**Figure E.1:** Sectional drawings of the optical reference cavity. (a) Zerodur-block (1) with mounted mirrors (2) and (3). It features multiple single cavities for simultaneous locking of four laser systems. (b) Design of the plano-concave mirror and ring-shaped piezo elements assembly (3) (for more informations on the single components see chapter 4.9.3).

The design of the optical reference cavity as shown in figure E.1 is the commonly used design in our former working group by Prof. Schmidt-Kaler in Mainz. As implied in figure 4.31 it is built into a small vacuum system<sup>12345</sup>. The flange serving as a mirror mount for the entrance windows, which are under an angle of  $5^\circ$  to the beam path, is home-made.

<sup>1</sup>Hositrاد, Reducer Tee, Flange Major NW100CF Minor NW35CF.

<sup>2</sup>Hositrاد, Cross Reducer 4-Way, Flange Major NW35CF Minor NW16CF.

<sup>3</sup>Hositrاد, Viewport Zero-Length Glass, Flange NW100CF.

<sup>4</sup>VAT, 54124-GE02-0001, Easy Close All-metal Angle Valve, DN16 CF.

<sup>5</sup>Agilent, 9190520,2 l/s ion pump with Mini CF flange.



## F — Correction of interaction time for the ${}^2F_{7/2}$ state

The preparation of the ions in the  ${}^2F_{7/2}$  state relies on the decay of the metastable  ${}^2D_{5/2}$  state and thus takes much longer than for the  ${}^2P_{1/2}$  and  ${}^2D_{3/2}$  state. Therefore, we prepare the  ${}^2F_{7/2}$  state before the MOT loading stage. Thus, the atoms already interact with the ions while being elevated into the interaction zone. We take this into account by calculating an effective interaction time, given by

$$\tau_F = \tau_{F,0} + \tau_{F,\text{corr}} , \quad (\text{F.1})$$

consisting of the bare interaction time  $\tau_{F,0} = 25$  ms, set in the experimental control software, and an additional term

$$\tau_{F,\text{corr}} = 2 \int_0^{T_{\text{ver}}} e^{-\frac{(h-z_{\text{min}}(t))^2}{2\sigma_{\text{vert}}^2}} dt , \quad (\text{F.2})$$

consisting of the integral of the approaching atom cloud's vertical density profile being elevated by the trap minimum's trajectory  $z_{\text{min}}(t)$  to the vertical position  $h$  of the ion. The factor 2 accounts for the transport back. For the measured vertical cloud size of  $\sigma_{\text{vert}} = 410(40)$   $\mu\text{m}$ , we get  $\tau_{F,\text{corr}} = 14(1)$  ms and therefore an effective interaction time of  $39(1)$  ms.



# Acknowledgments

In course of setting up the experimental setup, conducting the experiments and preparing this thesis I experienced substantial support by many people. First of all I want to mention my co-promoter, mentor, adviser, guide and friend Rene Gerritsma. Thank you for putting your trust in me. I already miss our debates with a good glass of Zötler/Zatte and I hope to see you and Evelien from time to time in the coming years. I also want to thank my promoter Florian Schreck who always has an open ear for his students and who was a big support during our move to Amsterdam.

Setting up a completely new experiment requires much time and patience as well as enthusiasm and a lot of confidence. And most of all it is a team game. I had the great luck to be accompanied by my fellow PhD student Henning Fürst, who took care of the *atomic* part of the setup as well as on the experimental control and many many many many things more. Next to Rene, he is the main reason why I could finish my thesis in time and I'm eternally grateful. I wish you all the best and a great career (hopefully in science)! Later on, our team was strengthened with Norman Ewald who first did his Master's thesis in our group before joining us as a PhD student. He helped us setting up the experiment which he did with best possible accuracy. I wish you many fascinating results on the Rydberg system. Now I have to cite Rene who wrote in the acknowledgments of his PhD thesis: *"Post-docs are very important to an experiment and we were lucky to get a very good one. Thomas"* Feldker, who did his PhD in Mainz, joined our group when we had just trapped and overlapped atoms and ions. His physical and technical knowledge and experience gave a real boost to the future development of our experiment and now we reach for the quantum regime. I also would like to acknowledge Thomas Secker who joined us for some months doing fascinating theoretical calculations on the atom-ion system and who introduced me to the fitness center next door, and Antonio

Negretti as well as Michał Tomza, our collaborators for the work described in chapter 3 and chapter 7, respectively, and further on.

We started this project at the University of Mainz. Being included in the working group *Quantenbit* headed by Prof. Schmidt-Kaler<sup>1</sup>, we had access to immense knowledge and know-how regarding state-of-the-art ion trapping and experimental control. I want to personally thank Ferdinand Schmidt-Kaler for his counsel, Kilian Singer for introducing me to ion trap simulations and Johannes Roßnagel to supply me with his design of the heat engine, which served as a model for our ion trap. As well as Ulrich Poschinger, Christian Schmiegelow, Max Hettrich, Georg Jakob, Vidyut Kaushal, Sebastian Wolf, Thomas Ruster, Henning Kaufmann and Marcel Salz for their help, advise and company during the whole build-up phase. In Mainz we also experienced great support from Christine Best and Elvira Stuck-Kerth putting the whole working group on a solid foundation. I also want to thank Kim Truong who had to execute an immense number of orders and Anton Gläser who conscientiously accepted all deliveries. The institutes' own mechanical workshop, headed by highly experienced Siegbert Felzer, built our ion trap and also countless various parts of the experimental setup with highest precision for an incredibly low price.

The experiment would not have been realized that way it did without the help of the *Ultracold Quantum Gases Group* at the Heidelberg University headed by Prof. Selim Jochim. They not only openly shared their profound knowledge of lithium traps but also supported us with technical drawings of their highly advanced setup. I want to personally thank Gerhard Zürn who was my contact person during this episode and who was extremely helpful.

In March 2016 our whole experiment and atom-ion working group was transferred to the University of Amsterdam where we have been kindly integrated into the *Quantum Gases and Quantum Information group*. Here, we experience great support by Ben van Linden van den Heuvell, Florian Schreck, Robert Spreeuw, Klassjan van Druten, Tom Hijmans, Jook Walraven and their teams of PhD students and post-docs. The smooth move was made possible by Joost van Mameren, Natalie Wells, Anne-Marieke Crommentuijn, Hugo Schlatter, Wim van Aartsen, Alix Wattjes and many more.

At last some personal acknowledgments: In Amsterdam the PhD students and post-docs form a great community. This helped me a lot to have a good time even though being separated from Kerstin. Thanks to all of you!

During my time as a student and also as a PhD student my parents have always been a big support. Special thanks go to my dad who, as a professor for

---

<sup>1</sup>[www.quantenbit.de](http://www.quantenbit.de)

biology, proofread the whole thesis and came up with some great suggestions for improvements.

And once again my thanks go to Rene, as he gave me the possibility to write this thesis from at home in Germany such that I could be with the two most important women in my life.

When I began my PhD, Kerstin was my girlfriend and now at the very end of it she is my wife and we have a wonderful child, Charlotte. I'm deeply grateful! Kerstin, especially the time I was in Amsterdam was hard for you. But you did not complain, even then when the date of birth drew near. To you my love I dedicate this thesis.

And thank you Charlotte for being the sweetest distraction while preparing this thesis and for your contagious enthusiasm to discover this world.



# List of publications

## Publications presented in this thesis

*Quantum dynamics of an atomic double-well system interacting with a trapped ion*

J. Joger, A. Negretti and R. Gerritsma

Phys. Rev. A **89**, 063621 (2014)

*Observation of collisions between cold Li atoms and  $Yb^+$  ions*

J. Joger, H. Fürst, N. V. Ewald, T. Feldker, M. Tomza and R. Gerritsma

Phys. Rev. A **96**, 030703(R) (2017)

## Related publications of the Hybrid atom-ion Quantum Systems group

*Trapped ions in Rydberg-dressed atomic gases*

T. Secker, N. V. Ewald, J. Joger, H. Fürst, T. Feldker and R. Gerritsma

Phys. Rev. Lett. **118**, 263201 (2017)

*Spectroscopy of the  $S1/2 \rightarrow P3/2$  transition in Yb II: Isotope shifts, hyperfine splitting and branching ratios*

T. Feldker, H. Fürst, N. V. Ewald, J. Joger and R. Gerritsma

Phys. Rev. A **97**, 032511 (2018)

*Dynamics of a single ion spin impurity in a spin-polarized atomic bath*

H. Fürst, T. Feldker, N. V. Ewald, J. Joger, M. Tomza and R. Gerritsma

arXiv:1712.07873 (2017)

*Prospects of reaching the quantum regime in Li- $Yb^+$  mixtures*

H. A. Fürst, N. V. Ewald, T. Secker, J. Joger, T. Feldker and R. Gerritsma

arXiv:1804.04486 (2018)



# Acronyms

**ac** alternating current

**AR** antireflective

**AOM** acousto-optic modulator

**BEM** Boundary Element Method

**cMOT** compressed MOT

**COM** center of mass

**dc** direct current

**ECDL** external-cavity diode laser

**EOM** electro-optic modulator

**FSR** free spectral range

**FWHM** full width at half maximum

**HV** high voltage

**LD** laser diode

**LO** local oscillator

**MM** micromotion

**mMOT** mirror MOT

**MOT** magneto optical trap

**MW** microwave  
**NA** numerical aperture  
**ODT** optical dipole trap  
**OI** optical isolator  
**PBS** polarizing beam splitter  
**PD** photodiode  
**PDH** Pound-Drever-Hall  
**PID** proportional–integral–derivative  
**PMT** Photomultiplier tube  
**PR** partial reflection  
**QDT** quantum defect theory  
**rf** radio frequency  
**ROC** radius of curvature  
**SHG** second harmonic generation  
**TA** tapered semiconductor amplifier  
**TEM** transverse electromagnetic mode  
**TSP** titanium sublimation pump  
**UHV** ultra-high vacuum

# Bibliography

- [1] S. A. Diddams, Th. Udem, J. C. Bergquist, E. A. Curtis, R. E. Drullinger, L. Hollberg, W. M. Itano, W. D. Lee, C. W. Oates, K. R. Vogel, and D. J. Wineland. An optical clock based on a single trapped  $^{199}\text{Hg}^+$  ion. *Science*, 293:825–828, 2001.
- [2] D.J. Wineland, J.C. Bergquist, J.J. Bollinger, R.E. Drullinger, and W.M. Itano. Quantum computers and atomic clocks. In *Proc. 6th Symposium on Frequency Standards and Metrology, St. Andrews, Scotland, Sept. 9 - 14, 2001.*, pages 361–368, Singapore, 2001. World Scientific.
- [3] J. I. Cirac and P. Zoller. Quantum computations with cold trapped ions. *Phys. Rev. Lett.*, 74(20):4091–4094, 1995.
- [4] R. Blatt and D. Wineland. Entangled states of trapped atomic ions. *Nature*, 453:1008–1015, 2008.
- [5] H. Häffner, C.F. Roos, and R. Blatt. Quantum computing with trapped ions. *Physics Reports*, 469:155, 2008.
- [6] K. Singer, U. Poschinger, M. Murphy, P. Ivanov, F. Ziesel, T. Calarco, and F. Schmidt-Kaler. Colloquium: Trapped ions as quantum bits: Essential numerical tools. *Reviews of Modern Physics*, 82:2609–2632, 2010.
- [7] R. Blatt and C. F. Roos. Quantum simulations with trapped ions. *Nat. Phys.*, 8:277, 2012.
- [8] Andrew D. Ludlow, Martin M. Boyd, Jun Ye, E. Peik, and P. O. Schmidt. Optical atomic clocks. *Rev. Mod. Phys.*, 87:637–701, 2015.

- [9] Stefan Willitsch. Coulomb-crystallised molecular ions in traps: methods, applications, prospects. *International Reviews in Physical Chemistry*, 31(2):175–199, 2012.
- [10] D. Leibfried, R. Blatt, C. Monroe, and D. Wineland. Quantum dynamics of single trapped ions. *Rev. Mod. Phys.*, 75:281, 2003.
- [11] A. Bermudez, X. Xu, R. Nigmatullin, J. O’Gorman, V. Negnevitsky, P. Schindler, T. Monz, U. G. Poschinger, C. Hempel, J. Home, F. Schmidt-Kaler, M. Biercuk, R. Blatt, S. Benjamin, and M. Müller. Assessing the progress of trapped-ion processors towards fault-tolerant quantum computation. *Phys. Rev. X*, 7:041061, 2017.
- [12] Markus Greiner, Olaf Mandel, Tilman Esslinger, Theodor W. Hänsch, and Immanuel Bloch. Quantum phase transition from a superfluid to a Mott insulator in a gas of ultracold atoms. *Nature*, 415(6867):39–44, 2002.
- [13] M. H. Anderson, J. R. Ensher, M. R. Matthews, C. E. Wieman, and E. A. Cornell. Observation of Bose-Einstein condensation in a dilute atomic vapor. *Science*, 269(5221):198–201, 1995.
- [14] B. DeMarco and D. S. Jin. Onset of Fermi degeneracy in a trapped atomic gas. *Science*, 285:1703, 1999.
- [15] Jean Dalibard. Collisional dynamics of ultracold atomic gases. In *Bose-Einstein Condensation in Atomic Gases, Vol. Course CXL of Proceedings of the International School of Physics Enrico Fermi (IOS)*. Press, 1998.
- [16] S. Inouye, M. R. Andrews, J. Stenger, H.-J. Miesner, D. M. Stamper-Kurn, and W. Ketterle. Observation of Feshbach resonances in a Bose-Einstein condensate. *Nature*, 392:151–154, 1998.
- [17] Th. Udem, R. Holzwarth, and T. W. Hänsch. Optical frequency metrology. *Nature*, 416(6877):233–237, 2002.
- [18] C. Monroe. Quantum information processing with atoms and photons. *Nature*, 416:238, 2002.
- [19] Immanuel Bloch, Jean Dalibard, and Sylvain Nascimbène. Quantum simulations with ultracold quantum gases. *Nat. Phys.*, 8:267–276, 2012.

- [20] Rudolf Grimm, Matthias Weidemüller, and Yurii B. Ovchinnikov. Optical dipole traps for neutral atoms. volume 42 of *Advances In Atomic, Molecular, and Optical Physics*, pages 95 – 170. Academic Press, 2000.
- [21] Immanuel Bloch, Jean Dalibard, and Wilhelm Zwerger. Many-body physics with ultracold gases. *Rev. Mod. Phys.*, 80:885, 2008.
- [22] Andrew T. Grier, Marko Cetina, Fedja Oručević, and Vladan Vuletić. Observation of cold collisions between trapped ions and trapped atoms. *Phys. Rev. Lett.*, 102:223201, 2009.
- [23] C. Zipkes, S. Paltzer, C. Sias, and M. Köhl. A trapped ion inside a Bose-Einstein condensate. *Nature*, 464:388, 2010.
- [24] Stefan Schmid, Arne Härter, and Johannes Hecker Denschlag. Dynamics of a cold trapped ion in a Bose-Einstein condensate. *Phys. Rev. Lett.*, 105:133202, 2010.
- [25] Felix H. J. Hall, Mireille Aymar, Nadia Bouloufa-Maafa, Olivier Dulieu, and Stefan Willitsch. Light-assisted ion-neutral reactive processes in the cold regime: Radiative molecule formation versus charge exchange. *Phys. Rev. Lett.*, 107:243202, 2011.
- [26] Wade G. Rellergert, Scott T. Sullivan, Svetlana Kotochigova, Alexander Petrov, Kuang Chen, Steven J. Schowalter, and Eric R. Hudson. Measurement of a large chemical reaction rate between ultracold closed-shell  $^{40}\text{Ca}$  atoms and open-shell  $^{174}\text{Yb}^+$  ions held in a hybrid atom-ion trap. *Phys. Rev. Lett.*, 107:243201, 2011.
- [27] K. Ravi, Seunghyun Lee, Arijit Sharma, G. Werth, and S. A. Rangwala. Cooling and stabilization by collisions in a mixed ion-atom system. *Nat. Commun.*, 3:1126, 2012.
- [28] A. Härter and J. Hecker Denschlag. Cold atom-ion experiments in hybrid traps. *Contemp. Phys.*, 55:33–45, 2014.
- [29] Shinsuke Haze, Ryoichi Saito, Munekazu Fujinaga, and Takashi Mukaiyama. Charge-exchange collisions between ultracold fermionic lithium atoms and calcium ions. *Phys. Rev. A*, 91:032709, 2015.
- [30] Ziv Meir, Tomas Sikorsky, Ruti Ben-shlomi, Nitzan Akerman, Yehonatan Dallal, and Roei Ozeri. Dynamics of a ground-state cooled ion colliding with ultra-cold atoms. *Phys. Rev. Lett.*, 117:243401, 2016.

- [31] H. Doerk, Z. Idziaszek, and T. Calarco. Atom-ion quantum gate. *Phys. Rev. A*, 81:012708, 2010.
- [32] U. Bissbort, D. Cocks, A. Negretti, Z. Idziaszek, T. Calarco, F. Schmidt-Kaler, W. Hofstetter, and R. Gerritsma. Emulating solid-state physics with a hybrid system of ultracold ions and atoms. *Phys. Rev. Lett.*, 111:080501, 2013.
- [33] J. M. Schurer, R. Gerritsma, P. Schmelcher, and A. Negretti. Impact of many-body correlations on the dynamics of an ion-controlled bosonic Josephson junction. *Phys. Rev. A*, 93:063602, 2016.
- [34] Lothar Ratschbacher, Christoph Zipkes, Carlo Sias, and Michael Köhl. Controlling chemical reactions of a single particle. *Nat. Phys.*, 8:649–652, 2012.
- [35] R. Côté and A. Dalgarno. Ultracold atom-ion collisions. *Phys. Rev. A*, 62:012709, 2000.
- [36] Carlo Sias and Michael Köhl. Hybrid quantum systems of atoms and ions. In *Quantum Gas Experiments*, chapter 12, pages 267–291. Imperial College Press, 2014.
- [37] Stefan Willitsch. Ion-atom hybrid systems. In *Ion Traps for Tomorrow's Applications*, volume 189. 2015.
- [38] R. Côté. Chapter Two - Ultracold Hybrid Atom–Ion Systems. volume 65 of *Advances In Atomic, Molecular, and Optical Physics*, pages 67 – 126. Academic Press, 2016.
- [39] D. Zhang and S. Willitsch. Cold ion chemistry. *arXiv:1703.07133*, 2017.
- [40] M. Tomza, K. Jachymski, R. Gerritsma, A. Negretti, T. Calarco, Z. Idziaszek, and P. S. Julienne. Cold hybrid ion-atom systems. *arXiv:1708.07832*, 2017.
- [41] Michal Krych and Zbigniew Idziaszek. Description of ion motion in a Paul trap immersed in a cold atomic gas. *Phys. Rev. A*, 91:023430, 2015.
- [42] C. Kollath, M. Köhl, and T. Giamarchi. Scanning tunneling microscopy for ultracold atoms. *Phys. Rev. A*, 76:063602, 2007.

- [43] T. Secker, R. Gerritsma, A. W. Glaetzle, and A. Negretti. Controlled long-range interactions between Rydberg atoms and ions. *Phys. Rev. A*, 94:013420, 2016.
- [44] M. Brownnutt, M. Kumph, P. Rabl, and R. Blatt. Ion-trap measurements of electric-field noise near surfaces. *Rev. Mod. Phys.*, 87:1419–1482, 2015.
- [45] R. Feynman. Simulating physics with computers. *Int. J. Theoret. Phys.*, 21:467, 1982.
- [46] Wolfgang Paul. Ein Ionenkäfig. In *Forschungsberichte des Wirtschafts- und Verkehrsministeriums Nordrhein-Westfalen*, volume 415. 1958.
- [47] M.G. Raizen, J.M. Gilligan, J.C. Bergquist, W.M. Itano, and D.J. Wineland. Linear trap for high-accuracy spectroscopy of stored ions. *Journal of Modern Optics*, 39(2):233–242, 1992.
- [48] Z. Idziaszek, A. Simoni, T. Calarco, and P. S. Julienne. Multichannel quantum-defect theory for ultracold atom–ion collisions. *New J. Phys.*, 13:083005, 2011.
- [49] L. Huy Nguyen, A. Kalev, M. Barrett, and B.-G. Englert. Micromotion in trapped atom-ion systems. *Phys. Rev. A*, 85:052718, 2012.
- [50] Marko Cetina, Andrew T. Grier, and Vladan Vuletić. Micromotion-induced limit to atom-ion sympathetic cooling in Paul traps. *Phys. Rev. Lett.*, 109:253201, 2012.
- [51] Kuang Chen, Scott T. Sullivan, and Eric R. Hudson. Neutral gas sympathetic cooling of an ion in a Paul trap. *Phys. Rev. Lett.*, 112:143009, 2014.
- [52] B. Höltkemeier, P. Weckesser, H. López-Carrera, and M. Weidemüller. Buffer-gas cooling of ions in a multipole radio frequency trap beyond the critical mass ratio. *Phys. Rev. Lett.*, 116:233003, 2016.
- [53] I. Rouse and S. Willitsch. Superstatistical energy distributions of an ion in an ultracold buffer gas. *Phys. Rev. Lett.*, 118:143401, 2017.
- [54] Henning Füst, Thomas Feldker, Norman V. Ewald, Jannis Joger, and Rene Gerritsma. Prospects of reaching the quantum regime in Li-Yb<sup>+</sup> mixtures. *arXiv:1804.04486*, 2018.

- [55] R. Saito, S. Haze, M. Sasakawa, R. Nakai, M. Raoult, H. Da Silva, O. Dulieu, and T. Mukaiyama. Characterization of charge-exchange collisions between ultracold  ${}^6\text{Li}$  atoms and  ${}^{40}\text{Ca}^+$  ions. *Phys. Rev. A*, 95:032709, 2017.
- [56] Scott T. Sullivan, Wade G. Rellergert, Svetlana Kotochigova, and Eric R. Hudson. Role of electronic excitations in ground-state-forbidden inelastic collisions between ultracold atoms and ions. *Phys. Rev. Lett.*, 109:223002, 2012.
- [57] D. S. Goodman, J. E. Wells, J. M. Kwolek, R. Blümel, F. A. Narducci, and W. W. Smith. Measurement of the low-energy  $\text{Na}^+$ – $\text{Na}$  total collision rate in an ion-neutral hybrid trap. *Phys. Rev. A*, 91:012709, 2015.
- [58] W.W. Smith, D.S. Goodman, I. Sivarajah, J.E. Wells, S. Banerjee, R. Cote, H.H. Michels, Jr. Mongtomery, J.A., and F.A. Narducci. Experiments with an ion-neutral hybrid trap: cold charge-exchange collisions. *Appl. Phys. B*, 114:75, 2014.
- [59] Sourav Dutta, Rahul Sawant, and S. A. Rangwala. Collisional cooling of light ions by cotrapped heavy atoms. *Phys. Rev. Lett.*, 118:113401, 2017.
- [60] A. Negretti, R. Gerritsma, Z. Idziaszek, F. Schmidt-Kaler, and T. Calarco. Generalized Kronig-Penney model for ultracold atomic quantum systems. *Phys. Rev. B*, 90:155426, 2014.
- [61] R. Gerritsma, A. Negretti, H. Doerk, Z. Idziaszek, T. Calarco, and F. Schmidt-Kaler. Bosonic Josephson junction controlled by a single trapped ion. *Phys. Rev. Lett.*, 109:080402, 2012.
- [62] Jannis Joger. Development and characterisation of a combined atom-ion micro trap. Diploma thesis, University Mainz, 2013.
- [63] Michal Tomza, Christiane P. Koch, and Robert Moszynski. Cold interactions between an  $\text{Yb}^+$  ion and a Li atom: Prospects for sympathetic cooling, radiative association, and Feshbach resonances. *Phys. Rev. A*, 91:042706, 2015.
- [64] Humberto da Silva Jr, Maurice Raoult, Mireille Aymar, and Olivier Dulieu. Formation of molecular ions by radiative association of cold trapped atoms and ions. *New Journal of Physics*, 17(4):045015, 2015.

- [65] Z. Idziaszek, T. Calarco, and P. Zoller. Controlled collisions of a single atom and an ion guided by movable trapping potentials. *Phys. Rev. A*, 76:033409, 2007.
- [66] Z. Idziaszek, T. Calarco, P. S. Julienne, and A. Simoni. Quantum theory of atom-ion collisions. *Phys. Rev. A*, 79:010702(R), 2009.
- [67] Christoph Zipkes, Lothar Ratschbacher, Carlo Sias, and Michael Köhl. Kinetics of a single trapped ion in an ultracold buffer gas. *New J. Phys.*, 13, 2010.
- [68] Michał Krych, Wojciech Skomorowski, Filip Pawłowski, Robert Moszynski, and Zbigniew Idziaszek. Sympathetic cooling of the  $\text{Ba}^+$  ion by collisions with ultracold Rb atoms: Theoretical prospects. *Phys. Rev. A*, 83:032723, 2011.
- [69] Bogumil Jeziorski, Robert Moszynski, and Krzysztof Szalewicz. Perturbation theory approach to intermolecular potential energy surfaces of van der Waals complexes. *Chemical Reviews*, 94(7):1887–1930, 1994.
- [70] H. Haken and H. C. Wolf. *Molecular Physics and Elements of Quantum Chemistry*. Springer Berlin Heidelberg, 2004.
- [71] Jacob N. Israelachvili. *Intermolecular and surface forces*. Academic Press London; San Diego, 2nd ed. edition, 1991.
- [72] P. Langevin. A fundamental formula of kinetic theory. *Ann. Chim. Phys.*, 5:245–288, 1905.
- [73] George Gioumousis and D. P. Stevenson. Reactions of gaseous molecule ions with gaseous molecules. v. theory. *The Journal of Chemical Physics*, 29(2):294–299, 1958.
- [74] W. Paul. Electromagnetic traps for charged and neutral particles. *Rev. Mod. Phys.*, 62:531–540, 1990.
- [75] G. Birkl, S. Kassner, and H. Walther. Multiple-shell structures of laser-cooled  $^{24}\text{Mg}^+$  ions in a quadrupole storage ring. *Nature*, 357:310–313, 1992.
- [76] D. J. Berkeland, J. D. Miller, J. C. Bergquist, W. M. Itano, and D. J. Wineland. Minimization of ion micromotion in a Paul trap. *J. App. Phys.*, 83(10):5025–5033, 1998.

- [77] F. G. Major and H. G. Dehmelt. Exchange-collision technique for the RF spectroscopy of stored ions. *Phys. Rev.*, 170:91–107, 1968.
- [78] R. G. DeVoe. Power-law distributions for a trapped ion interacting with a classical buffer gas. *Phys. Rev. Lett.*, 102:063001, 2009.
- [79] Bastian Höltkemeier, Pascal Weckesser, Henry López-Carrera, and Matthias Weidemüller. Buffer-gas cooling of a single ion in a multipole radio frequency trap beyond the critical mass ratio. *Phys. Rev. Lett.*, 116:233003, 2016.
- [80] Steven Schowalter, Alexander Dunning, Kuang Chen, Prateek Puri, Christian Schneider, and Eric R. Hudson. Blue-sky bifurcation of ion energies and the limits of neutral-gas sympathetic cooling of trapped ions. *Nature Communications*, 7:12448, 2016.
- [81] I. Rouse and S. Willitsch. Superstatistical energy distributions of an ion in an ultracold buffer gas. *Phys. Rev. Lett.*, 118:143401, 2017.
- [82] J. Joger, A. Negretti, and R. Gerritsma. Quantum dynamics of an atomic double-well system interacting with a trapped ion. *Phys. Rev. A*, 89:063621, 2014.
- [83] T. Calarco, U. Dorner, P. S. Julienne, C. J. Williams, and P. Zoller. Quantum computations with atoms in optical lattices: Marker qubits and molecular interactions. *Phys. Rev. A*, 70:012306, 2004.
- [84] M. Krych and Z. Idziaszek. Controlled collisions of two ultracold atoms in separate harmonic traps. *Phys. Rev. A*, 80:022710, 2009.
- [85] M. Albiez, R. Gati, J. Fölling, S. Hunsmann, M. Cristiani, and M. Oberthaler. Direct observation of tunneling and nonlinear self-trapping in a single bosonic Josephson junction. *Phys. Rev. Lett.*, 95:010402, 2005.
- [86] Ingrid Bausmerth, Uwe R. Fischer, and Anna Posazhennikova. Quantum top inside a Bose-Einstein-condensate Josephson junction. *Phys. Rev. A*, 75:053605, 2007.
- [87] Uwe R. Fischer, Christian Iniotakis, and Anna Posazhennikova. Coherent single atom shuttle between two Bose-Einstein condensates. *Phys. Rev. A*, 77:031602(R), 2008.

- [88] R. Gati and M. K. Oberthaler. A bosonic Josephson junction. *J. Phys. B: At. Mol. Opt. Phys.*, 40:R61, 2007.
- [89] S. Levy, E. Lahoud, I. Shomroni, and J. Steinhauer. The a.c. and d.c. Josephson effects in a Bose-Einstein condensate. *Nature*, 449:579–583, 2007.
- [90] L. J. LeBlanc, A. B. Bardou, J. McKeever, M. H. T. Extavour, D. Jervis, J. H. Thywissen, F. Piazza, and A. Smerzi. Dynamics of a tunable superfluid junction. *Phys. Rev. Lett.*, 106:025302, 2011.
- [91] I. Bouchoule. Modulational instabilities in Josephson oscillations of elongated coupled condensates. *Eur. Phys. J. D*, 35:147, 2005.
- [92] T. Betz, S. Manz, R. Bücke, T. Berrada, Ch. Koller, G. Kazakov, I. E. Mazets, H.-P. Stimming, A. Perrin, T. Schumm, and J. Schmiedmayer. Two-point phase correlations of a one-dimensional bosonic Josephson junction. *Phys. Rev. Lett.*, 106:020407, 2011.
- [93] A. Eckardt, T. Jinasundera, C. Weiss, and M. Holthaus. Analog of photon-assisted tunneling in a Bose-Einstein condensate. *Phys. Rev. Lett.*, 95:200401, 2005.
- [94] Julian Grond, Thomas Betz, Ulrich Hohenester, Norbert J. Mauser, Joerg Schmiedmayer, and Thorsten Schumm. The Shapiro effect in atomchip-based bosonic Josephson junctions. *New J. Phys.*, 13:065026, 2011.
- [95] Nir Bar-Gill, Christian Gross, Igor Mazets, Markus Oberthaler, and Gershon Kurizki. Einstein-Podolsky-Rosen correlations of ultracold atomic gases. *Phys. Rev. Lett.*, 106:120404, 2011.
- [96] Q. Y. He, M. D. Reid, T. G. Vaughan, C. Gross, M. Oberthaler, and P. D. Drummond. Einstein-Podolsky-Rosen entanglement strategies in two-well Bose-Einstein condensates. *Phys. Rev. Lett.*, 106:120405, 2011.
- [97] Zhihao Lan and Carlos Lobo. Optical lattices with large scattering length: Using few-body physics to simulate an electron-phonon system. *Phys. Rev. A*, 90:033627, 2014.
- [98] G. J. Milburn, J. Corney, E. M. Wright, and D. F. Walls. Quantum dynamics of an atomic Bose-Einstein condensate in a double-well potential. *Phys. Rev. A*, 55:4318–4324, 1997.

- [99] B. R. Johnson. New numerical methods applied to solving the one-dimensional eigenvalue problem. *J. Chem. Phys.*, 67:4086, 1977.
- [100] Daniel Adam Steck. Rubidium 87 D line data. <http://steck.us/alkalidata/>, 2015.
- [101] R. J. Cook, D. G. Shankland, and A. L. Wells. Quantum theory of particle motion in a rapidly oscillating field. *Phys. Rev. A*, 31:564, 1985.
- [102] A. Härter, A. Krüchow, A. Brunner, and J. Hecker Denschlag. Minimization of ion micromotion using ultracold atomic probes. *Applied Physics Letters*, 102(22):221115, 2013.
- [103] Will Gunton, Mariusz Semczuk, and Kirk W. Madison. Realization of BEC-BCS-crossover physics in a compact oven-loaded magneto-optic-trap apparatus. *Phys. Rev. A*, 88:023624, 2013.
- [104] Henning A. Füst. *PhD thesis (in preparation)*. PhD thesis, University of Amsterdam, 2018.
- [105] Herman Feshbach. Unified theory of nuclear reactions. *Rev. Mod. Phys.*, 36:1076–1078, 1964.
- [106] Daniel Rotter. Photoionisation von Kalzium. Diploma thesis, University Innsbruck, 2003.
- [107] Ulrich Georg Poschinger. *Quantum optics experiments in a microstructured ion trap*. PhD thesis, University Mainz, 2010.
- [108] C. Pozrikidis. *A practical guide to boundary element methods with the software library BEMLIB*. CRC Press, 2002.
- [109] W. W. Macalpine and R. O. Schildknecht. Coaxial resonators with helical inner conductor. *Proceedings of the IRE*, 47(12):2099–2105, 1959.
- [110] J. D. Sivers, L. R. Simkins, S. Weidt, and W. K. Hensinger. On the application of radio frequency voltages to ion traps via helical resonators. *Applied Physics B*, 107(4):921–934, 2012.
- [111] Friedhelm Serwane. The setup of a magneto optical trap for the preparation of a mesoscopic degenerate Fermi gas. Diploma thesis, University Heidelberg, 2007.

- [112] Philipp Simon. Apparatus for the preparation of ultracold Fermi gases. Diploma thesis, University Heidelberg, 2010.
- [113] Gerhard Zürn. Realization of an optical microtrap for a highly degenerate Fermi gas. Diploma thesis, University Heidelberg, 2007.
- [114] M. Bartenstein, A. Altmeyer, S. Riedl, R. Geursen, S. Jochim, C. Chin, J. Hecker Denschlag, R. Grimm, A. Simoni, E. Tiesinga, C. J. Williams, and P. S. Julienne. Precise determination of  ${}^6\text{Li}$  cold collision parameters by radio-frequency spectroscopy on weakly bound molecules. *Phys. Rev. Lett.*, 94:103201, 2005.
- [115] Andre Wenz. *From Few to Many: Ultracold Atoms in Reduced Dimensions*. PhD thesis, University Heidelberg, 2013.
- [116] M. Johanning, A. Braun, D. Eiteneuer, C. Paape, C. Balzer, W. Neuhauser, and C. Wunderlich. Resonance-enhanced isotope-selective photoionization of Yb I for ion trap loading. *Applied Physics B*, 103(2):327–338, 2011.
- [117] Y. Takasu, K. Komori, K. Honda, M. Kumakura, T. Yabuzaki, and Y. Takahashi. Photoassociation spectroscopy of laser-cooled ytterbium atoms. *Phys. Rev. Lett.*, 93:123202, 2004.
- [118] Norman Vincenz Ewald. Quest for an ultracold hybrid atom-ion experiment. Master’s thesis, University Mainz, 2015.
- [119] Kilian Singer, Selim Jochim, Marcel Mudrich, Allard Mosk, and Matthias Weidemüller. Low-cost mechanical shutter for light beams. *Review of Scientific Instruments*, 73(12):4402–4404, 2002.
- [120] E. H. Pinnington, G. Rieger, and J. A. Kernahan. Beam-laser measurements of the lifetimes of the  $6p$  levels in Yb II. *Phys. Rev. A*, 56:2421–2423, 1997.
- [121] R. W. P. Drever, J. L. Hall, F. V. Kowalski, J. Hough, G. M. Ford, A. J. Munley, and H. Ward. Laser phase and frequency stabilization using an optical resonator. *Applied Physics B*, 31(2):97–105, 1983.
- [122] Michael Eric Gehm. *Preparation of an optically-trapped degenerate Fermi gas of  ${}^6\text{Li}$ : Finding the route to degeneracy*. PhD thesis, Duke University, 2003.

- [123] Arthur L. Schawlow. Spectroscopy in a new light. *Rev. Mod. Phys.*, 54:697–707, 1982.
- [124] Dipankar Das, Sachin Barthwal, Ayan Banerjee, and Vasant Natarajan. Absolute frequency measurements in Yb with 0.08 ppb uncertainty: Isotope shifts and hyperfine structure in the 399 nm  $^1S_0 \rightarrow ^1P_1$  line. *Phys. Rev. A*, 72:032506, 2005.
- [125] D. F. V. James. Quantum dynamics of cold trapped ions with application to quantum computation. *Appl. Phys. B*, 66:181, 1998.
- [126] J. H. Wesenberg, R. J. Epstein, D. Leibfried, R. B. Blakestad, J. Britton, J. P. Home, W. M. Itano, J. D. Jost, E. Knill, C. Langer, R. Ozeri, S. Seidelin, and D. J. Wineland. Fluorescence during Doppler cooling of a single trapped atom. *Phys. Rev. A*, 76:053416, 2007.
- [127] P. Taylor, M. Roberts, S. V. Gateva-Kostova, R. B. M. Clarke, G. P. Barwood, W. R. C. Rowley, and P. Gill. Investigation of the  $^2S_{1/2} - ^2D_{5/2}$  clock transition in a single ytterbium ion. *Phys. Rev. A*, 56:2699–2704, 1997.
- [128] S. Olmschenk, K. C. Younge, D. L. Moehring, D. N. Matsukevich, P. Maunz, and C. Monroe. Manipulation and detection of a trapped Yb<sup>+</sup> hyperfine qubit. *Phys. Rev. A*, 76:052314, 2007.
- [129] R. Islam, C. Senko, W. C. Campbell, S. Korenblit, J. Smith, A. Lee, E. E. Edwards, C.-C. J. Wang, J. K. Freericks, and C. Monroe. Emergence and frustration of magnetism with variable-range interactions in a quantum simulator. *Science*, 340(6132):583–587, 2013.
- [130] R. Blatt, H. Schnatz, and G. Werth. Ultrahigh-resolution microwave spectroscopy on trapped  $^{171}\text{Yb}^+$  ions. *Phys. Rev. Lett.*, 48:1601, 1982.
- [131] R. Blatt, H. Schnatz, and G. Werth. Precise determination of the  $^{171}\text{Yb}^+$  ground state hyperfine separation. *Zeitschrift für Physik A Atoms and Nuclei*, 312(3):143–147, 1983.
- [132] P. T. H. Fisk, M. J. Sellars, M. A. Lawn, and C. Coles. Accurate measurement of the 12.6 GHz clock transition in trapped  $^{171}\text{Yb}^+$  ions. *IEEE Trans. Ultrason. Ferroelectr. Freq. Control*, 44:344, 1997.
- [133] Mark Fox. Quantum optics. An introduction. In *Oxford Master Series in Physics*. 2006.

- [134] Norman F. Ramsey. A molecular beam resonance method with separated oscillating fields. *Phys. Rev.*, 78:695–699, 1950.
- [135] F. Mintert and C. Wunderlich. Ion-trap quantum logic using long-wavelength radiation. *Phys. Rev. Lett.*, 87(25):257904, 2001.
- [136] C. Ospelkaus, U. Warring, Y. Colombe, K. R. Brown, J. M. Amini, D. Leibfried, and D. J. Wineland. Microwave quantum logic gates for trapped ions. *Nature*, 476:181, 2011.
- [137] T. Ruster, C. T. Schmiegelow, H. Kaufmann, C. Warschburger, F. Schmidt-Kaler, and U. G. Poschinger. A long-lived Zeeman trapped-ion qubit. *Applied Physics B*, 122(10):254, 2016.
- [138] W. Nagourney, J. Sandberg, and H. Dehmelt. Shelved optical electron amplifier: Observation of quantum jumps. *Phys. Rev. Lett.*, 56(26):2797–2799, 1986.
- [139] T. B. Ottenstein, T. Lompe, M. Kohnen, A. N. Wenz, and S. Jochim. Collisional stability of a three-component degenerate Fermi gas. *Phys. Rev. Lett.*, 101:203202, 2008.
- [140] Mathias Neidig. A realization of a two-dimensional fermi gas in a standing wave trap. Master’s thesis, University Heidelberg, 2013.
- [141] E. L. Raab, M. Prentiss, Alex Cable, Steven Chu, and D. E. Pritchard. Trapping of neutral sodium atoms with radiation pressure. *Phys. Rev. Lett.*, 59:2631–2634, 1987.
- [142] J. Reichel, W. Hänsel, and T. W. Hänsch. Atomic micromanipulation with magnetic surface traps. *Phys. Rev. Lett.*, 83:3398–3401, 1999.
- [143] M. Weidemüller, T. Esslinger, M. A. Ol’shanii, A. Hemmerich, and T. W. Hänsch. A novel scheme for efficient cooling below the photon recoil limit. *Europhysics Letters*, 27(2):109, 1994.
- [144] D. Boiron, C. Triché, D. R. Meacher, P. Verkerk, and G. Grynberg. Three-dimensional cooling of cesium atoms in four-beam gray optical molasses. *Phys. Rev. A*, 52:R3425–R3428, 1995.
- [145] J. Joger, H. FÜRST, N. V. Ewald, T. Feldker, M. Tomza, and R. Gerritsma. Observation of collisions between cold Li atoms and Yb<sup>+</sup> ions. *Phys. Rev. A*, 96:030703, 2017.

- [146] Humberto da Silva Jr, Maurice Raoult, Mireille Aymar, and Olivier Dulieu. Formation of molecular ions by radiative association of cold trapped atoms and ions. *New J. Phys.*, 17:045015, 2015.
- [147] Christoph Zipkes, Stefan Palzer, Lothar Ratschbacher, Carlo Sias, and Michael Köhl. Cold heteronuclear atom-ion collisions. *Phys. Rev. Lett.*, 105:133201, 2010.
- [148] NIST Atomic Spectra Database <http://physics.nist.gov/PhysRefData/ASD>, 2017.
- [149] Timur V. Tscherbul, Paul Brumer, and Alexei A. Buchachenko. Spin-orbit interactions and quantum spin dynamics in cold ion-atom collisions. *Phys. Rev. Lett.*, 117:143201, 2016.
- [150] Elvira R. Sayfutyarova, Alexei A. Buchachenko, Svetlana A. Yakovleva, and Andrey K. Belyaev. Charge transfer in cold  $\text{Yb}^+ + \text{Rb}$  collisions. *Phys. Rev. A*, 87:052717, 2013.
- [151] Henning FÜRST, Thomas Feldker, Norman V. Ewald, Jannis Joger, Michal Tomza, Tomza, and Rene Gerritsma. Dynamics of a single ion spin impurity in a spin-polarized atomic bath. *arXiv:1712.07873*, 2017.
- [152] C. Monroe, D. M. Meekhof, B. E. King, S. R. Jefferts, W. M. Itano, D. J. Wineland, and P. L. Gould. Resolved-sideband Raman cooling of a bound atom to the 3D zero-point energy. *Phys. Rev. Lett.*, 75(22):4011–4014, 1995.
- [153] Ch. Schneider, M. Enderlein, T. Huber, and T. Schaetz. Optical trapping of an ion. *Nature Photonics*, 4, 2010.
- [154] Alexander Lambrecht, Julian Schmidt, Pascal Weckesser, Markus Debatin, Leon Karpa, and Tobias Schaetz. Long lifetimes and effective isolation of ions in optical and electrostatic traps. *Nature Photonics*, 11, 2017.
- [155] Tobias Schaetz. Trapping ions and atoms optically. *Journal of Physics B: Atomic, Molecular and Optical Physics*, 50(10):102001, 2017.
- [156] Julian Schmidt, Alexander Lambrecht, Pascal Weckesser, Markus Debatin, Leon Karpa, and Tobias Schaetz. Optical trapping of ion coulomb crystals. *Phys. Rev. X*, 8:021028, 2018.

- [157] J. Deiglmayr, A. Göritz, T. Best, M. Weidemüller, and R. Wester. Reactive collisions of trapped anions with ultracold atoms. *Phys. Rev. A*, 86:043438, 2012.
- [158] T. Secker, N. V. Ewald, J. Joger, H. Fürst, T. Feldker, and R. Gerritsma. Trapped ions in Rydberg-dressed atomic gases. *Phys. Rev. Lett.*, 118:263201, 2017.
- [159] Norman V. Ewald. *PhD thesis (in preparation)*. PhD thesis, University of Amsterdam, 2019.
- [160] N. Yu and L. Maleki. Lifetime measurements of the  $4f^{14}5d$  metastable states in single ytterbium ions. *Phys. Rev. A*, 61:022507, 2000.
- [161] M. Schacht, J. R. Danielson, S. Rahaman, J. R. Torgerson, J. Zhang, and M. M. Schauer.  $^{171}\text{Yb}^+ \ ^5\text{D}_{3/2}$  hyperfine state detection and  $F=2$  lifetime. *Journal of Physics B: Atomic, Molecular and Optical Physics*, 48(6):065003, 2015.
- [162] R. W. Berends, E. H. Pinnington, B. Guo, and Q. Ji. Beam-laser lifetime measurements for four resonance levels of Yb II. *J. Phys. B: At. Mol. Opt. Phys.*, 26:L70–L704, 1993.
- [163] M. Roberts, P. Taylor, G. P. Barwood, P. Gill, H. A. Klein, and W. R. C. Rowley. Observation of an electric octupole transition in a single ion. *Phys. Rev. Lett.*, 78:1876–1879, 1997.
- [164] T. Feldker, H. Fürst, N. V. Ewald, J. Joger, and R. Gerritsma. Spectroscopy of the  $^2\text{S}_{1/2} \rightarrow ^2\text{P}_{3/2}$  transition in Yb II: Isotope shifts, hyperfine splitting, and branching ratios. *Phys. Rev. A*, 97:032511, 2018.
- [165] Steven Matthew Olmschenk. *Quantum teleportation between distant matter qubits*. PhD thesis, University of Michigan, 2009.